In-Medium Modification of Pion-Pairs on Deuterium

von

Stefan Lugert

aus

Butzbach - Ebersgöns

Dem
Fachbereich Mathematik und Informatik, Physik, Geographie
Justus-Liebig-Universität Gießen
zur Erlangung des akademischen Grades

Dr. rer. nat.

vorgelegte Dissertation

Vorsitzender:	Prof. Dr. Volker Metag
Berichter:	PD Dr. Stefan Leupold
	Prof. Dr. Jürgen Kiefer
Tag der mündlichen Prüfung:	23. November 2007

Gießen, den 18. Oktober 2007

Der Spaß fängt erst dann an, wenn man die Regeln kennt. Im Universum aber sind wir momentan noch dabei, die Spielanleitung zu lesen. (Richard P. Feynman)

gedruckt von *stafadruck GmbH*, 35625 Hüttenberg

Zusammenfassung

In dieser Arbeit wird die quasifreie Photoproduktion von Pionenpaaren an gebundenen Nukleonen entsprechend der Reaktionsgleichung

$$\gamma + A \longrightarrow \pi\pi(A-1) + N$$

für flüssiges Deuterium analysiert. Diese Messungen ermöglichen eine vom Isospin abhängige Bestimmung der massendifferentiellen und totalen Wirkungsquerschnitte am Deuteron.
In vorausgegangenen Experimenten der CHAOS- und Crystal Ball Kollaboration wurde bereits die pioneninduzierte Produktion von Pionenpaaren gemessen. Die Verteilung der invarianten Massen zeigte für das isoskalare $\pi\pi$ Mesonensystem mit größer werdender Ordnungszahl eine Verschiebung der Intensität zur Schwelle hin. Im Einklang mit theoretischen Rechnungen kann dieser Effekt als Indiz für die teilweise Wiederherstellung der Chiralen Symmetrie gedeutet werden.
Da Pionen stark wechselwirkende Teilchen sind, die mit großer Wahrscheinlichkeit an der Oberfläche der Targetkerne absorbiert werden, untersuchen diese Experimente lediglich die Oberfläche und somit kleine effektive Dichten. Photonen hingegen könnnen im gesamten Kern Reaktionen induzieren und somit auch große effektive Dichten sondieren. Ein Vorreiterexperiment mit einem Photonenstrahl wurde durch die TAPS Kollaboration im Jahre 1999 am Mainzer Beschleuniger MAMI-B durchgeführt. Die dortigen Messungen ergaben für den isoskalaren $\pi^0\pi^0$ Kanal mit größer werdender Ordnungszahl auch eine Verschiebung der Intensität zur Schwelle hin. Im $\pi^{\pm}\pi^0$ Kanal konnte dieser Effekt nicht beobachtet werden, dies diente als Referenz. Die Beobachtungen bestätigten die Ergebnisse der vorausgegangenen Experimente, da Endzustandswechselwirkungen der Pionen die beiden Isospin-Kanäle in erster Näherung ähnlich beeinflussen. Aufgrund der unzureichenden statistischen Signifikanz der Daten war die Aussagekraft des Experiments jedoch limitiert.

Das Experiment, welches in dieser Arbeit beschrieben wird, erzielte eine wesentlich bessere Statistik, die eine Überprüfung der alten Daten erlaubt. Um näherungsweise den kompletten Raumwinkel von 4π zur Teilchenidentifikation abzudecken wurde in diesem Experiment der TAPS Detektor als Vorwärtswand in Verbindung mit dem Crystal Ball Detektor an MAMI verwendet. Der Experimentaufbau startete Ende 2003. Die neue Ausleseelektronik für die BaF_2 Detektoren kam hier zum ersten Mal zum Einsatz. Zwischen Juni 2004 und April 2005 wurden Messungen an unterschiedlichen Targets vorgenommen, unter anderem auch die lD_2 Daten, welche in dieser Arbeit anaysiert wurden.
Die von Ralf Gregor vorgenommene Analyse der neuen Daten bestätigt die zuvor gemessenen und veröffentlichten Daten. Die Verschiebung der invarianten $\pi^0\pi^0$ Massen zur Schwelle hin ist jedoch weniger stark ausgeprägt als in den publizierten Daten beschrieben. Neben der Analyse der Festkörpertargets (C, Ca und Pb), die von Ralf Gregor durchgeführt wurde, ist die Analyse von Deuterium aus den folgenden beiden Gründen ein entscheidender Beitrag, um die ablaufenden Prozesse zu verstehen. Zum Einen kann

man die Festkörpertargets und Wasserstoff mit dem leichtesten Kern, dessen Nukleonen Fermi-Bewegung aufweisen und der zugleich das geringste Kernvolumen hat, dem Deuterium vergleichen. Weiterhinn gibt es derzeit keine massendifferentiellen Wirkungsquerschnitte für die beschriebenen Kanäle am Deuterium. Durch die Analyse der Deuterium-Daten und Subtraktion der publizierten Wasserstoff-Daten kann der massendifferentielle Wirkungsquerschnitt am Neutron bestimmt werden. Eine grundlegende Frage der Theorie ist, ob die Wirkungsquerschnitte am Neutron und am Proton identisch sind, bzw. in wieweit sie im relevanten Energiebereich voneinander abweichen.
Um die Wirkungsquerschnitte quantitativ zu bestimmen benötigt man die Effizienz des Detektorsystems. Um diese zu berechnen, entwickelte ich die MonteCarlo Simulation für den verwendeten Detektoraufbau unter Verwendung einer auf GEANT basierenden Vorlage des Crystal Ball Simulationscodes.
Derzeit können die BUU-Transportrechnungen die Unterschiede in den beiden Isospin Kanälen für die Festkörpertargets nicht richtig wiedergeben. Dies könnte auf Unsicherheiten in den Produktionsquerschnitten am Neutron zurückgeführt werden. Eine endgültige Aussage, ob die Effekte alleine durch Endzustandswechselwirkungen oder durch teilweise Wiederherstellung der chiralen Symmetrie erklärt werden kann, kann aus diesem Grunde noch nicht getroffen werden. Durch die Bestimmung der Wirkungsquerschnitte am Neutron und Implementation der Erkenntnisse in den BUU Code können die Rechnungen wiederholt und dann mit den publizierten Daten verglichen werden.
Im Vergleich zum Proton zeigt der differentielle Wirkungsquerschnitt am Neutron eine relative Verschiebung der Intensität zur Schwelle der $\pi\pi$-Massen. Mit dem hier gegebenen Wirkungsquerschnitt kann die Theorie nun ihre Modelle bezüglich der Anregungsfunktion am Neutron anpassen.
Von Dezember 2002 bis Oktober 2003 entwickelte ich die SlowControl für die neue TAPS Elektronik, basierend auf einer 6U-VME Ausleseplatine (CAEN-V874 Motherboard). Die Elektronik wurde auf die speziellen Belange der BaF_2 Szintillatoren zugeschnitten und kam in dieser Crystal Ball/TAPS@MAMI Strahlzeit erstmalig zum Einsatz.
Zwischen November und Dezember 2003 baute ich mit Ralf Gregor ein Test-Experiment mit 19 BaF_2 Kristallen am Institut für Kernphysik in Mainz auf.

Im Januar 2004 begannen wir mit der Errichtung des kompletten TAPS-Detektorsystems als Vorwärtswand. Diese Vorwärtswand bestand aus 510 BaF_2 Kristallen unter Verwendung der neuen Elektronik und 510 Plastikszintillatoren, die vor den einzelnen Kristallen als Detektor für geladene Teilchen (Charged Particle Veto, CPV) angebracht wurden. In Kombination mit dem Crystal Ball, der Photonenmarkierungsanlage (Glasgow-Mainz-Tagger), zwei Drahtkammern (Multi Wire Proportional Chamber, MWPC) und einem Teilchenidentifikationsdetektor (Particle Identification Detector, PID) wurde ein gemeinsames Auslesesystem errichtet.

Abstract

In this thesis the quasifree photoproduction of pion pairs on bound nucleons

$$\gamma + A \longrightarrow \pi\pi(A-1) + N$$

is analyzed for liquid Deuterium. These measurements allow an isospin dependent determination of the mass differential and total cross section of pion pairs on Deuterium.
In former experiments pion induced production of pion pairs was measured by the CHAOS- and Crystal Ball collaborations. The invariant mass distributions showed a shift in strength towards the threshold region with increasing atomic number of the targets in case of the isoscalar $\pi\pi$ meson system. According to theoretical predictions this effect could be interpreted as a positive signature of a partial restoration of chiral symmetry.
As pions are strongly interacting particles, which get absorbed in the surface region of the nucleus, these measurement only probed small effective densities. In contrast, photons can penetrate the whole nucleus resulting in a higher effective nuclear density. A pioneering experiment with a photon beam was performed by the TAPS collaboration at the accelerator facility MAMI-B in Mainz in 1999. This measurement observed an invariant mass shift of the isoscalar $\pi^0\pi^0$ channel with increasing atomic number as well. In the $\pi^{\pm}\pi^0$ channel this effect was not observed which served as a cross check. This observation confirmed the former experiments, since final state interactions of the pions would affect in first order both isospin channels in a similar way. Due to the poor statistics, the significance of the data was however limited.

The experiment described in this work reached a much higher statistical significance, allowing a review of the old data. In this experiment, the TAPS detector was used as a forward wall in combination with the Crystal Ball detector to achieve almost the complete 4π solid angle coverage for particle detection at the MAMI accelerator facility. The installation of the experimental setup started at the end of 2003. The new readout electronics for the BaF_2 crystals was used for the first time. Between June 2004 and April 2005 measurements on several targets were performed, including the lD_2 data which has been analyzed in this work.
The new data analysis, performed by Ralf Gregor, confirms the previously measured and published data. However, the shift of the invariant $\pi^0\pi^0$ mass to the threshold region is less pronounced compared to the published data. Beside the analysis of the solid targets (C, Ca and Pb), which was performed by Ralf Gregor, the analysis of the Deuterium data is an essential contribution to understanding the ongoing processes for two reasons. Firstly, there is the possibility to compare the solid targets and Hydrogen to the lightest nucleus having Fermi motion included but the lowest possible nuclear volume, the Deuterium. For the second reason, there are no data for the mass differential cross section on the neutron available for the mentioned channels. Analyzing the Deuterium data and subtracting the published proton data, the cross section on the neutron gets accessible. An essential question for the theory is, whether the cross section on neutron and proton are the same or how much they differ in the relevant energy regime.

To determine the absolute cross section, the efficiency of the detector system is required. To provide this efficiency, I also developed the MonteCarlo simulation using a skeleton of the Crystal Ball simulation code, based on the GEANT package.
Presently, BUU transport calculations can not describe the different behavior in the isospin channels for the solid targets, which may partly be due to uncertainties in the production cross section on the neutron. Therefore, a final interpretation of the observed mass shift - whether it can be described by final state interaction alone or by a partial restoration of chiral symmetry - can not be made as yet. With the cross section determination on the neutron, the BUU calculations can be refined and compared to the analyzed data again.
The cross section on the neutron shows a relative shift of strength towards lower $m_{\pi\pi}$ in comparison to the cross section on the proton. With the cross section on the neutron available, refined transport calculations should be performed.

From December 2002 till October 2003 I developed the slow control for the new TAPS electronics, which was based on a 6U-VME readout board (CAEN-V874 motherboard). The electronics was tailored to the specific needs of BaF_2-scintillators, and it was used the first time in the Crystal Ball/TAPS@MAMI beam period.
In November and December 2003, together with Ralf Gregor, we built a test setup with 19 BaF_2-crystals at the tagged photon facility of the Institut für Kernphysik in Mainz.
In January 2004 we began the installation of the full TAPS setup as a forward wall, consisting of 510 BaF_2-crystals using the new electronics and 510 individual plastic scintillators which served as a charged particle veto detector (CPV). In combination with the Crystal Ball, the Glasgow-Mainz-Tagger, two wire chambers (MWPC's) and a particle identification detector (PID), a common readout system was installed.

Contents

List of Tables

List of Figures

1. Motivation and theoretical background

In this work, the 2π interaction in the so called σ-channel (I=J=0) in the nuclear medium is investigated. This allows to experimentally study a possible effect of chiral symmetry restoration. Its signature would be identified in a stronger mass shift in the $I = 0$ $\pi\pi$ system compared to the $I \neq 0$ $\pi\pi$ system.

1.1. Introduction

"What is the world made of?" and *"What holds it together?"* have been interesting questions since the time of the ancient world. The Greek philosopher Demokrit postulated around 400 B.C. that all matter is composed of indivisible particles, the atoms. He also claimed that those atoms are so small that they have no internal structure, and were thus elementary particles. This theory was not accepted by the entire world. Other atom models, like the one invented by Aristoteles comprising the 4 elements - water, air, fire and earth - came up. In the 18th century, due to chemical experiments, one found that air consists of more than one "indivisible" particle. In the 19th century, Thompson found electrons in cathode-ray experiments and postulated an atomic model where the negative electrons are embedded in some positive material. At the beginning of the 20th century, Rutherford studied scattering experiments by shooting α-particles on some thin metal foils and with his results he invented a new atomic model. Based on those scattering experiments he postulated that atoms consist of a very small core with positive charge carrying the complete mass, surrounded by a large cloud of negative electrons. Bohr modified this model postulating discrete states for the electrons with electrons rotating around the nucleus without emitting radiation. Electrodynamics demands accelerated charged particles to emit radiation. The electrons would fly into the nucleus following some spiral. Consequently, the atom would have to collapse. The Bohr model was e.g. able to describe the Balmer series emitted by the hydrogen atom. Using quantum mechanics, physicist like Heisenberg, Born and Feynman developed Quantum Electro-Dynamics (QED), the relativistic quantum field theory. This theory was able to describe all interactions of charged particles. The outcome of this is an orbital model for the atom which was able to describe all atomic processes and chemical reactions.

In 1932 the neutron as second constituent of the nucleus (beside the proton) was found. In accelerator experiments, performed in the 1950's and 1960's, lots of new particles, called hadrons were found. Gell-Mann and Ne'eman developed a method to order this particle zoo by inventing a new type of sub-nuclear and elementary particle, the quarks. In this model, all of the baryons were supposed to be built from 3 quarks. Nowadays, the existence of 6 quark flavors is well established. This model also was able to predict charge and mass of new particles that had not yet been found. The great break-through of the model was the prediction of the Ω^- baryon, which was found some years later in an experiment.
The standard model of particles contains six quarks, six leptons, grouped into three fam-

generation	name	mass	charge	l_e	l_μ	l_τ
1	e^-	511 keV	-1	+1	0	0
	ν_e	< 2 eV	0	+1	0	0
2	μ^-	105.66 MeV	-1	0	+1	0
	ν_μ	< 0.2 eV	0	0	+1	0
3	τ	1784 MeV	-1	0	0	+1
	ν_τ	< 18.2 MeV	0	0	0	+1

Table 1: Lepton properties.
The data were taken from [PDG06].

generation	name	mass	charge	I_3	S	C	B	T
1	up (u)	$1.5 \ldots 3.0$ MeV	+2/3	+1/2	0	0	0	0
	down (d)	$3 \ldots 7$ MeV	-1/3	-1/2	0	0	0	0
2	charm (c)	$1150 \ldots 1350$ MeV	+2/3	0	0	+1	0	0
	strange (s)	$75 \ldots 170$ MeV	-1/3	0	-1	0	0	0
3	top (t)	≈ 17400 MeV	+2/3	0	0	0	0	+1
	bottom (b)	$4000 \ldots 4400$ MeV	-1/3	0	0	0	-1	0

Table 2: Quark properties.
The data were taken from [PDG06].

ilies, and the exchange bosons (as mediators of the forces), being responsible for the interaction of the elementary particles (figure 1). Not shown are the anti-particles with same mass but opposite charge. In addition, the quarks have color (red, blue, green) and the anti-quarks the corresponding anti-colors. Moreover the gluons, the mediators of the strong force carry a color/anti-color mixture. All together the standard model consists of the following 61 particles:

- $6 \cdot 3$ quarks and anti-quarks Σ=36
- 6 leptons and anti-leptons Σ=12
- 1 photon, the mediator of the electromagnetic interaction
- 8 gluons, mediators of the strong interaction
- 3 bosons (W^+, W^-, Z^0), mediators of the weak interaction
- 1 Higgs boson (not yet found)

The properties of the leptons are shown in table 1. Beside mass and charge, the lepton numbers for electrons (l_e), muons (l_μ) and taus (l_τ), that are conserved for any decay process, are shown. All antileptons have same numbers with opposite sign. In table 2, the quark properties are listed. In comparison to the leptons, the quantities like isospin (I_3), strangeness (S), charm- (C) bottom- (B) and top numbers (T) are only conserved for strong interactions. Also here the sign flips for anti quarks.

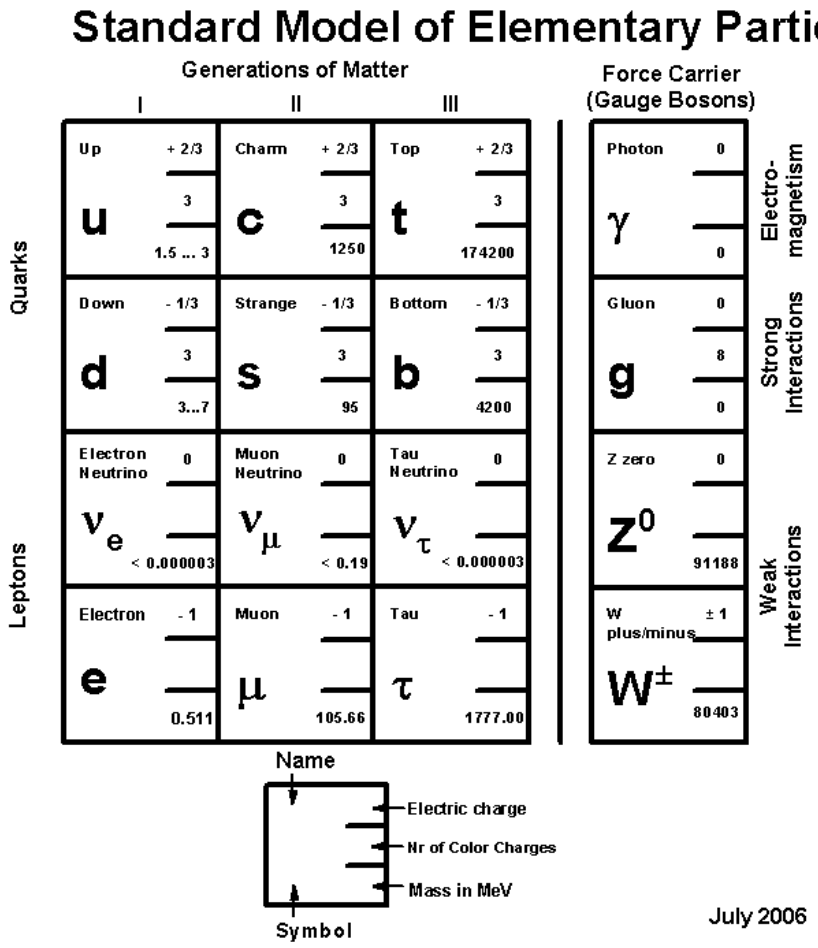

Figure 1: The standard model of elementary particles.
The data were taken from [PDG04], the layout from [Smc94].

However, there are still some open questions:

- At the moment, only the electromagnetic and the weak interactions can be described by a combined theory, leading to the electroweak force. Not implemented are the strong interaction and gravitation. Is there a theory, the so called "Grand Unified Theory", describing all known physics.

- If the center of mass energies are increased, will there be an observable inner structure of the quarks and leptons?

- The theory to describe all strong interactions among quarks and gluons is Quantum Chromo Dynamics (similar to Quantum Electro Dynamics). The QCD can not be solved quantitatively (for the low energy regime) because the mediator bosons, the gluons, carry strong charge themselves. The coupling constant α_s is not constant over whole momentum range. In the regime of low energy / low momentum transfer α_s is no longer small, so that the equations of QCD cannot be solved by perturbation

theory. Therefore lattice calculations must be developed.

- Not understood is the mechanism of generating hadron masses from the current quark masses. Why do the constituent quark masses differ so much from the current quark masses?
- Another question is, whether the Higgs boson really exists and if yes, how the current quark masses are generated?

For all these questions, new large experiments like LHC@CERN and FAIR@GSI are being designed and set up.[GSI][CERN]

All masses and widths of particles listed by the Particle Data Group (see [PDG04]) are particle masses in the vacuum. But what happens to the mass, when a particle is generated or decaying under extreme conditions? If there was an effect of temperature or density on the mass of hadrons, an effective mass should be determinable. This thesis will focus on the question whether masses of hadrons are static properties or whether they can change as a function of temperature or density.

1.2. Properties of Hadrons

Baryons are composed of three quarks in all color states (blue, red, green) resulting in a color neutral baryon. By combining quark/anti-quark pairs (blue/anti-blue, red/anti-red, green/anti-green), also color neutral particles, the mesons, are generated.

1.2.1. Mesons

Mesons consist of a bound quark/anti-quark ($\overline{q}q$) pair. Mesonic states with the lowest masses (e.g. the pions), do not have an orbital angular momentum ($L = 0$). Because of this the total angular momentum for this mesons is equal to the total spin of the quarks $\overrightarrow{J} = \overrightarrow{L} + \overrightarrow{S}$. As quarks and anti-quarks are fermions, they carry the spin $S = \frac{1}{2}$, so they can be arranged to mesons with parallel ($\uparrow\uparrow$) or anti parallel ($\downarrow\uparrow$) spins. Mesons have a parity of $P = (-1)^{L+1}$ (which is for this case $P = -1$). As a result of this, it is possible to distinguish pseudo scalar mesons ($J^P = 0^-$) from vector mesons ($J^P = 1^-$). In case of the u and d quark, the current masses are almost the same and small compared to hadronic scales, allowing one to describe these quarks as two different states of the same particle. The symmetry group is called SU(2) flavor symmetry. Due to the fact that the mass difference of the quarks in comparison to the masses of the hadrons is almost negligible, the SU(2) flavor symmetry is almost conserved. The formalism to distinguish u from d quarks in the SU(2) group is called Isospin. Here the u and d quark form the Isospin doublet ($I = \frac{1}{2}$) with the states $I_3(u) = +\frac{1}{2}$ and $I_3(d) = -\frac{1}{2}$. Adding the s quark, the SU(3) flavor symmetry takes over. Another quantum number, the strangeness is introduced. Strangeness is an additive quantum number, where the s quark has $S = -1$

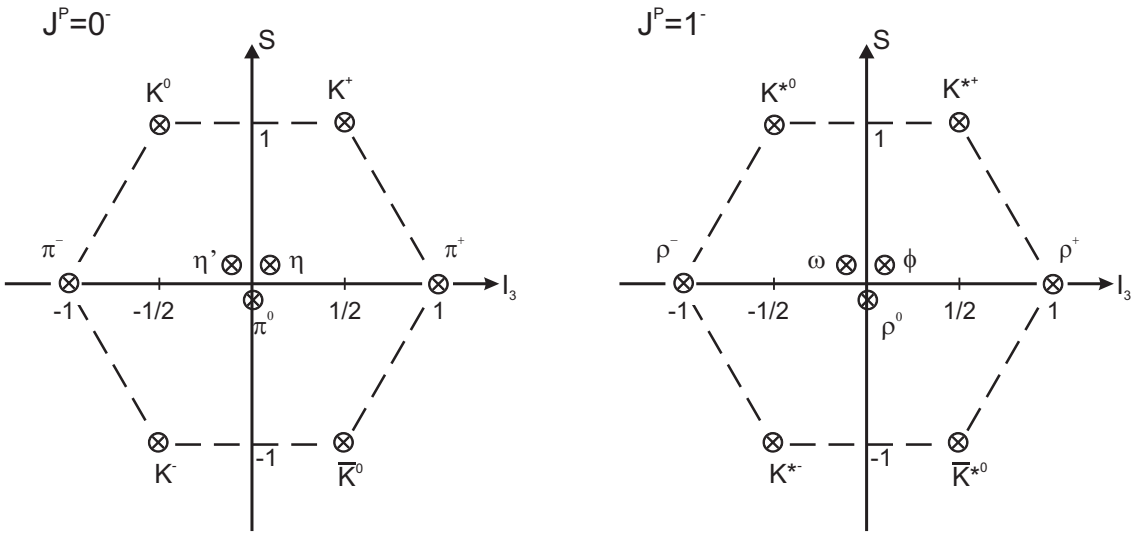

Figure 2: Nonets of pseudoscalar (left) and vector mesons (right).

and the $\overline{s}$ quark has $S = +1$. Combining now the 3 quarks (u, d, s), 9 combinations with $J = 0$, the pseudoscalar mesons and 9 combinations with J=1, the vector mesons are possible. Derived from group theoretical aspects (which will not be described further in this work), the 9 combinations can be separated into an octet and a singlet. In figure 2 the SU(3) group is shown for the pseudoscalar and the vector mesons according to their Isospin (I_3) and strangeness S. Quarks combined to mesons with angular orbital momentum L > 0 are able to create states with positive parity. Mesons corresponding to the pseudo scalar mesons ($J^P = 0^-$) with positive parity are the scalar mesons with $J^P = 0^+$; and for the vector mesons ($J^P = 1^-$), the corresponding states are called axial vector mesons ($J^P = 1^+$).

1.2.2. Baryons

Like the mesons, the baryons can be ordered according to their quark content. Since the baryons are fermions, they have to be built from 3 quarks. Taking only the 3 light quarks into account, 27 different qqq combinations can be built. Derived from group theory, two octet with mixed symmetry, an antisymmetric singlet and a symmetric decuplet describe the $3^3 = 27$ combinations completely($10 \otimes 8 \otimes 8 \otimes 1$). The total spin of the baryons can have the value $S = \frac{3}{2}$ for all spins having the same orientation ($\uparrow\uparrow\uparrow$) or $S = \frac{1}{2}$ ($\uparrow\downarrow\uparrow$). For baryons without orbital angular momentum ($L = 0$), the total angular momentum is identical to the total spin. Taking into account the possible spin orientations and the condition to have an anti symmetric wave function of the particles, one octet and the singlet have to disappear so that the multiplets shown in figure 3 remain: The protons, as lightest

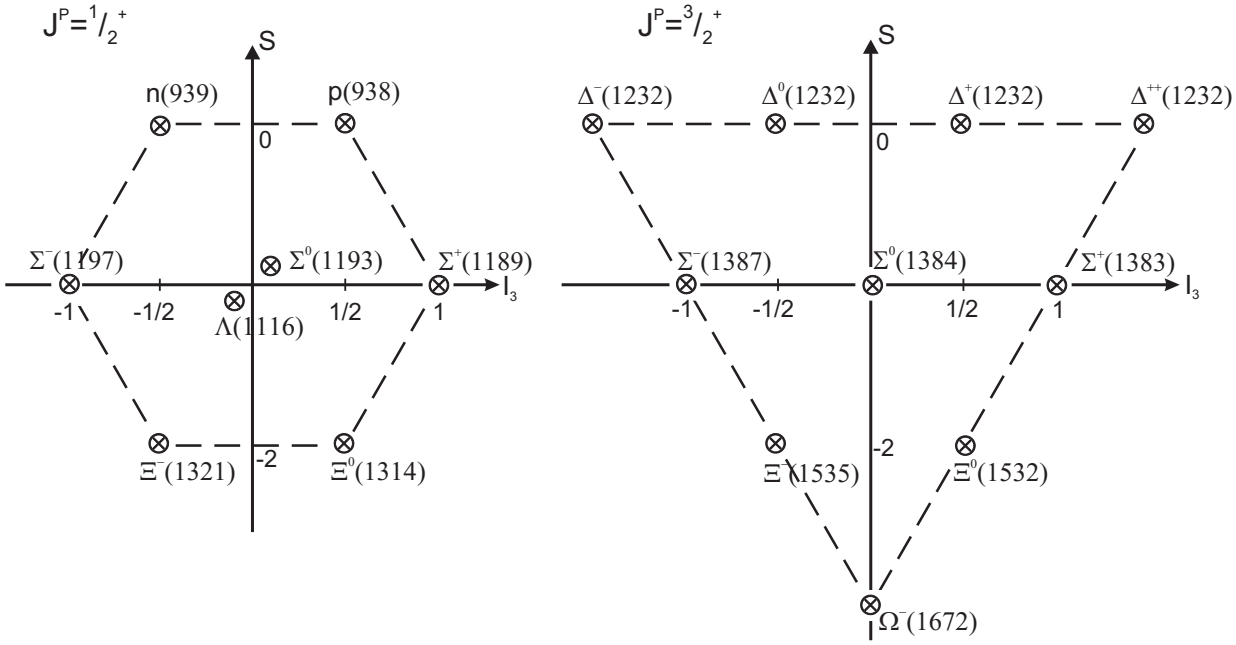

Figure 3: The lightest baryon octet and anti-decuplet.

baryons, must be stable (otherwise the whole universe, the way we know it, would not exist). Applying the isospin formalism to the proton and neutron, they can be described as two states of the nucleon. This is very useful since they should interact the same way with the strong force and have the same excitation mechanism. In light of this, protons and neutrons will simply be referred to as nucleons for the following discussion.
Nucleons can be excited into higher energy states by deposition of energy e.g. by shooting real photons (photoproduction) or virtual photons, having their origin in electron scattering (electroproduction) into the nucleon. Those meta stable states are called resonances. The most famous resonance is the $\Delta(1232)$ resonance. The Δ can be populated by bringing enough energy into a nucleon to achieve a spin flip reaction $N(\uparrow\downarrow\uparrow)+\Delta E \longrightarrow \Delta(\uparrow\uparrow\uparrow$). In addition, several hundred resonances are known. In figure 4 the excitation spectrum of the nucleon with respect to the available photon energy provided by the MAMI-B accelerator ($E_\gamma \leq 885$ MeV) is shown.

Looking into the total photoabsorption cross section off the proton, one can see two peaks (see figure 5). The Δ resonance is located in the first resonance region with energies smaller 0.5 GeV. The other peakthat is situated at higher peak energies, called the "second resonance region", is a superposition of several resonances (accessible with MAMI-B energies). The largest contribution to the cross section originates from the $P_{11}(1440)$, $D_{13}(1520)$ and $S_{11}(1535)$, see section 1.6.

The baryons, having positive parity $L = 0$, also have chiral partners with an angular orbital momentum $L \neq 0$ and negative parity.

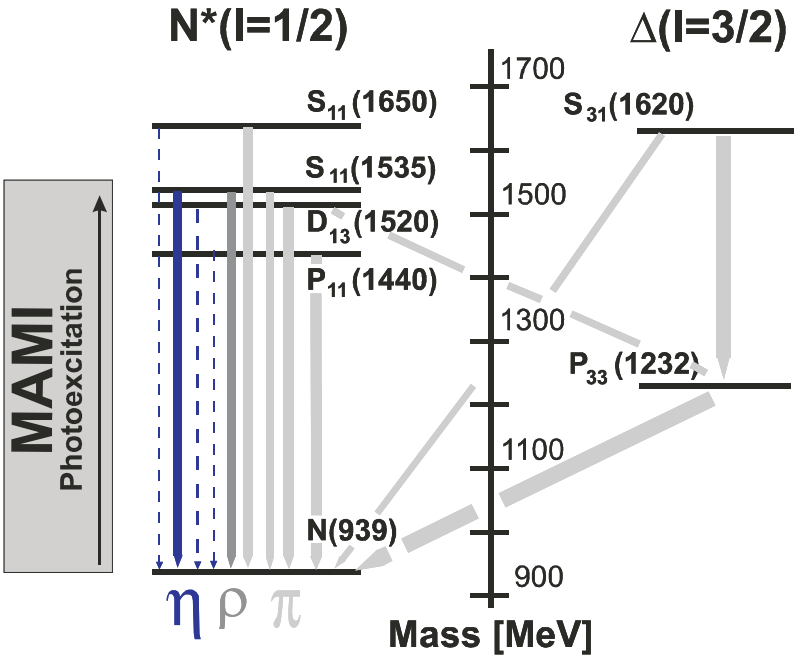

Figure 4: Resonance decay scheme accessible with MAMI-B energies.

1.3. Basics on Chiral Symmetry

Chiral symmetry is a fundamental symmetry on the quark-level and a basic feature of the strong interaction. Since this symmetry is limited to massless quarks, they would travel at the speed of light. Massless fermions can be either right or left handed. These two types of fermions cannot transform into each other. Gluons do not distinguish between left- and right-handed and they do not change helicity. As a result of this, the handedness or helicity of massless particles is conserved and can be calculated as shown in equation 1,

$$h = \frac{\overrightarrow{s} \cdot \overrightarrow{p}}{|\overrightarrow{s}| \cdot |\overrightarrow{p}|} \tag{1}$$

where $\overrightarrow{s}$ is the spin, $\overrightarrow{p}$ the momentum and h the helicity of the considered particle.
As soon as the quark has a mass, it can no longer travel at the speed of light. One can therefore find an inertial reference frame that is moving faster than this particle. As the momentum vector changes, right handed particles can become left handed (and vice-versa). One can observe a mixing of the left and right handed worlds. Evidently, chiral symmetry exists in the chiral limit. However, because of the small masses of the current quarks ($m_u \approx 1.5 \ldots 3.0$ MeV; $m_d \approx 3 \ldots 7$ MeV) compared to the baryon masses ($m_N \approx 939$ MeV), chiral symmetry should be conserved approximately. If chiral symmetry was naively realized, the chiral partners would have the same mass. In addition to the small explicit breaking, the chiral symmetry is broken spontaneously. The vacuum of the QCD ground state does not have this symmetry. The vacuum is not actually empty but is filled up with the chiral condensate ($\langle 0 \mid \bar{q}q \mid 0 \rangle \neq 0$ or shorter $\bar{q}q$ pairs). To check

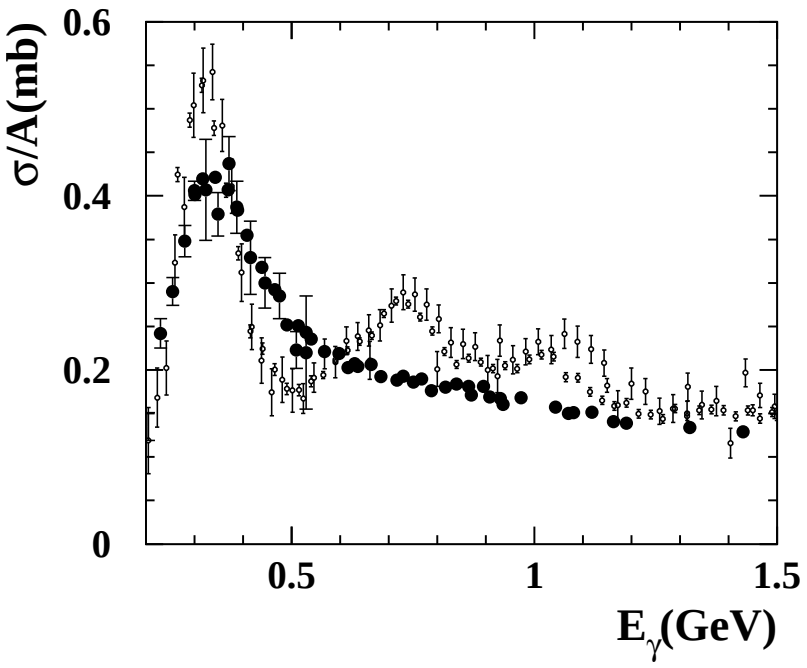

Figure 5: Total photo absorption cross section.
The black circles represent the measured cross section on the proton, the black dots an average over several nuclear targets. The figure was taken from [Trn06].

whether the chiral symmetry is broken on the hadron level, one can have a look at the chiral partners like the ρ-meson (1^-) and the a_1-meson (1^+) where $m_\rho = 770$ MeV and $m_{a_1} = 1260$ MeV. Here the mass split is comparable to the mass of hadrons.

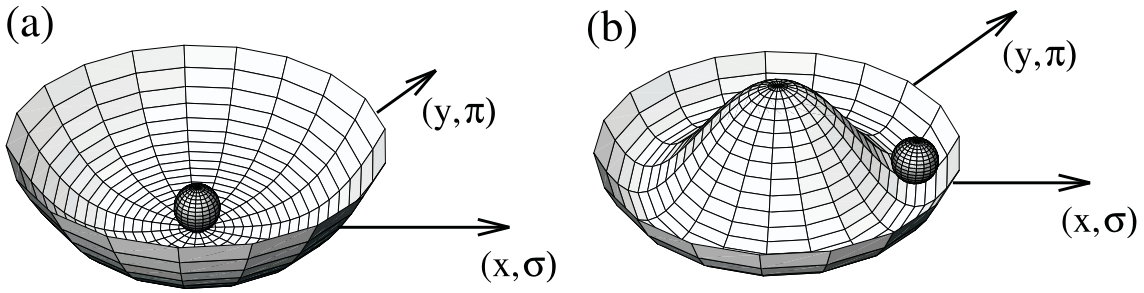

Figure 6: Potential illustrating the breaking of chiral symmetry.
The plot was taken from [Koc02].

To describe this effect, figure 6 shows two symmetric potentials. In the left picture, the ground state is in the center of the potential. In the right plot, the ground state is no longer in the middle. The QCD Lagrangian is depending on two fields, one for massless (called π) and another for massive states (σ). If both fields were zero at the ground state, one would expect a potential like it is shown in figure 6 a. In picture b), the ground state is not

in the middle of the potential, which means that one of the fields has to have a non-zero expectation value. As a consequence of that non-zero chiral condensate ($\langle \overline{q}q \rangle \propto \langle \sigma \rangle \neq 0$),

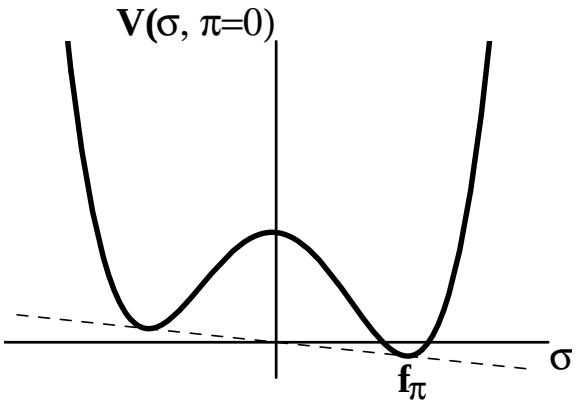

Figure 7: Spontaneous and explicit symmetry breaking.
The plot was taken from [Koc02].

$\left(N_{flavor}^2 - 1\right)$ massless Goldstone-bosons are predicted. Due to the fact that chiral symmetry is broken explicitly, one expects a small mass for those Goldstone-bosons. Figure 7 shows a projection of figure 6 b for $\pi = 0$. Due to the explicit symmetry breaking caused by the small mass differences of the quarks, the QCD lagrangian loses rotational invariance in this intrinsic $\sigma - \pi$ space.
In SU(2) flavor symmetry, where only the two lightest quarks are considered, 3 light mesons are expected. In nature one can find 3 pions ($\pi^{\pm}, \pi^0$) with a very small mass compared to the baryon mass ($m_{(\pi^{\pm})} \approx 139$ MeV, $m_{(\pi^0)} \approx 135$ MeV). Taking also into account the s-quark, the symmetry group changes to SU(3) and 5 more Goldstone-bosons (with higher mass than the pions, the etas and kaons) are predicted.

Chiral partners of mesons with respect to SU(2)

The masses of up and down quarks are regarded as zero for the ideal chiral SU(2) symmetry. The mesons form isospin multiplets.

In table 3, η_{light} is a state which by construction contains only up and down quarks. η_{strange} contains only strange quarks. The physical states η and η' are linear combinations of η_{light} and η_{strange}. In principle the same applies to ω and ϕ. Here, to a good approximation the ω contains only up and down quarks and the ϕ is purely strange [Leu07a].

multiplet	partner
π	$f_0(600) = \sigma$
K	$K_0^*(800) = \kappa$
η_{light}	a_0
η_{strange}	no (singlet)
ρ	a_1
ω	no (singlet)
K^*	K_1
ϕ	no (singlet)

Table 3: Chiral partners of various mesons with respect to SU(2).

Chiral partners of various mesons with respect to SU(3)

The masses of up, down and strange quarks are regarded as zero. The mesons form flavor multiplets, namely octets and singlets. These octets and singlets mix and are therefore subsumed into nonets.

multiplet	partner
(π, K, η, η')	$(\sigma, \kappa, a_0(980), f_0(980))$
$(\rho, K^*, \omega, \phi)$	$(a_1(1260), K_{1A}, f_1(1285), f_1(1420))$

Table 4: Chiral partners of various mesons with respect to SU(3).

In table 4, the K_{1A} is a linear combination of the physical states $K_1(1410)$ and $K_1(1680)$ (see [PDG04], section 14: Quark model) [Leu07a].

The only scalar meson this work will discuss is the σ meson, all other (axial) vector mesons won't be considered, as the production threshold energy can not be reached at the MAMI accelerator.

Chiral partners of baryons

In ideal SU(2), the chiral partner of the nucleon is the $N^*(1535)$: $N \leftrightarrow N^*(1535)$

Going to SU(3), chiral partner of the ground state octet containing (nucleon, Σ, Λ, Ξ) is an octet with spin-parity $\frac{1}{2}^-$ (see e.g. [PDG04], section 14: Quark model).

For other systems, the chiral partners are not really established (see e.g. [Jid00]). For the $\Delta(1232)^+$ it is suggested there, that it belongs to a chiral quartet (concerning SU(2)). This would mean that there is not one chiral partner of the Δ, but that there are four states which belong together: $\Delta(1232)P_{33}$, $N^*(1520)D_{13}$, $\Delta(1700)D_{33}$, $N^*(1720)P_{13}$.

1.4. Chiral Symmetry Restoration

Even though the chiral symmetry is broken both explicitly and spontaneously on the hadron level, with increasing temperature or density chiral symmetry may partly be restored. The order parameter of the chiral symmetry is the chiral condensate $\langle q\overline{q}\rangle$, which has to be a function of temperature and density.

$$\langle \overline{q}q \rangle = f\,(T, \rho) \tag{2}$$

Basically all theories predict a vanishing chiral condensate ($< \overline{q}q > \longrightarrow 0$) with increasing temperature and density, see figure 8.

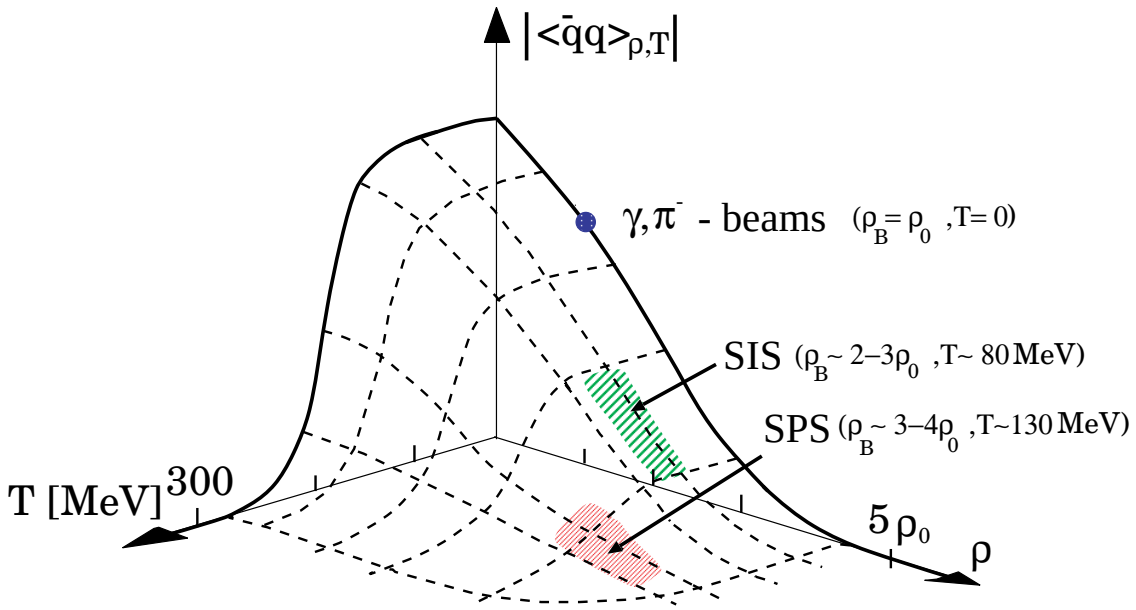

Figure 8: Chiral condensate as a function of T and p.
The plot was taken from [Wei92].

As a consequence of this chiral symmetry restoration, the degeneracy of the parity doublets like π and σ or ρ and a_1 should be recovered. High temperature can be obtained in heavy ion collisions. High density also can be generated by heavy ion collisions or choosing the experimental parameters such, that the (production and) decay of the desired particles will happen inside the nucleus. This type of reaction process is called *in medium studies*. The effect of *in medium* properties of hadrons has been promoted (e.g. by Brown and Rho [Bro91]) with the following empirical Brown-Rho scaling.

$$\frac{m^*_{\sigma,\rho,\omega}}{m_{\sigma,\rho,\omega}} \approx \frac{m^*_N}{m_N} \approx \frac{f^*_\pi}{f_\pi} \tag{3}$$

where m^* is the in-medium mass and m the vacuum value of the corresponding hadron. The dependence of the σ-mass on the density can be parameterized using equation 4, which is derived from QCD sum rules [Hat92]:

$$m^*_{\sigma,\rho} \approx m_{\sigma,\rho}\left(1 - \alpha_{\sigma,\rho}\frac{\rho_N}{\rho_0}\right) \tag{4}$$

1.5. Experimental Access to Chiral Symmetry Restoration

As the chiral condensate is not a directly accessible observable, another way to test the theories is necessary. Therefore, models are needed to calculate observable effects. In the Nambu Jona-Lasinio model [Kli90], the σ meson mass has to decrease with increasing density. It has to become degenerate in mass with its chiral partner, the pion, as shown in the left plot of figure 9.

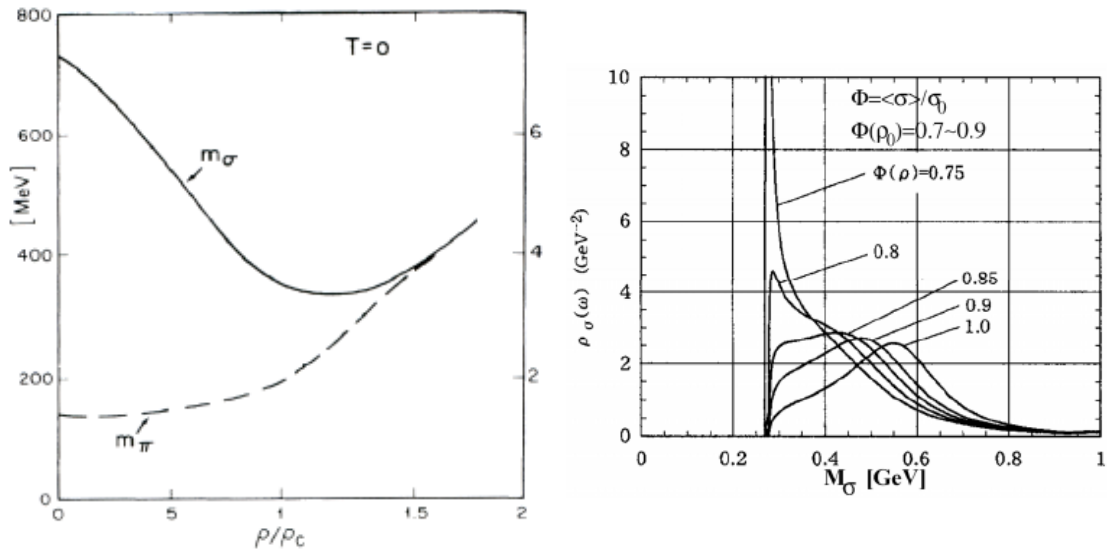

Figure 9: Observable effects of chiral symmetry restoration.
Left hand side: NJL calculations performed by Bernard et al. [Ber87];
Right hand side: Calculations performed by Hatsuda et al. [Hat99]. See text for details.

The right plot of figure 9 shows the mass shift of the σ as a function of the density. The shift can be studied, investigating the $\sigma \rightarrow 2\pi$ decay channel. As this is the dominant decay channel, a decreasing mass of the σ meson should then have effects on the invariant mass spectrum of the pion pairs.

The calculations of Hatsuda [Hat99] predict a shift in the 2π invariant mass for $\sigma \longrightarrow \pi^0\pi^0$ with increasing density. On the right side of figure 9, the 2 pion mass distribution is shown corresponding to the available phase space for different values of the chiral condensate. The curve for $\Phi_0 = 1.0$ represents the invariant mass distribution of the 2π

system in vacuum. For normal nuclear density $\Phi_{\rho_0} = 0.7 \ldots 0.9$ is expected.
In addition, the width of the invariant mass peak has to change, too. This can be explained in the following way: when the mass of the σ meson is decreasing with increasing density, the phase space for the decay particles (2π) changes. This means that less energy is available for the decay. Therefore, the high invariant masses in the spectrum are reduced in intensity. Since the lower limit of the available phase space is 2 m_π, a narrower width results. The effect can be studied by measuring the invariant mass distribution of the 2 π^0-mesons for different nuclear targets. A higher atomic number is related to a larger nucleus with a larger volume (V) and surface (S). Here the probability for producing a meson in the core is higher than for smaller nuclei.

$$\frac{V}{S} = \frac{A}{A^{\frac{2}{3}}} = A^{\frac{1}{3}} = R \tag{5}$$

In figure 10 the nucleon density distributions ($\rho(r)$) for carbon, calcium and lead are shown, derived from formula 6, where A is the atomic number and ρ_0 the nominal nucleon density [Hof57]. With increasing atomic radii the fraction of volume compared to the surface increases.

$$\rho = \frac{\rho_0}{1 + e^{\frac{r - \sqrt[3]{A}}{0{,}54}}} \tag{6}$$

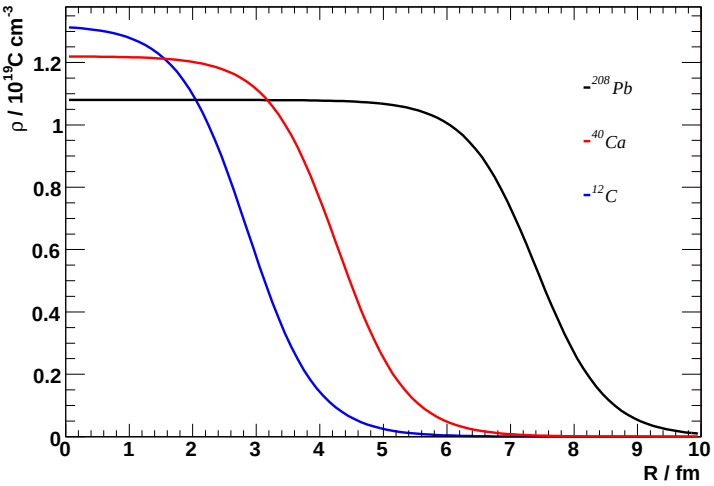

Figure 10: Mean charge density plot for C, Ca and Pb.

1.6. Photoproduction of Mesons off Nuclei and Theoretical Models

As nucleons are composite systems built from quarks, they can be excited into resonances with different subsequential decay modes. A level scheme is shown in figure 4.

Different resonance decay processes can contribute to the double pion channel with respect to the MAMI energies, see reactions 7 to 11:

$$\gamma p \rightarrow D_{13}(1520) \rightarrow (\Delta\pi)^+ \rightarrow \pi\pi N \tag{7}$$
$$\gamma p \rightarrow D_{13}(1520) \rightarrow \rho N \tag{8}$$
$$\gamma p \rightarrow D_{13}(1520) \rightarrow \sigma N \tag{9}$$
$$\gamma p \rightarrow P_{11}(1440) \rightarrow \sigma N \rightarrow \pi\pi N \tag{10}$$
$$\gamma p \rightarrow P_{11}(1440) \rightarrow (\Delta\pi)^+ \rightarrow \pi\pi N \tag{11}$$
$$\tag{12}$$

The decay via emission of the ρ and σ mesons to the nucleon ground state (with subsequent decays of the mesons into pion pairs) and the cascade decay of the resonances via the intermediate Δ resonance are listed here. The Oset model [Roc05] predicts the dominant process to be the sequential decay of the $D_{13}(1520)$ and the $P_{11}(11440)$ resonances via the $\Delta(1232)$, while the Laget [Lag03] [Lag96] model predicts it to be only the decay of the $P_{11}(1440)$ via a correlated pair of pions in a relative s-wave. In the Oset model, σ mesons are generated dynamically by 2π interaction.

There are several possibilities for photons interacting with a nucleon in the relevant energy range. The Feynman graphs considered by the Oset group [Roc05] for this reaction are shown in figure 11. The Feynman graphs l and r represent the decay of the $D_{13}(1520)$ and $P_{11}(1440)$. They are the major contributors to the cross section.
Along with $\pi^0\pi^0$, also the $\pi^0\pi^+$ and the $\pi^\pm\pi^\mp$ will be produced on the proton.

There are 6 possibilities for quasi free production of pion pairs on nuclei which follow the conservation laws, regardless of the isospin of the nucleus being scattered on:

$$\gamma p \rightarrow \pi^0\pi^0 p \quad \gamma n \rightarrow \pi^0\pi^0 n \tag{13}$$
$$\gamma p \rightarrow \pi^0\pi^+ n \quad \gamma n \rightarrow \pi^0\pi^- p \tag{14}$$
$$\gamma p \rightarrow \pi^+\pi^- p \quad \gamma n \rightarrow \pi^+\pi^- n \tag{15}$$

Because of isospin conservation and the fact that the σ has $I = 0^+$, the σ can only decay into the $I = 0$ channels listed below.

$$\underset{I=0}{\sigma \rightarrow \pi^0\pi^0} \quad \underset{I=0}{\sigma \rightarrow \pi^+\pi^-} \quad \underset{I=1}{\sigma \nrightarrow \pi^0\pi^\pm}$$

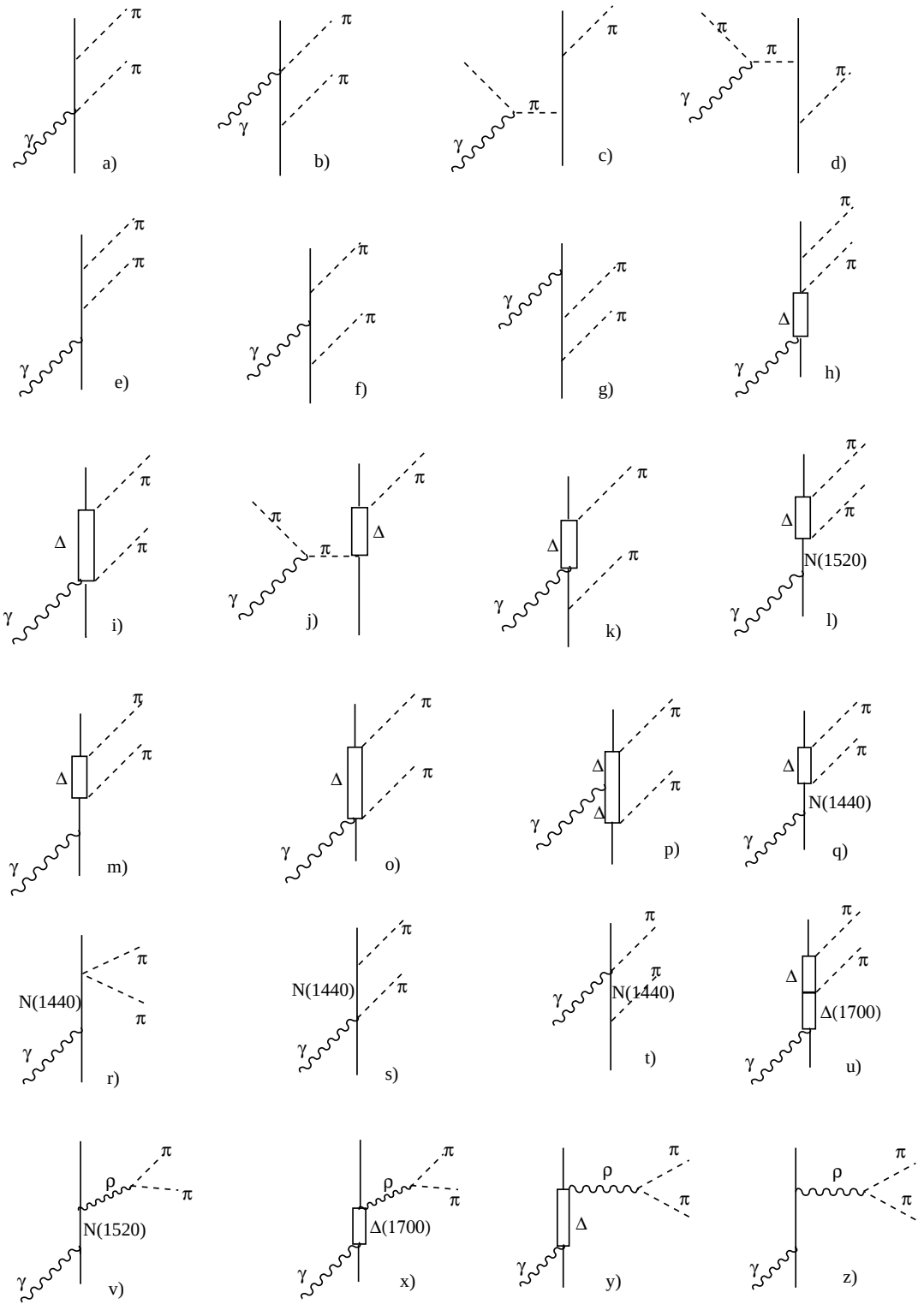

Figure 11: Feynman diagrams considered in the Valencia model.
The graphs were taken from [Roc05].

If an invariant mass shift for the $I = J = 0$ channels is measured due to the aspects discussed above, this shift should not be visible in any other isospin channel. Both channels have to be studied together and compared as a function of the target mass. In addition other effects like final state interactions can cause a mass shift because of the lowering of the kinetic energy.
Pions produced in the target can interact strongly within the nucleus or with another. They can be re-scattered and transformed into other pions by populating an N^* resonance and re-decaying:

charge exchange reactions

$$\pi^0 p \to \Delta^+ \to \pi^+ n \quad \pi^0 n \to \Delta^0 \to \pi^- p \tag{16}$$
$$\pi^- p \to \Delta^0 \to \pi^0 n \quad \pi^+ n \to \Delta^+ \to \pi^0 p \tag{17}$$

non charge exchange reactions

$$\pi^0 p \to \Delta^+ \to \pi^0 p \quad \pi^0 n \to \Delta^0 \to \pi^0 n \tag{18}$$
$$\pi^+ p \to \Delta^{++} \to \pi^+ p \quad \pi^+ n \to \Delta^+ \to \pi^+ n \tag{19}$$
$$\pi^- p \to \Delta^0 \to \pi^- p \quad \pi^- n \to \Delta^- \to \pi^- n \tag{20}$$

If charge exchange reactions occurred, the channels could get mixed up. In figure 12, the total cross section of the three channels of double pion production on the proton is shown [Kru06]. The dominant channel is the $\pi^+\pi^-$ with a production cross section of $\sigma \approx 75$ μb followed by the $\pi^\pm\pi^0$ channel with $\sigma \approx 55$ μb and $\pi^0\pi^0$ with $\sigma \approx 10$ μb at a beam energy of 750 MeV. Particles of the double-charged channel may also be transfered into the single-charged and those in turn, into the uncharged channel, which is called side-feeding.

This means, if the pions are losing energy by rescattering, the peak position and width of the measured channel will differ from the expected one, due to the rescattering process of other channels via charge exchange; or in case of non charge exchange just by inelastic scattering with the target material. Also, double charge exchange reactions have been taken into account and were calculated. However, that effect is negligible and will not be discussed furthermore. To avoid π absorption, final state interaction (fsi) of the π with any other strongly interacting particle has to be minimal. This corresponds to a maximum mean free path or high transparency, which allows the pions to get out of the nucleus with minimized fsi. This is illustrated in figure 13.

1.7. Experimental access to medium modifications

With the aim to study medium effects in a wide density range, it is necessary to have targets with different average nuclear densities. As discussed previously, the density in

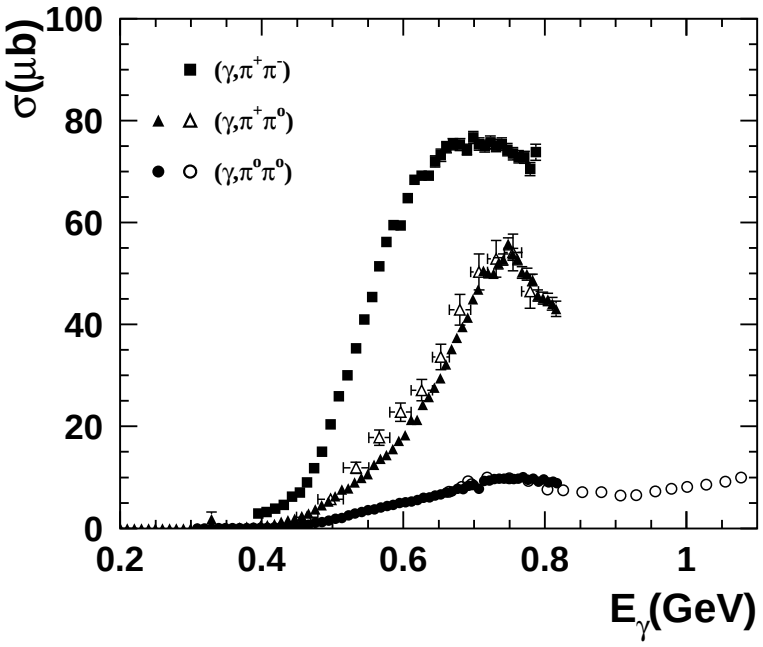

Figure 12: Photoproduction cross section for the 2π channels from the proton. The figure was taken from [Kru06].

the core is almost constant, but it decreases quickly at the surface. In large nuclei the probability of producing a pion at nominal nuclear density is higher than in small nuclei. Because of this, by choosing different targets like Deuterium, Carbon, Calcium and Lead medium effects can be probed.

In pion induced reactions, like $A\,(\pi^-, 2\pi^0)\,X$, as performed by the CHAOS- and Crystal Ball Collaboration [Bon96] [Sta00], the pion has a high probability to interact with the nucleus close to the surface (figure 13). The so called initial state interactions (isi) are of the same type like the final state interactions described above. The pion never will enter

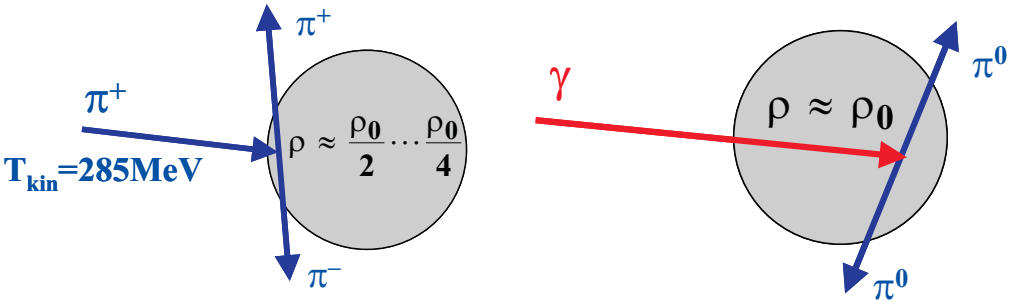

Figure 13: Interaction of pions/photons with nuclei.

deeply into the nucleus. Because of this, only surface effects can be studied with this type of experiment.
This problem can be avoided by using a photon beam. As photons do not interact strongly, they can interact at any depth of the core with the same probability in the relevant energy region.

Like mentioned before, the produced pions do interact strongly with the target nuclei. To minimize the fsi, it is necessary, that the nuclei become more or less transparent for the produced pions. In figure 14 the absorption parameter α is plotted versus the pion momentum. The maximal transparency is obtained for pions having momenta $|p| = 90 \ldots 110$ MeV [Kru95].

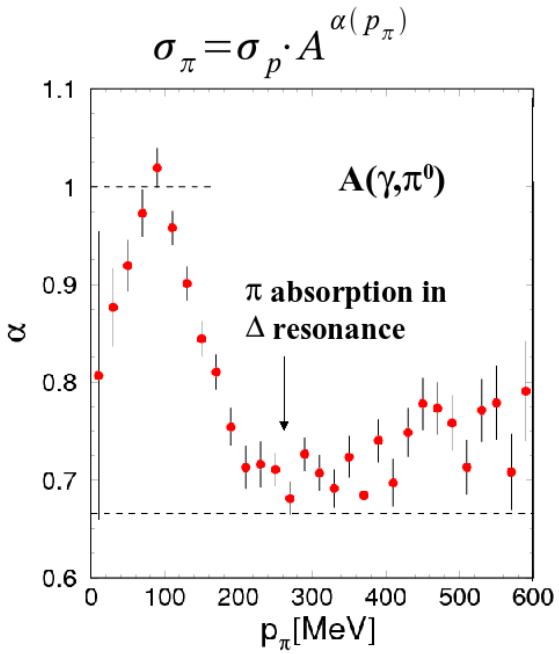

Figure 14: Absorption parameter α as function of the pion momentum for pions produced in nuclear matter.
σ_π is the inclusive pion production cross section on a nucleus with the atomic number A, σ_p represents the inclusive pion production cross section on a free proton and p_π denotes the momentum of the pion. The plot was taken from [Kru95].

To assure a maximum mean free path for the pions in the medium, the transparency has to be maximal. This leads to the following constraints for the reaction $\gamma X \rightarrow \pi\pi Y$:
Calculated from phase space, the outcoming pions have an average momentum of approximately 120 MeV for an incident photon energy of $400 - 460$ MeV. Figure 15 shows the momentum (red) and kinetic energy (black) of a charged pion from simulation in this energy range. Selecting the events with photon energies of $400 - 460$ MeV will lead to minimal final state interaction. In this way the rescattering (reactions 16. . .20) will be

minimized.

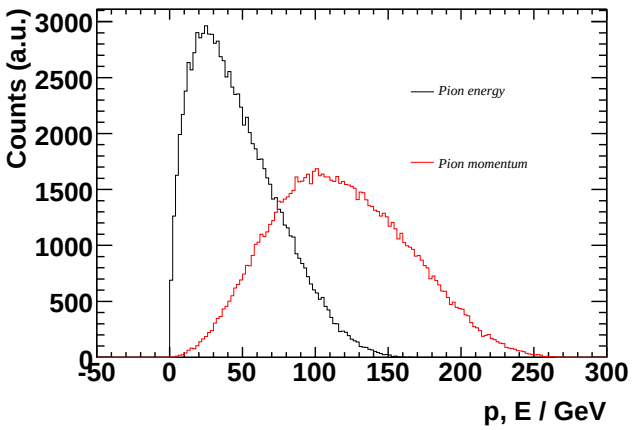

Figure 15: Momentum and kinetic energy distribution of pions from the reaction $\gamma p \rightarrow \pi\pi Y$ for $E_\gamma = 400 \ldots 460$ MeV.
The distributions were calculated from GEANT simulations, see chapter 5.

In summary, the following parameters are important for this experiment:

- A photon beam is needed to avoid initial state interactions
- The beam energy range of $400 \ldots 460 MeV$ has to be covered
- Different targets are essential to scan over a range of average densities
- To cover large solid angles, a 4π solid angle detector is needed

Experiments done by the TAPS collaboration

In addition to pioneering experiments using strongly interacting pion beams by the CHAOS collaboration and the Crystal Ball collaboration, the TAPS collaboration was the first to use photon beams to probe the whole nuclear volume. In 1999 a first measurement of medium effects has been done [Mes02], [Blo07]. For this purpose TAPS was arranged in 6 equivalent blocks and a larger wall placed in forward direction, surrounding the target as shown in figure 16.

The results are shown in figure 17.
There is obviously a shift to low $\pi\pi$ masses in the $I = 0$ channel, such an effect is not observed for the $I = 1$ channel. But due to the poor statistics, it was not possible to

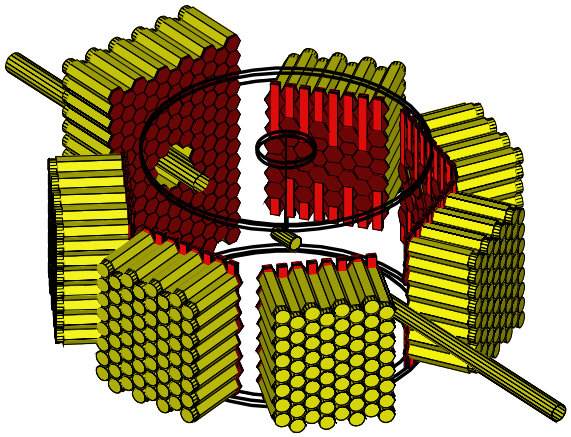

Figure 16: TAPS@MAMI - setup of the year 1999.
Shown is a schematical drawing from GEANT simulations. TAPS, consisting of BaF_2 detectors (yellow) and Vetos (red), was arranged in a 6 block structure plus forward wall around the scattering chamber (black circles), covering a solid angle of ≈ 0.4 sr.

perform some of the more restrictive cuts which could determine whether this is a trivial effect due to fsi or an effect of partial chiral symmetry restoration. Figure 18 shows the ratio $R_{Pb/C}$ between the differential cross sections per nucleon for $A =^{nat} Pb$ and $A =^{12} C$ of the reactions $A(\gamma, \pi^0\pi^0)X$ and $A(\gamma, \pi^\pm\pi^0)X$. The determined ratio $R_{Pb/C}$ in the $\pi^\pm\pi^0$ was found to be flat and a significant in-medium shape effect was observed in the ratio $R_{Pb/C}$ of the $\pi^0\pi^0$ channel.

Due to these limited statistics a new experiment was set up at the MAMI accelerator at the University of Mainz using TAPS and the Crystal Ball detector to cover almost the full solid angle.

The next chapters will cover this new experimental setup and the analysis of the data taken during that beam period.

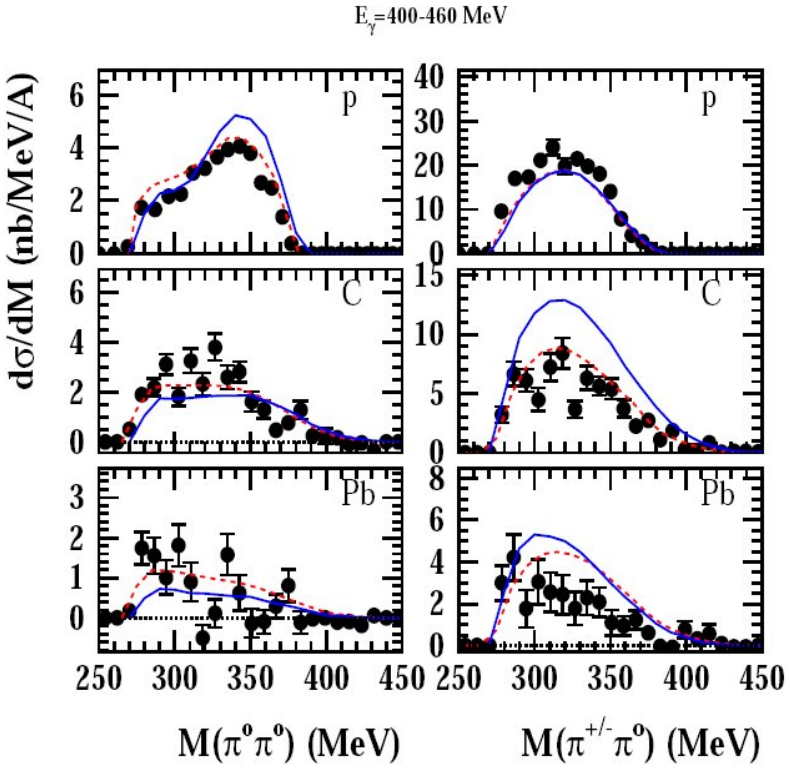

Figure 17: Results for the different targets in the range $E_\gamma = 400 - 460 MeV$, taken in 1999.
The blue solid curve shows the calculations of Roca et al, the red dotted curve shows the phase space distribution. The spectra were taken from [Mes02].

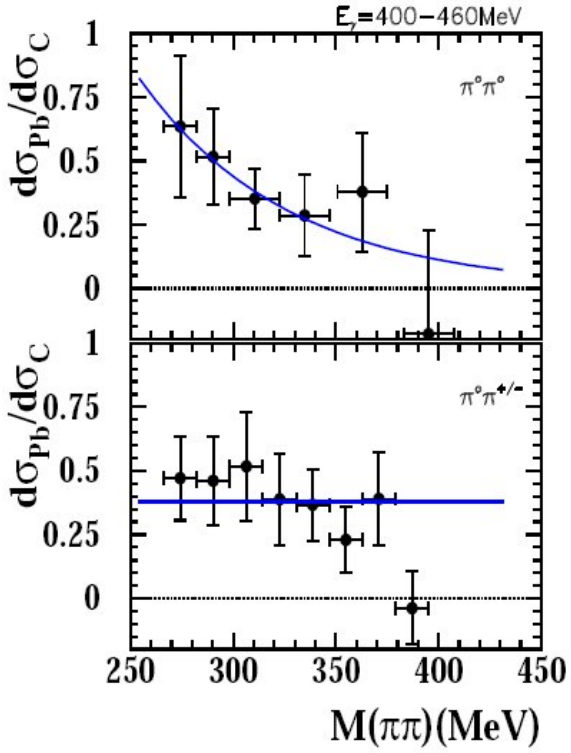

Figure 18: Ratios of the differential cross sections for Pb and C.
The blue solid line shows a fit through the data points. The spectra were taken from [Mes02].

2. Experimental Setup of CB/TAPS@MAMI

The experiments were performed in the A2 hall of the accelerator facility MAMI (MAinzer MIkrotron) of the Institut für Kernphysik, Johannes Gutenberg Universität Mainz.
Figure 19 shows the floor plan of the accelerator facility with the experimental areas.
In the following section the complete experimental setup will be described.

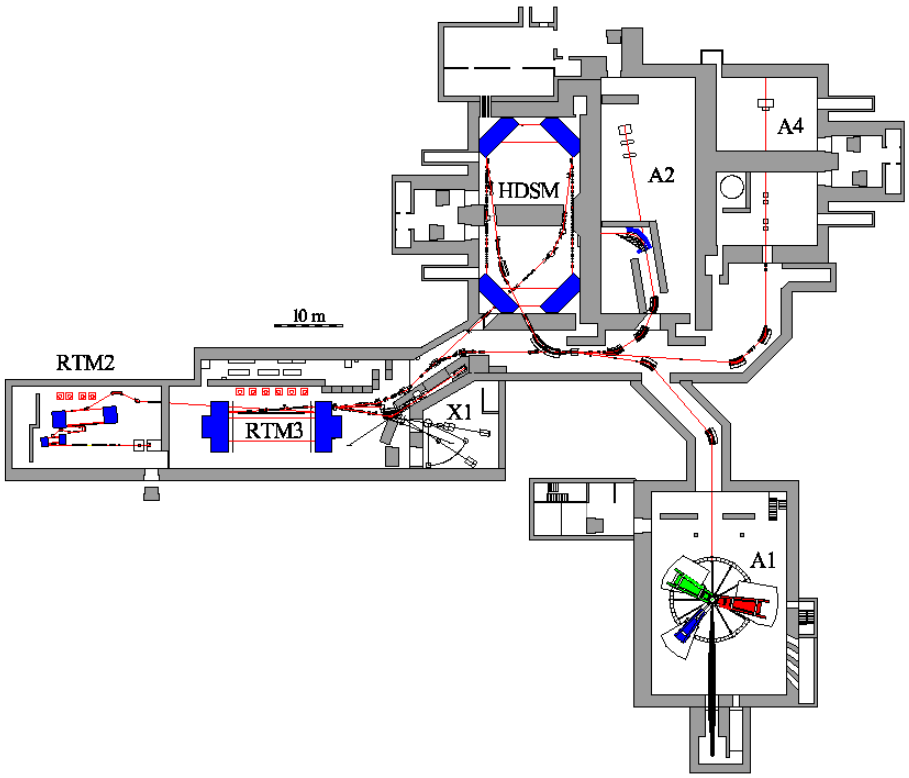

Figure 19: Floor plan of the MAMI accelerator facility with experimental areas.

2.1. The MAMI Accelerator

The MAMI accelerator is an electron accelerator facility, set up in four steps. At the beginning of the acceleration mechanism, free electrons are produced by glowing emission in which a cathode material is heated up to several hundred to approximately thousand degrees Celsius. It is also possible to produce polarized electrons. Here photoeffects are induced by focusing a polarized laser beam onto a GaAsP crystal. The electrons can leave the material (in vacuum) due to their thermal energies. A high voltage between the cathode and an anode accelerates the electrons to the anode. They form a very thin and sharp beam. Because of technical problems with handling electrical fields of more than several hundred kilovolts, the maximum energy of the electron beam is limited to 100 keV. This

	Linac	RTM 1	RTM 2	RTM 3
Injection energy	100 keV	3,455 MeV	14,35 MeV	179,5 MeV
Maximum energy	3,45 MeV	14,35 MeV	179,7 MeV	855,0 (885,0) MeV
number of cycles	-	18	51	90
dipole field	-	0,1026 T	0,555 T	1,2842 T (1,3260 T)
magnet weight	-	1.3 t	43 t	450 t
energy gain per cycle	-	0,599 MeV	3,24 MeV	7,5 MeV

Table 5: Parameters of the accelerator.

mechanism is referred to as the "electron gun". The electrons of 100 keV produced in the electron gun are accelerated to 4.0 MeV in a linear "pre-accelerator", the so called "injector linac" and then are routed into an array of three race-track microtrons (RTM). A RTM is a quasi periodic linac, meaning the electron beam is recirculated in two 180° dipole magnets after having passed the High-Frequency (HF) cavities [Ahr05]. In RTM 1 the electrons are accelerated to 14.9 MeV in 18 turns, in RTM 2 a maximum energy of 180 MeV is reached in 51 turns and in RTM 3 the electron beam can be extracted in steps of 15 MeV up to 885 MeV in max. 90 turns. Details on the accelerator can be found in table 5.
In the RTM's the electrons are fed several times through a linear accelerator section where they gain some amount of energy. The magnetic fields of the two dipole magnets are constant, so the curvature radius of the electron beam has to increase with each acceleration step (see figure 20). Therefore several different pipes are required to bring the beam back to the acceleration section. This is repeated until the maximum energy is reached and the beam is extracted to the next RTM.
The acceleration in the microtrons is done by microwaves with a frequency of 2.45 GHz in acceleration sections of about two meters length. The acceleration the electrons gain in these cavities is comparable with an electrostatic accelerator of about 2 megavolt DC [Jan05]. At the output of RTM 3 the electrons can reach a maximum energy of 855 MeV and the maximum beam current is of the order of 100 μA. At beam currents of the order of 10 nA, which is the normal order of magnitude for tagged photon experiments, MAMI is able to provide a higher beam energy of 885 MeV which mainly was used for the solid target experiments.
MAMI is a continuous wave (cw-) accelerator, it has a continuous electron beam, which is very useful for coincidence experiments. The number of random coincidences is much lower than in a pulsed beam.

At the end of RTM3 the electron beam has the following specifications:

- Cw-beam
- Maximum current of 100 μA for unpolarized and 30 μA for polarized beam
- Electron energy can be chosen between 180 MeV and 855 MeV in 15 MeV steps
- The energy is very well known: $\frac{\Delta E}{E} < 2 \cdot 10^{-4}$

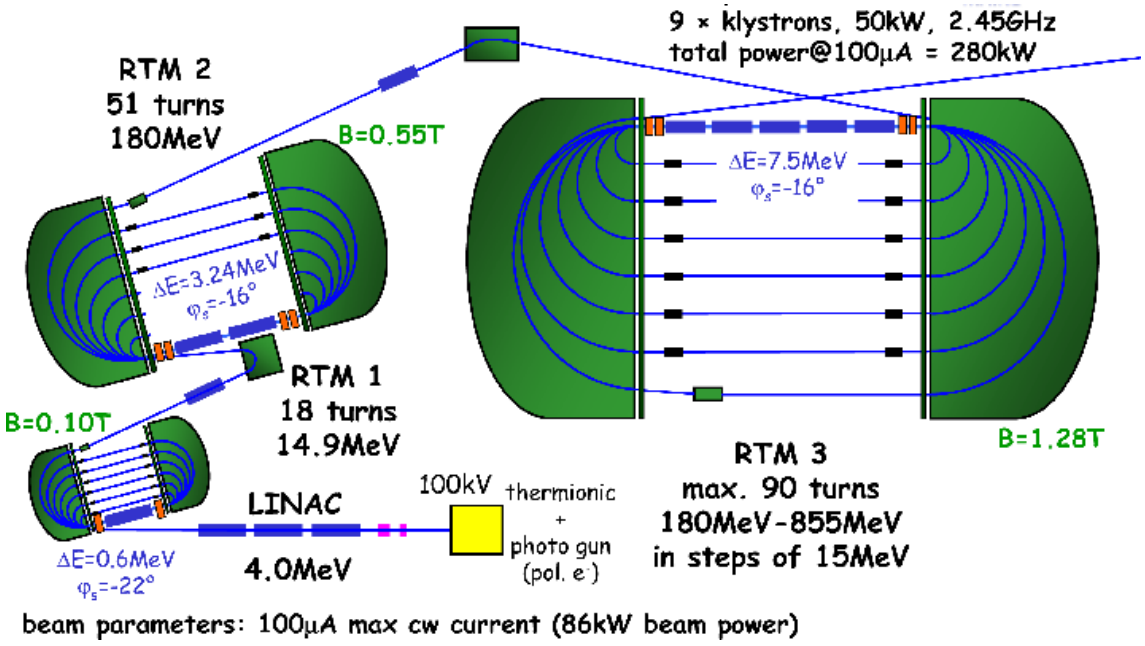

Figure 20: MAMI-B accelerator sections
The figure was taken from [Jan05].

An additional fourth accelerator section that was recently installed, reached a maximum electron energy of 1.5 GeV in January 2007. In contrast to the 3 RTM's this accelerator consists of four 90° magnets and two linear accelerator sections with two microwave frequencies of 4.9 GHz and 2.45 GHz. It is called the Harmonic Double Sided Microtron (HDSM). This facility, also called MAMI-C, began its first test experiments in spring 2007.

2.2. The Photon Beam

The electrons, accelerated in MAMI, are used to produce photons via the Bremsstrahlung mechanism. The electrons are shot through a very thin radiator foil (or a thin diamond to achieve a polarized beam). Because of Coulomb interactions with the Fe-Atoms the electrons lose energy and according to the laws of electrodynamics they emit bremsstrahlung photons. These real photons will be called a photon beam in this work; the energy of the photon beam follows a typical $1/E_\gamma$ distribution like it is shown in figure 21 left hand side. In figure 21 right plot, a tagger channel spectrum of the Glasgow-Mainz tagger is shown. In order to get the $1/E_\gamma$ distribution one has to correct for the different energy bins of the tagger elements. Also seen is the polarization peak of the polarized photons, which is not relevant in his work.

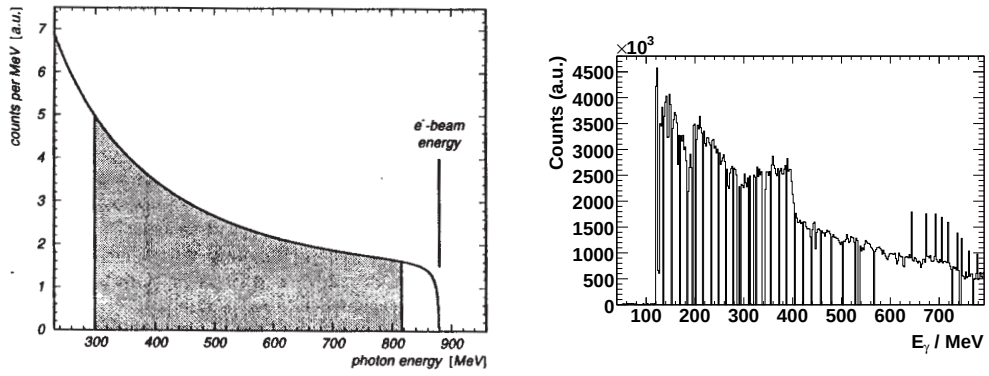

Ideal 1/E-spectrum Tagger channel spectrum

Figure 21: Ideal photon spectrum for bremsstrahlungs mechanism and the corresponding tagger channel spectrum from the analysis.
In the tagger channel spectrum, also the polarization peak is visible in the energy range of 350-400MeV.

2.3. The Glasgow-Mainz Tagger

For the analysis of the data it is necessary to know the energy of the photons in every single event. One can calculate the photon-energy (E_γ) from the energy of the incoming electron beam (E_0) and the energy of the electron after the production of the bremsstrahlung photon (E_{e^-}) measured in the tagger.

$$E_\gamma = E_0 - E_{e^-} \tag{21}$$

This equation is valid as long as the energy transfer to the recoil nucleus is negligible, which is the case for Nickel and Iron - the probability is 99% that less than 2.5 keV is transferred to the nucleus [Kru95].
The energy of the incoming electrons is determined by the accelerator group by using a flux gate magnetometer or by summing up all potential differences. To measure the energy of the scattered electrons the Glasgow-Mainz tagging facility was used in this work [Ant91] [Hal96].

In a magnetic field of approximately 1 T, in the large dipole tagging magnet, the electrons (having the charge q) are bent due to the Lorentz force. According to their momentum (p_e) the radius (R) of the curvature is unique for every single E_{e^-}/B-ratio, see equation 22.

$$R = \frac{p_e}{B \cdot q} \tag{22}$$

The electrons are deflected horizontally and detected in 352 plastic scintillators which are arranged overlapping in the focal plane. The plastic scintillators are read out individually by photomultiplier and have a width of 2.4 cm which provides an energy resolution of $1 \ldots 2$ MeV.

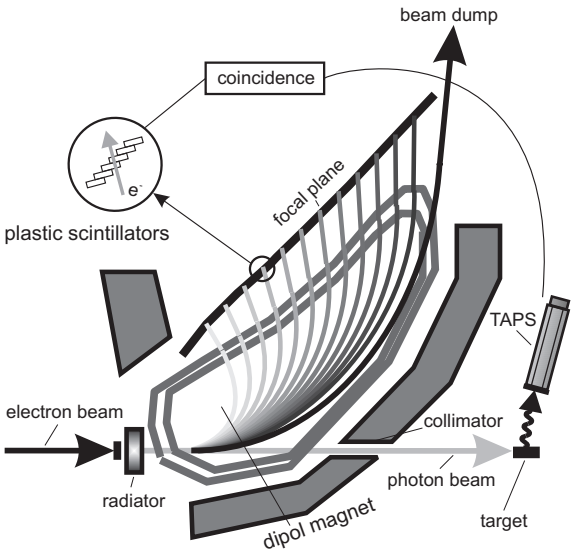

Figure 22: Schematic view of the Glasgow-Mainz-Tagger.

With this so-called Tagger the photons in the energy range of 40. . . 820 MeV (5. . . 92% of the beam energy) can be tagged. All electrons that do not interact with the radiator foil and do not produce bremsstrahlung are deflected into the beam-dump where they are stopped and neutralized.
In addition one can improve the energy resolution of the electrons by measuring the electron energy more precisely. A detector was set up called the microscope and consists of 96 scintillating fibers which are read out by 16-base photomultipliers. It covers an energy range of 65 MeV with a resolution of 350 keV [Rei99].
The photons are emitted in a light cone whose dimension depends on the energy of the beam.

$$\theta = arccos\frac{E_e}{e} \tag{23}$$

To have a small beam spot of roughly 2 cm on the targets, a lead-collimator (with an inner diameter of 4 mm which is placed 2.5 m behind the radiator, in the Yoke of the tagger magnet) was used. Due to this collimation the photon flux decreased. To obtain the fraction of photons that reach the target, the tagging efficiency (ϵ_{tagg}) is calculated as the ratio of the number of photons passing through the collimator to the numbers of electrons registered in the tagger.

$$\epsilon_{tagg} = \frac{N_\gamma}{N_e} \tag{24}$$

The photons passing the collimator are measured with a lead-glass detector placed in the photon beam which has an efficiency of 100 % for high energetic photons. The target has to be unmounted and the beam current reduced to some pA beforehand. Knowing the tagging efficiency and by measuring the count rate (or flux) in the tagger ladders,

Photon flux	$5 \cdot 10^5 s^{-1} MeV^{-1}$
Linear Polarization	$\leq 50\%$
Circular Polarization	$\leq 80\%$
Tagging-Range ($E_e = 855MeV$)	45. . . 790 MeV
Radiator	4 μm Fe
Collimator	3 mm

Table 6: Properties of the photon beam.

the photon flux at the target position can be determined, which is important for absolute cross-section measurements. The tagging efficiency is of the order of 30% for a 3 mm collimator. The tagging efficiency calibration will be described in chapter 3.3.4.

2.4. The Targets

2.4.1. Hydrogen and Deuterium Target

For the liquid Hydrogen and Deuterium beam times, the DAPHNE cryotarget system was used [Tho04]. The target cell itself, (made from Kapton, thickness 125μm) had a usable diameter of $\approx$ 24 mm and a length of 48 mm. This cell was surrounded by 8 layers of an isolation foil (8μm Mylar and 2μm Aluminum). Due to some ice growing on the exit window, an additional 10μ m Kapton cylinder was mounted around the cell. The whole cryotarget was inserted into a scattering chamber, a carbon fiber tube with an outer diameter of 82 mm and a Kapton foil as exit window.
The target gas was liquefied by adiabatic expansion from 21 to 9 bar in a heat exchanger. By this process the Deuterium was cooled down and condensed. The operation parameters of the cryotarget system were 23.5 K and 1077 ± 1 mbar resulting in a target density of 163.27 $\frac{kg}{m^3}$ [Tho07]. A detailed description of the target system can be found in [War97].

In figure 23, the result of determining the absolute dimensions of the target cell at liquid nitrogen temperatures is shown. A polaroid photograph was fixed to the outside of the beam pipe at the position of the target cell. Onto that film, a small steel plate with very precisely known holes was glued. The photograph was exposed 6 times to the photon beam at different coordinates in order to take pictures along the whole target cell (6 large circles in the photograph). Knowing the size of the holes in the steel plate, one can determine the absolute dimension of the target cell by measuring the shadowed areas.

Number of nuclei in the targets

The number of atoms (n) or molecules per unit volume can be derived from the following equations, knowing the mass number (A) and the grammage (g) (or the molar mass), the

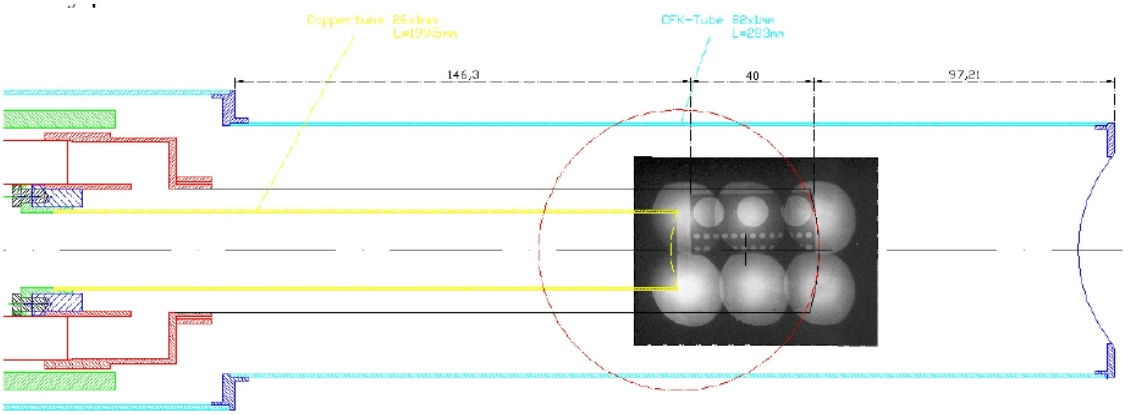

Figure 23: Hydrogen target cell, technical drawing with superimposed x-ray picture for size determination.
The picture was taken from [Tho04], see text for details.

density (ρ) and the Loschmidt-number ($N_L = 6.023 \cdot 10^{23} mol^{-1}$):

$$N_L = A \cdot g \tag{25}$$
$$n = \rho \cdot g \tag{26}$$
$$\Rightarrow n = \frac{N_L}{A} \cdot \rho \tag{27}$$

Applying this now to liquid Deuterium:

$$A = 4 \frac{g}{mol} \tag{28}$$
$$\rho_{D_2} = 0.16327 \frac{g}{cm^3} \tag{29}$$
$$n_{D_2} = \frac{6.023 \cdot 10^{23} mol^{-1}}{4 \frac{g}{mol}} \cdot 0.16327 \frac{g}{cm^3} \tag{30}$$
$$= 2.54 \cdot 10^{22} \frac{D_2 - molecules}{cm^3} \tag{31}$$

Since lD_2 molecules contain 2 d nuclei (or as the molar mass of a single D_2 atom is half of the molecule's value), the density of deuterium atoms is twice as high:

$$n_{D_2} = \frac{6.023 \cdot 10^{23} mol^{-1}}{2 \frac{g}{mol}} \cdot 0.16327 \frac{g}{cm^3} \tag{32}$$
$$= 5.09 \cdot 10^{22} \frac{D - atoms}{cm^3} \tag{33}$$

2.4.2. Solid Targets

In order to be able to insert solid targets into the beam, it was necessary to replace the cryostat, the beam pipe and also the target cell of the liquid Hydrogen target (lH_2-, re-

spectively lD_2-target).

After removing the cryotarget system, a steel pipe (DN 100) was mounted at the photon beam fitting of the tagger. A halo collimator, designed by J. Ahrends [Ahr05] was installed followed by a vacuum bellow (to align the target precisely in beam direction). The halo collimator consisted of 2 parts: A precisely adjusted part that was mounted directly into the beam pipe and a lead shield that was mounted in front of the CB where the beam pipe was fed through. This part was not adjustable and was designed to shield the ball from large angle halos, whereas the Ahrends collimator was aligned such that the beam spot only covered the target region and all other angles in forward directions were masked.
Another beampipe (3 mm thick, 70 mm outer diameter) was connected to the vacuum bellow and fed through the lead wall. In the passage of the lead shield, a three point alignment system was implemented to align the beampipe in the middle of the Crystal Ball and perpendicular to the beam axis. To minimize the energy loss a 1 mm thick carbon fiber tube was used as scattering pipe. The intersection was performed by inserting the carbon tube into the steel rod, into which two O rings were machined to guarantee vacuum tightness. The reason for this detachable connection was to keep the possibility of taking out the scattering pipe for changing the targets without unmounting the whole beampipe up to the tagger. The exit window on the downstream side was designed the same way. It consisted also of an aluminum ring with an O ring and Kapton foil glued on as an exit window. The length of the carbon tube was determined in a way that all shielding material of the exit window would be in the range of $19 \ldots 21^\circ$ in θ where neither CB nor TAPS were sensitive.
The targets themselves were mounted into the scattering chamber and held by a target holder made of 10 mm thick Rohacell plates cut into triangular shape. It had an inner diameter of 30 mm to put the targets in and an outer diameter of 70 mm to fit exactly into the carbon pipe. The whole setup is shown in figure 24.

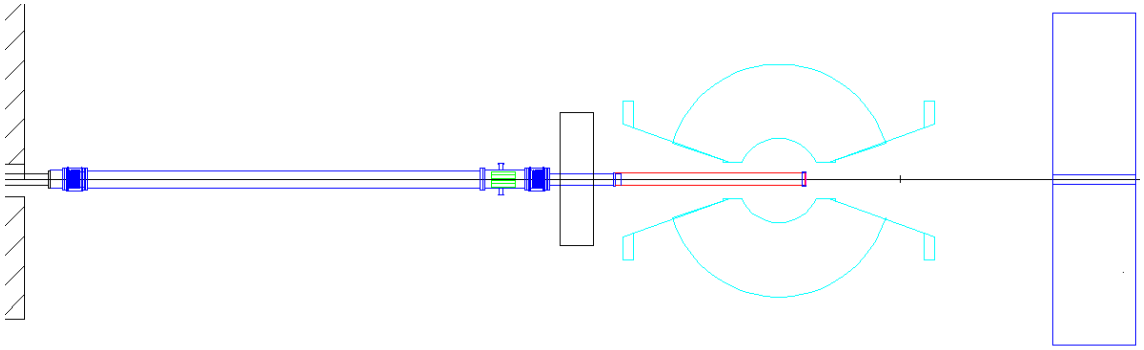

Figure 24: Beamline used for the solid target runs.
The steel pipes are drawn in blue, the carbon fiber tube is red, also shown are the halo collimator in green and the lead shield at the upstream side of the ball.

2.4.3. Target position

The absolute and relative position of the targets were determined in the following way:
Firstly there exist three different methods to determine the center of the Crystal Ball:

1. Measure the distance between the outer margins of the CB at $\theta = 0°$ and $\theta = 180°$. The median determines the center.
2. In the equatorial plane, at $\theta = 90°$, two support stilts are fixed. Perpendicular to the beam axis, crossing the connection line, another center position can be found.
3. To the CB frame, at about $\theta = 60°$ and $\theta = 120°$, some marks are attached. The crossing point of the diagonal lines drawn between, determine a third center position.

The main problem is that all three methods give results which differ by up to 2 cm.
The alignment of the cryotarget was done like described in point (3) [Kash06].
The length of the carbon pipe with respect to the position of the upstream beam rod was determined by measurements from CAD drawings. This was necessary in order to have the additional material of the exit window in the insensitive region of the setup between $\theta = 19 \ldots 21°$. Knowing the exact distance between the target position and the exit window of the carbon tube, one can insert the Rohacell target holder and position it within an accuracy of 3 mm from the downstream side.
The target changing procedure was as follows:

1. Feed a short carbon tube over the scattering chamber from the downstream side to protect the MWPC's and the PID
2. Let the photon beam pipe up to air (normal pressure)
3. Remove the scattering pipe from the steel pipe (upstream side)
4. Push the scattering pipe into the protection pipe as far as possible
5. As soon as the scattering chamber is accessible from downstream, it was carefully removed, leaving the protection pipe in place
6. Remove the Kapton window from the scattering chamber
7. Take out the target with an extraction tool
8. Insert the new target
9. Position it in the determined/calculated place
10. Reinstall the exit window
11. Carefully put the scattering chamber back into the CB
12. Reconnect it to the steel pipe
13. Evacuate the whole system again

14. When the pressure is below 1 mbar, take out the protection pipe

The setup should allow a target exchange as quickly as possible without performing a ultra high vacuum. Because of using simple O rings as connections, the target exchange was quick and easy. This setup was planned to have as little oxygen and air in the target systems possible, which serves the two purposes of preventing the metals from oxidizing and reducing the number of particles the photons can react with. With this setup a pressure of 10^{-5} mbar was reached. This was sufficient because no temperature transfer or ice growing had to be considered as for the hydrogen target.
The exact target positions was determined using the MWPC's and a program written by V. Kashevarov [Kash06]. In this way the z-vertices of the reactions in the targets were determined. In the empty target runs, the two windows of the Kapton cell were measured as a reference point. As mentioned before, the absolute position of the hydrogen target cell was exactly aligned to the geometrical middle of the CB. The middle between entry and exit window of the LD_2 cell is in the center of the CB like it is shown in figure 25 top left. Same spectra were taken for the solid targets. A gaussian was fitted to determine the relative target position with respect to the wire chamber vertex.

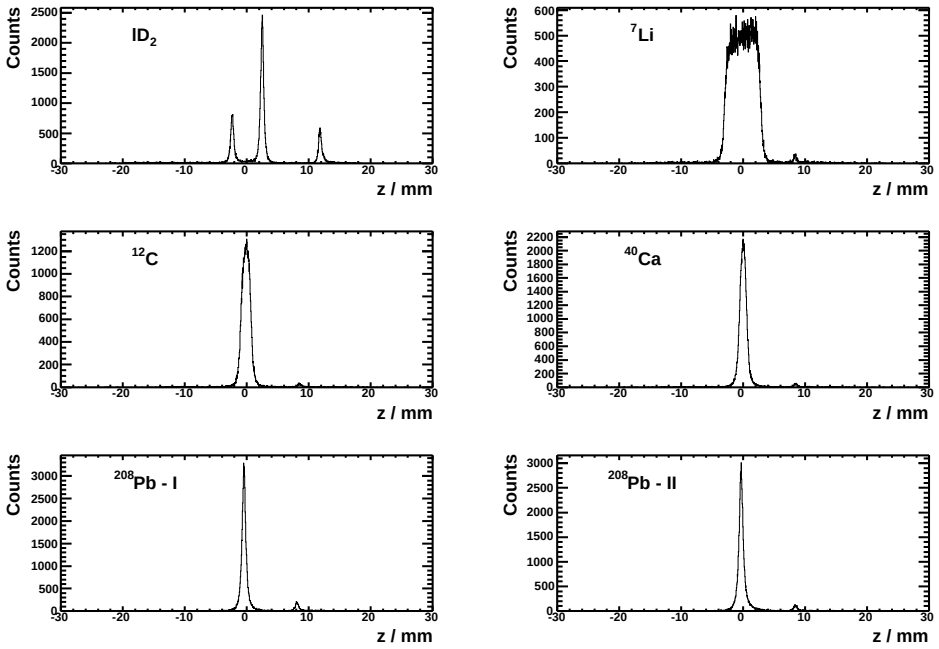

Figure 25: Position of the targets determined by using the MWPC.

Knowing the relative distance between the solid and hydrogen targets, the absolute distance to any "center" of the CB can now be determined. This makes it easy to determine

target	rel. distance [cm]	run	$d_{target-TAPS}$ [cm]
lD_2	+0,13	3738	173,17
Li	-0,03	6372	173,33
C	-0,13	6603	173,43
Ca	0,0	6563	173,30
Pb - I	-0,45	5790	173,75
Pb - II	-0,32	6677	173,62

Table 7: Target positions.

the distance between target and frontside of the BaF_2 crystals (see table 7), just by measuring the macroscopic distance between the "center" of the CB and the TAPS frontface. This value is necessary for simulation and reconstruction and was determined to be 173.3 ± 0.2 cm.

Target materials and properties

During the solid target beam times several targets were used. All solid targets had a diameter of 30 mm.

Li Target

The Li target was a 45 mm long metal bar made of natural Li (92.4 % ^6Li, 7,6 % ^7Li). It tarnishes and oxidizes as it reacts with oxygen and moisture from the air after a short time. It had to be machined under an inert protective gas and kept under vacuum during the experiment.

C Target

The C target consisted of a 15 mm graphite disc which already had been used in the CB-TAPS@ELSA experiment [Trn06] and at GSI.

Ca Target

The Ca target (97% pure ^{40}Ca) consisted of a 10 mm metal disc which had to be kept under vacuum since it also oxidizes very quickly in air.

Pb Target

The Pb target was a 0,5 mm metal foil consisting of isotopic pure ^{208}Pb from Edinburgh University.

The holding structure for the nuclear targets was developed at the University of Giessen. The relevant properties of the target are listed in table 8. For the normalization of the cross sections the number of target atoms per cm^2 is calculated. An example is shown for the Ca target:

$$N_N = \frac{N_L \cdot \rho \cdot L}{M} = \frac{6.022 \cdot 10^{23} mol^{-1} \cdot 1.54 g \cdot cm^{-3} \cdot 1 cm}{40.08 g \cdot mol^{-1}} = 2.29 \cdot 10^{22} cm^{-2} \quad (34)$$

Target	^{2}H	^{7}Li	^{nat}C	^{16}O	^{nat}Ca	^{208}Pb
Thickness $[cm]$	4.80	5.40	1.50	2.50	1.00	0.05
Density $[g \cdot cm^{-3}]$	0.163	0.534	1.67	1.0 *	1.55	11.35
Surface density $[g \cdot cm^{-2}]$	0.783	2.884	2.51	2.5 *	1.55	0.568
Radiation length $[g \cdot cm^{-2}]$	127.3	82.29	43.26	36.08	16.52	6.39
Radiation length $[cm]$	781.00	154.10	25.90	36.10	10.65	0.563
Target thickness $[\%X_0]$	6.14	3.5	5.8	6.9	9.4	9.3

Table 8: Target properties.

The radiation length of the targets has been calculated in the following way[PDG04]:

$$X_0 = \frac{716.4g \cdot cm^{-2} \cdot A}{Z(Z+1) \cdot ln(\frac{278}{\sqrt{Z}})} \tag{35}$$

2.5. Particle ID

The inner most detector in the Crystal Ball is the Particle Identification Detector (PID). It is a $\frac{\Delta E}{\Delta x}$ detector based on plastic scintillators which can be used for particle identification and to generate a trigger with a minimal time resolution of about 0.5 ns [Dow03]. Scintillating detectors have two major functions. First of all they convert the excitation energy of solid state bodies to visible light and then lightguides transport that light to a photomultiplier tube (PM). One can distinguish between organic and inorganic scintillators. The principle of an inorganic scintillator will be described in the chapter 2.7.1. The

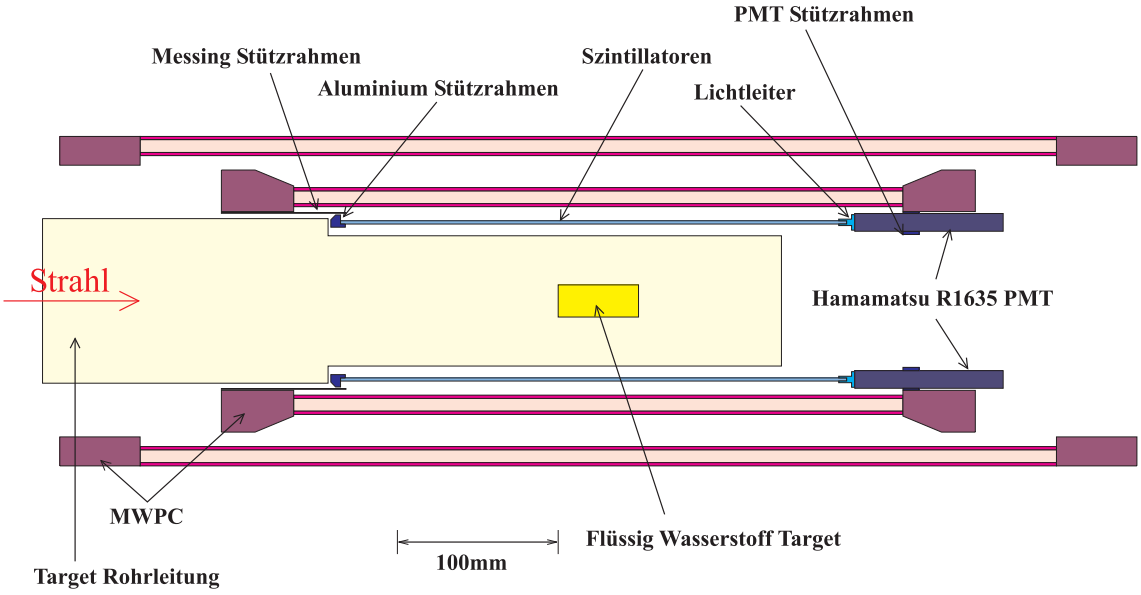

Figure 26: Technical drawing of the PID.

mechanism of organic scintillators is as follows: Energy can be absorbed by the excitation of the electron configuration of an organic molecule. When the excited state of that organic molecule relaxes into its ground state, light is emitted. Because of the energy level scheme in organic molecules with π-electron structure, the transition energies are of the order of 3...4 eV, which means most of the outcoming light is in the ultraviolet regime. Therefore, one has to add some wavelength shifting material that converts the UV light into visible light, which is much easier to register. E.g: most of the UV light would be stopped in the entrance window of the PMs because only some special and very expensive species of glass are transparent to UV light. Of course, one has to optimize the absorption wavelength of the wavelength shifter with its emission wavelength and the designated photomultiplier. An optimal position for the PID would have been between

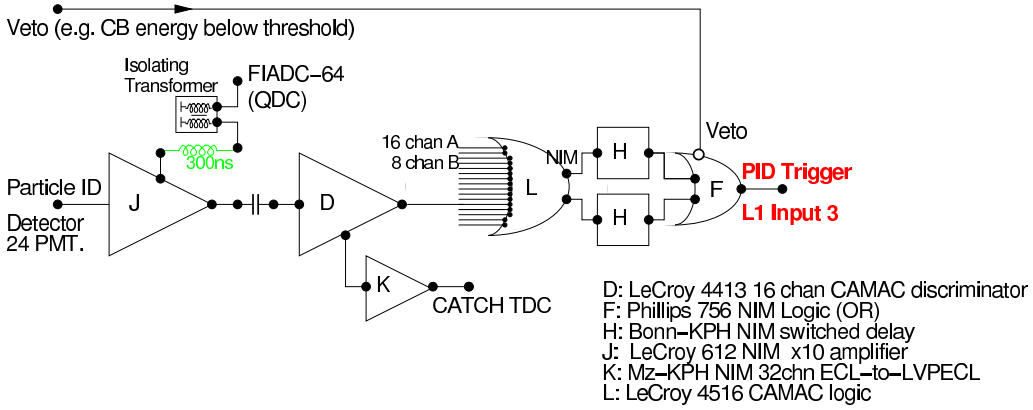

Figure 27: Readout scheme for the PID.

the MWPC's and the Na(Tl)I crystals of the CB. Because of the multiple scattering in the scintillating material the spatial resolution of the MWPC's is decreased. But as the remaining space between CB and MWPC's is only 1 mm, the PID has been manufactured as a cylinder consisting out of 24 plastic scintillators (each covering 15° in ϕ) exactly fitting in between the MWPC's and the beam pipe of the targets. The material of the scintillator strips is EJ204, with a low density and a very short time constant (0,7ns [Ann01]) as its main properties. The strips are aligned along the beam axis and coated with some reflecting Mylar foil. To prevent the scintillators and photomultipliers from seeing light, every element is wrapped in black tape. The low density of the scintillator refers to a low weight of the PID which is essential not to damage the MWPC's inside the PID. To get a high energy resolution in the PID and to keep the multiple scattering as low as possible the thickness of the strips was chosen to be 2 mm. The photomultipliers had to be connected directly to the scintillators to minimize light-loss by light guides. For spatial reasons it was also necessary to use the smallest PM-tubes available (Hamamatsu R1635 PM with Base E1761-04). The PM-tubes had to be mounted in an Aluminum support ring at the downstream end of the detector for spatial reasons, even though the forward half angle which was kept clear was decreased from 12° to 9,8°. A technical drawing of the PID is shown in figure 26. A readout of the strips from the target side was not possible because of the cryotarget system itself [Dow06]. The time and charge information of the 24 strips

are read out, amplified and split for ADC and TDC in LeCroy 612 modules. After a delay of 300 ns (see figure 27) the signals are coupled into an FIADC64 (a 64 channel fast integrating ADC built for the COMPASS experiment which is a 12 bit QDC with 64 channels in 9 U VME format). LEDs (labled as D) digitize the signals above threshold for the time measurement via CATCH-TDC's. Via the modules L (OR of 8 or 16 channels), H (adjustable delays) and F (gated OR), the OR of all 24 strips can contribute to the experiment trigger [Kra07].

2.6. Wire chambers

Two of the multi wire proportional chambers (MWPC's) with a very high spatial resolution were used as vertex detectors for the CB. These wire chambers can reconstruct both the trajectories of the charged particles that are produced in the target and their decay-products. The MWPC's working principle is derived from a proportional chamber. The simplest type of proportional counter consists of a cylindrical tube with conductive inner walls, vacuum-tight end-closures and filling of some counting gas, and in the middle of the cylinder, a very thin wire along its rotation axis [Sch06]. That wire has a positive potential compared to the cylinder. This generates a radial electrical field with a strength given by equation 36:

$$E = \frac{1}{r} \cdot \frac{U_0}{ln(b/a)} \tag{36}$$

where a is the radius of the wire, b is the radius of the cylinder and r is the radial distance of a charged particle from the cylinder-axis. At low values of the field, the electrons and ions created by the incident radiation simply drift to their respecting collecting electrodes. During the migration of these charges many collisions occur with neutral gas molecules. Because of their low mobility, positive and negative ions achieve very little average energy between collisions. Free electrons are easily accelerated by the applied field and may have enough energy to ionize gas molecules in ongoing collisions. Indeed, close to the anode wire ($20 \ldots 100$ μm), the electrical field is increasing so much that the electrons from the primary ionization processes gain enough energy to be able to ionize other atoms of the counting gas. More electrons are produced, which are also accelerated in the direction towards the wire. An avalanche is produced where the number of secondary electrons is proportional to the number of primary electrons that were produced by the initial ionizing particle flying through the detector. This concept was optimized to obtain a high spatial resolution by combining a large number of these basic elements in an appropriate way.

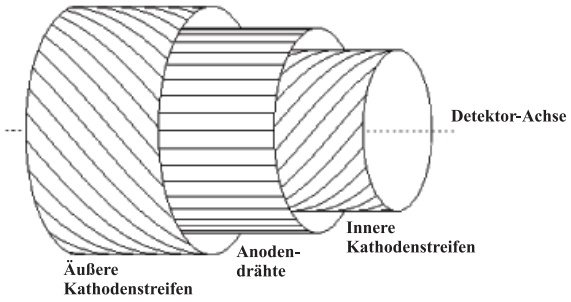

Figure 28: Schematical drawing of a MWPC.

Each of the two chambers consists of three layers. The inner and the outer layer were machined from 1 mm thick Rohacell (Polymethacrylimid [Röh01]) with a 25 μm Kapton-film on it. On the inner surface between the Rohacell cylinders Aluminum strips (0,1 μm thick and 4 mm broad) were glued. They are separated by 0.5 mm and are tilted 45° in respect to the cylindrical axis (see figure 28). These Aluminum-strips form the cathodes. The anode wires consist of tungsten-wires with a thickness of 20 μm and a separation of 2 mm, they are aligned parallel to the cylindrical axis. The residual space between the anode and cathode is 4 mm in diameter and filled with a counting gas consisting of 74.5% Argon (Ar), 25% Ethane (C_2H_6) and 0.5% Perfluormethane (CF_4). Between the anode strips and cathode wires a voltage of +2300...2500 V is applied. The MWPC's covered the whole azimuthal angle (ϕ) and a polar angle (θ) of $21...159°$. All in all 94% of the solid angle (4π) were covered with the wire chambers. Details on the MWPC are listed in table 9. A particle passing through the detector causes an avalanche of electrons which then causes a signall between the strips and the wires. From the wires one can deduce a logical signal, whereas one can get an analog signal from the strips which is proportional to the induced charge. Because of the fact that a particle flying through the detector can fire more than one strip at the same time, the resolution in space is in the order of Δx=Δy=0.1 mm.
In this setup the 480 wires are read out via 4 TDC-CATCHES, the pulses of the 320 strips are digitized by 10 iSADC cards on 2 iMUX modules, but are not used in this work (see figure 29).

MWPC	Nr. 1	Nr. 2
Length	360 mm	560 mm
Inner radius	60 mm	92 mm
Outer radius	68 mm	100 mm
Nr. of anode wires	192	288
Nr. of strips (inside)	60	92
Nr. of strips (outside)	68	100

Table 9: Properties of the MWPC.

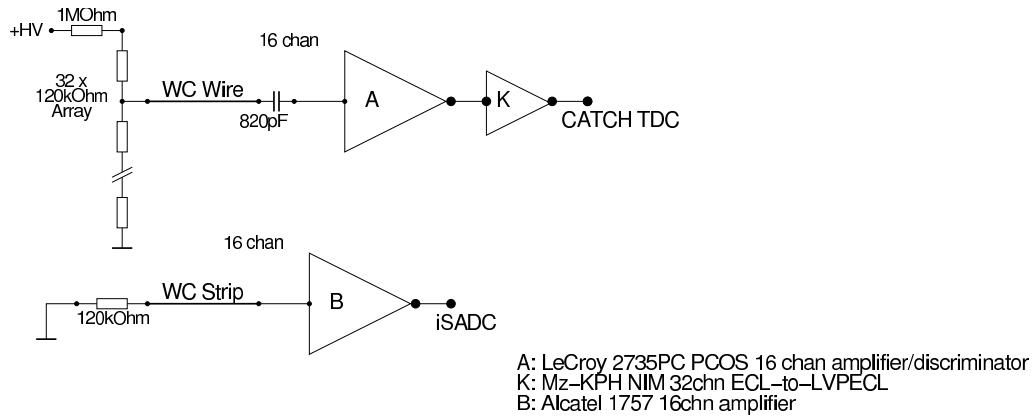

Figure 29: Readout scheme for the MWPC.

During the DAPHNE experiment the trajectories of the particles have been deduced from reading out the information of 3 MWPC's. Due to the limited space in the beam tunnel of the Crystal Ball it was only possible to arrange 2 MWPC's - the 3rd Vertex information is generated by reconstructing the cluster center of the crystal ball. With this method one can obtain an azimuthal angular resolution of $\phi \lesssim 4^\circ$ and a polar angular resolution of $\theta \lesssim 2^\circ$ Full Width at Half Maximum (FWHM). The reconstruction-efficiency for $\pi^\pm$ is in the order of 85%, and for protons it is 90% [Dow06].

2.7. TAPS

The electromagnetic calorimeter TAPS (Two Arm Photon Spectrometer) was built to measure photons and neutral mesons like pions or etas that decay into photons. It can detect and identify charged particles, which will be explained in section 3.6.3.

2.7.1. BaF_2 Modules

The TAPS detector is a modular system built out of a variable amount of BaF_2 modules. Each of the modules is built from a BaF_2 single crystal that is cut into hexagonal shape with a width of 59 mm and a length of 225 mm and a cylindrical end cap. This end cap is 54 mm in diameter and has a length of 25 mm. The photomultiplier is coupled optically by using silicon coupling grease to the crystal endcap. Figure 30 shows a schematic drawing of a BaF_2 detector. The crystals can stop $\pi^\pm$ mesons up to 185 MeV and protons up to 380 MeV [Mar98]. To minimize light loss, the crystal is wrapped into a white Teflon film, surrounded by a very thin aluminum foil. The photomultiplier (with a μ-Metal tube for shielding magnetic fields) and the wrapped crystal are combined to a complete detector module using some black shrinking tube which makes the modules light tight against external light sources. The length of 25 cm is corresponding to a radiation length of 12 X_0. The material BaF_2 was chosen because of the following reasons:

- BaF_2 is only slightly hygroscopic, thus it is easy to handle (in comparison to NaI for example)
- BaF_2 is easy to machine (using standard techniques for "processing" metal) and to create the demanded hexagonal shape
- BaF_2 can be produced with high radiochemical purity (low contamination due to radionuclides)
- It has a low cross section for thermal neutrons
- BaF_2 is resistant against radiation damages
- It is easy to heal the radiation damage by using UV light
- High light yield per MeV grants a good energy resolution: $\frac{\sigma}{E} = \frac{0.79\%}{E_\gamma} + 1.8\%$ [Gab94]
- Only a slight variation of the light output with the temperature (1.3% per 1°C) [Pfe98]
- BaF_2 has a small Moliere radius of only 4.3 cm, the electromagnetic shower only spreads over a small number of crystals
- The signal from a BaF_2 detector is shown schematically in fig 48 left side. Because of the steep rise of the signal for each detector, a time resolution of 500 ps FWHM can be achieved [Kot04].
- BaF_2 has two scintillation components with very different lifetimes, a fast component with τ=0.8 ns and a slow component τ=620 ns. These components are excited differently by photons, protons and pions. This pulse shape information can be used for particle identification. Details on this technique are described in section 3.1.3.

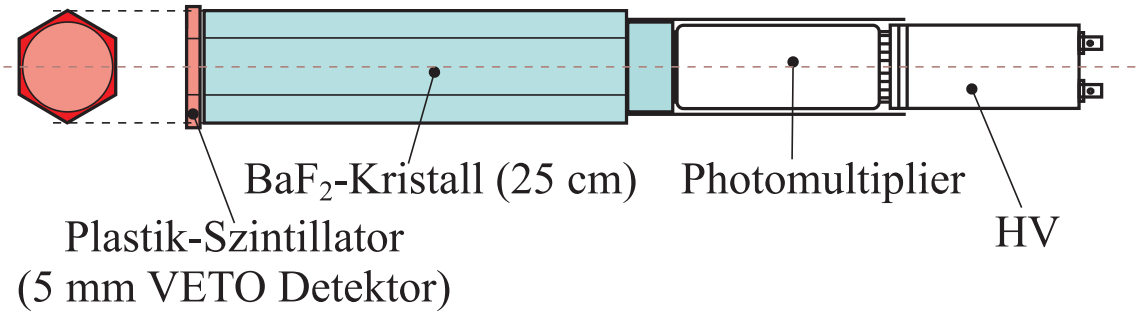

Figure 30: BaF_2 module with Veto in front.

Shower development

A shower is a cascade of secondary particles produced as the result of a high-energy particle interacting with dense matter. The incoming particle interacts, producing multiple new particles with lesser energy; each of these then interacts in the same way, a process

that continues until many thousands, millions, or even billions of low-energy particles are produced. These are then stopped in the matter and absorbed. An electromagnetic shower begins when a high-energy electron or photon enters a material. At high energy, photons interact with matter primarily via pair production. They convert into an electron-positron pair, interacting with an atomic nucleus or electron in order to conserve momentum. High-energy electrons and positrons primarily emit photons in a bremsstrahlungs process. These two processes continue in turn, until the remaining particles have lower energy. Electrons and photons then lose energy via scattering until they are absorbed by atoms like it is shown in figure 31.

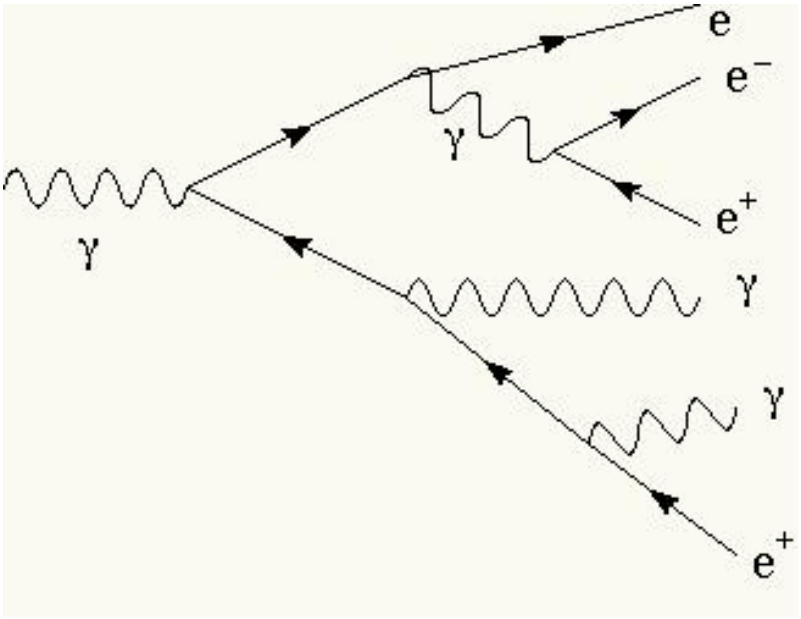

Figure 31: Development of an electromagnetic shower.

Scintillation Principle

In inorganic materials, the energy states are determined by the crystal lattice. A pure crystal has only a valence and a conduction band available, with a band gap in between them. Absorption of energy by the crystal results in the excitation of an electron from the valence to the conduction band. Then it de-excites to the valence band radiating a photon. This system is not very efficient, because the emitted photon has an energy that is far beyond the visible range. Another aspect to be considered is that the emitted scintillating light is not re-absorbed in the material. The band gap needs to be reduced in order to lower the energy of the emitted photon (close) to the visible range. This can be achieved by doping the crystal material with impurities, so called activators (see figure 32), thereby allowing a de-excitation through these sites and an increase in the probability of a photon being ejected within the visible (or in case of BaF_2 near UV) range.

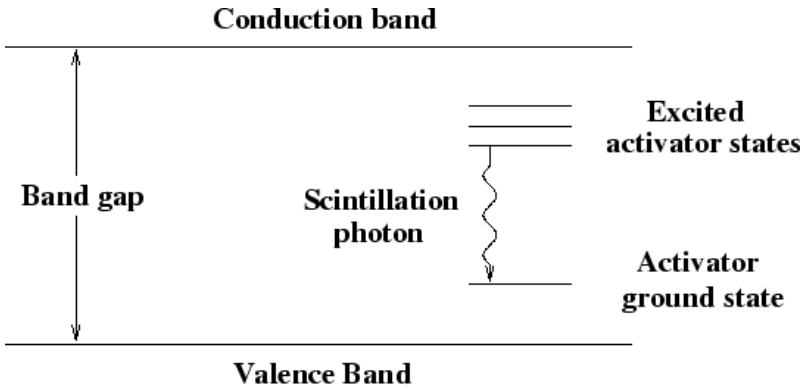

Figure 32: Scintillation principle.
See text for details.

2.7.2. TAPS Geometry

In the experimental setup CB-TAPS@MAMI 2004/05 TAPS consisted of 510 BaF_2 crystals set up as a forward wall as it is shown in figure 33.

All crystals were aligned in a huge hexagonal frame made of aluminum plates. The corners were filled up with some plastic dummy crystals, shown in figure 33 as the white hexagons without numbering. One crystal in the middle was left out as a hole for the beam to pass through. Alltogether the TAPS forward wall was aligned in 174 cm distance to the center of the target. In this setup TAPS covered an angle of $\theta = 1 \ldots 20^\circ$ and $\phi = 0 \ldots 360^\circ$. In the former experiments, TAPS was subdivided into the so-called blocks because of the characteristics of the electronic modules that were used. As this concept succeeded, TAPS stayed at this cake-piece structure like shown in fig. 33. The blocks A, C, D, E, G, H consisted each of 64 and blocks B, F of 63 crystals. This is also the structure, the hardware was designed to be.

2.7.3. The new Electronics

The new TAPS electronics is based on the VME bus-standard. One of its features / specifications is that all digitized information from the BaF_2 detector is available from one single module for at least 4 channels. It is based on a 6U-VME readout board (CAEN-V874), the so-called motherboard, and a circuit board (piggy-board) which is mounted on top of the motherboard, fitting into one standard VME slot. All electronic circuits for the readout of the BaF_2-crystals are placed on the piggyback, like the constant fraction discriminators (CFD), leading edge discriminators (LED), charge to analog converters (QAC) and the analog-digital converters (ADC). The Piggy-board contains a high-speed 12 bit ADC and a VME interface to be read out by a VME computer via the VME backplane in the crate [Dre04].

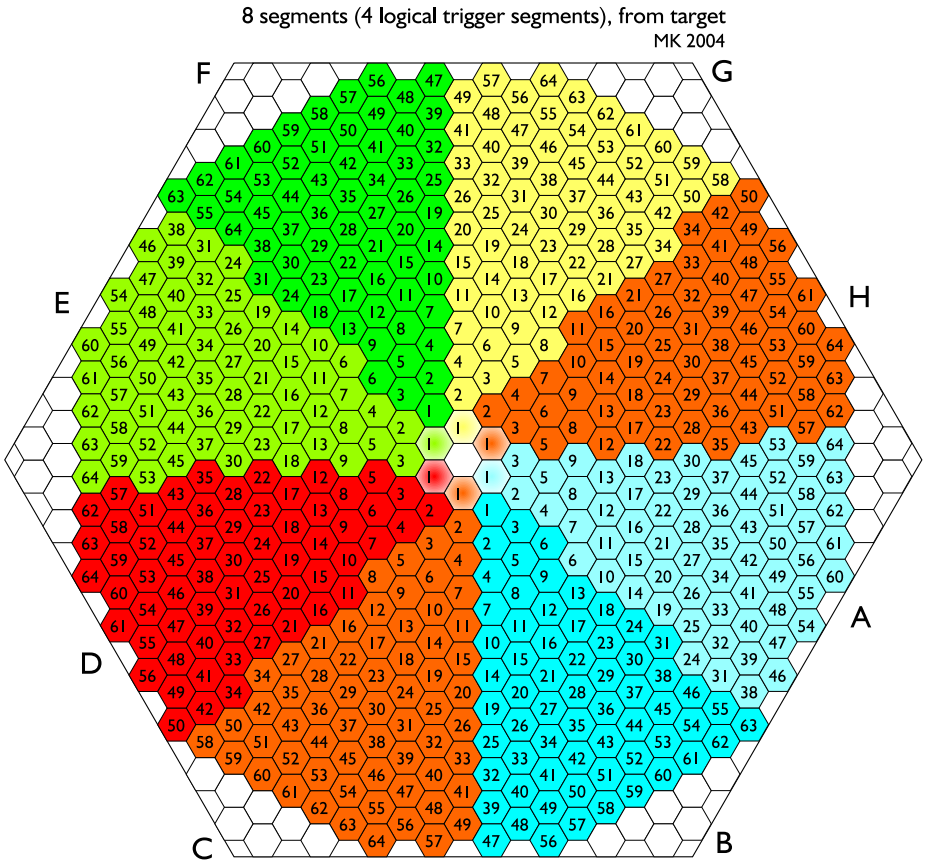

Figure 33: TAPS segmentation, view in beam direction.
The figure was provided by [Kot04].

The BaF_2 signal is distributed to the discriminators (CFD, LED1,LED2) and to 4 integration circuits QAC1, QAC2, QAC3, QAC4, like it is shown in figure 35.

All discriminator signals are fed to the front panel of the board and are connected to the logic unit of the board (PLD), which provides the integration gates and the bit pattern of the event. Also, the PLD handles the slow control of the discriminator settings, the width and timing of the integration gates, the reset function for the fast-clear, and the busy signal.

The CFD signal is the start signal for the readout; it generates an integration window of length 2 μs for the digitalization of a typical BaF_2 pulse. If the COM signal does not arrive after 750 ns, an additional "fastclear time" of 1.8 μs takes place which limits the maximum readout rate to 400 kHz. Digitalization and readout of data takes additional 10 μs. Also, a digital test pulse can simulate the CFD signal, bypassing the analog part of

Figure 34: Picture of the TAPS spectrometer as forward wall.

the readout. If the readout is triggered without having a signal coming in, the QAC's will integrate no charge, and a zero value is generated. This generates the pedestal. Simultaneously, the output signal for the multi coincidence unit (MCU) is generated.
If this trigger signal is in coincidence with the first level trigger of the experiment, a COM signal has to arrive 500 ns later in a time window of $\pm$250 ns. In the case of a positive trigger decision, the detector information of all channels are digitized and stored. This mode is called common stop mode. If the COM signal does not arrive in that time window, the readout process is stopped and all buffers are cleared.

The data is accessed by the VME-backplane on the mainboard.
In every VME-crate (which is the readout-element for a block) the following elements are arranged: A VME-computer (VMIC VMIVME7750), 16 readout-boards (64 channels) and a synchronization module (SIS 3680). In addition, there are two more VME crates

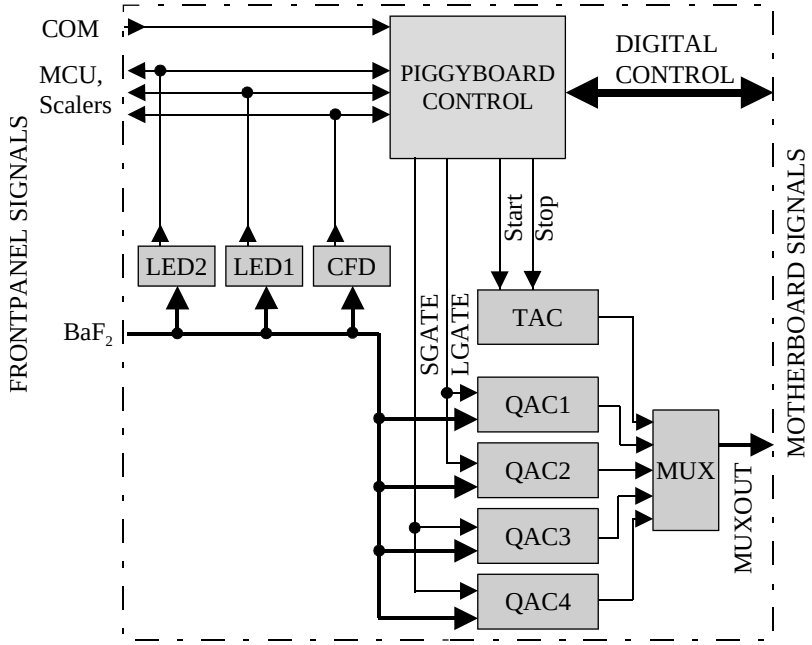

Figure 35: Block diagram of a BaF_2 readout board.

for 8 MCU's (multi channel coincidence units having 64 inputs, developed by the KVI Groningen).

Crosstalk

One of the first tests under experimental conditions was a crosstalk check. Here, the influence of the neighboring channels on the VME boards was studied. With a modified version of the slowcontrol hardwareserver any of the four channels per board could be switched off. After taking cosmic data with all possible on/off combinations an analysis of the peak position of the TDC followed. Comparing the positions with only one and several channels switched on, the crosstalk is determined. Figure 36 shows the individual crosstalk per BaF_2 channel for two, three and four channels per board activated. The crosstalk is very small, so that the coincident energy deposition in neighboring channels does not have an effect on the peak position in the energy and time spectra.

2.7.4. Computers and TFTP-Boot

For this experiment the decision was made to use VME CPU's (VMIC VMIVME7750) without local disks for the following reasons:

- One is able to change elements of the architecture, even if the machine is not running
- Due to eventual power crashes in the experimental setup, the harddisks will not be

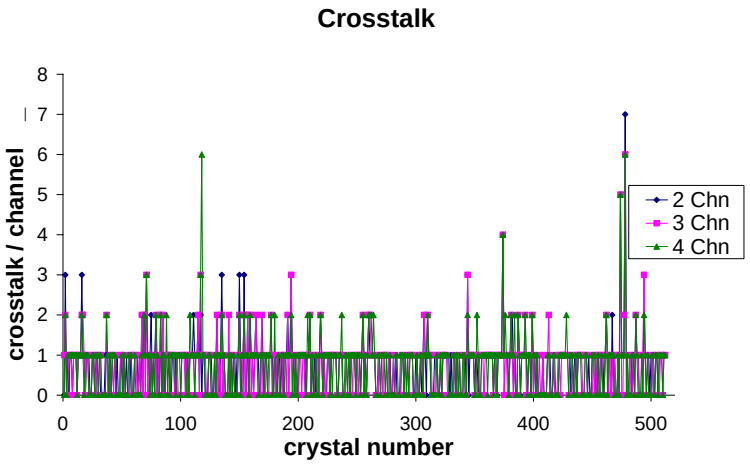

Figure 36: Picture of the crosstalk measurement
On the x axis the individual BaF_2 channel is plotted against the maximum crosstalk in TDC channels on the y axis.

affected

- Easy to expand the system to more CPU's than forseen for this experiment
- All CPU's have an identical operation system
- All self-written code will behave exactly the same on each machine
- Lower costs than having an individual harddisk for each CPU

To boot the VME CPU's without local harddisks, it was decided to use BOOTP and TFTP. The VME CPU's mount their filesystem (via NFS) from a Linux desktop computer as server (server1). This server1 was set up and connected to an optical Gigabit-Switch in the experimental hall to allow galvanic isolation between the counting-room and the experimental hall. On server1 the BOOTP- TFTP- and NFS-Server was installed.
The boot procedures go as follows:
Switching on the VME CPU, it neither knows its own IP nor that of the server. A boot request including its MAC address is sent in broadcast mode, after which it listens and waits for a reply. When the listening server receives a valid MAC address, it sends back (also in broadcast mode) the following information:

- Client MAC address (that the client knows, this package belongs to it)
- IP address and name of the client
- IP address and name of the server

- Name and path of the kernel image (that will be loaded via TFTP)
- Path of the document root (that then will be loaded via NFS)

The client compares the MAC address with its own and passes the information of the kernel image to the boot program, which afterwards contacts the TFTP server. If the TFTP server accepts the connection from the VME CPU, the requested file is sent in 512 byte blocks and stored in a RAMdisk on the VME CPU. Afterwards the boot process is executed. On boot, the filesystem is imported to the VME CPU using NFS. NFS means Network File System, directories and partitions from foreign computers behave such as if they were localized on the machine whereas they are just mounted via the network.

The kernel to boot the VME's was generated and stored to /tftpboot on the server.

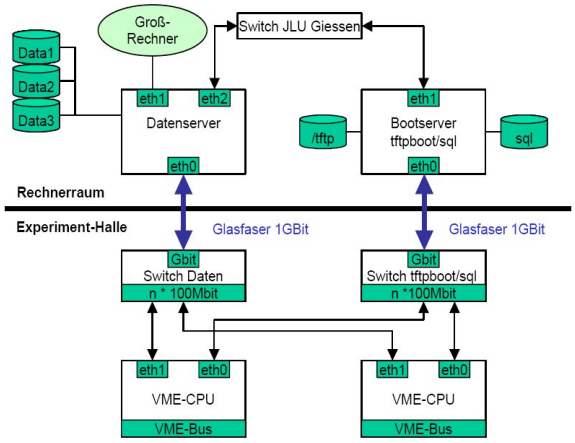

Figure 37: Schematics of the TAPS computer system.

The network cable plan is shown in Appendix A.8.

2.7.5. The new readout and DAQ

After a reaction in the target took place and a positive trigger decision was made (see section 2.9), the data stored in the NTEC boards shall be read out. To initialize the readout process, a trigger signal was distributed from the trigger logic to the CPU's in the VME crates. The CPU's read out all the NTEC boards via the backplane/VME bus system. All data stored in the NTEC boards was combined into a data packet with a unique event ID. This ID was provided by a SIS 3680 module. All the data packets were then sent to the TAPS data acquisition server (DAC server) via TCP/IP. On this server all the packets, collected from the VME-CPU's are stored. Those who have the same event ID are combined into a TAPS data packet. This packet contains all the data collected by the TAPS detector. It can then be written to disc. When TAPS is measuring in standalone mode (see energy calibration) the data are stored on the DAC server or, in the combined readout

mode, the data packets can be transfered to the global event builder, which then combines the data packets of all sub-detectors or detector elements. Here, all available data is stored together.

As described above, the data packets have to receive a number in order to identify the whole TAPS event. Therefore a master CPU in a VME crate provides the actual packet ID, which the slave CPU's receive. Furthermore the master CPU blocks all incoming trigger signals until all slave CPU's are finished with the readout and have sent the packets to the event saver. After all CPU's have sent a clear signal to the central trigger unit, the busy flag is reset and a new trigger can be processed.
The data acquisition can be subdivided into 3 parts and is based on the readout system of the CBELSA experiment [Gre07] [Sch99] [Ehm00]. These components will be described in the following.

- One event builder per CPU / VME crate
- The event saver running on the acquisition server
- An user interface to control the system

The event builder:
On each VME CPU a readout process is running which waits for a trigger signal at the entrance of the synchronization module (SIS3860). As soon as a valid trigger (see chapter 2.9) signal is detected, the trigger logic is set to busy to prevent that any other trigger is accepted or anything further is written into the buffers of the NTEC boards. Then, all 16 NTEC boards are read out by the CPU (common stop mode). When the readout process is finished, all data in the buffers of the NTEC boards is cleared and the busy flag is reset. As described above, the data packets have to receive a number in order to combine the whole TAPS event. Therefore a master CPU provides the actual packet ID, which the slave CPUs receive. All data read out from the NTEC boards is combined to a block event with the ID in the header. These block events are then sent to the event saver via fiber-optics-gigabit Ethernet. After the data transfer is finished, a 2 bit finish-flag is set on the sync module. The master CPU is blocking all incoming trigger signals until all slave CPU's are finished with the readout. Having sent the packets to the event saver and all finish-flags have been received in the master-sync, the inhibit is reset. The TAPS busy is cleared, new trigger signals are accepted and a new readout cycle can begin.

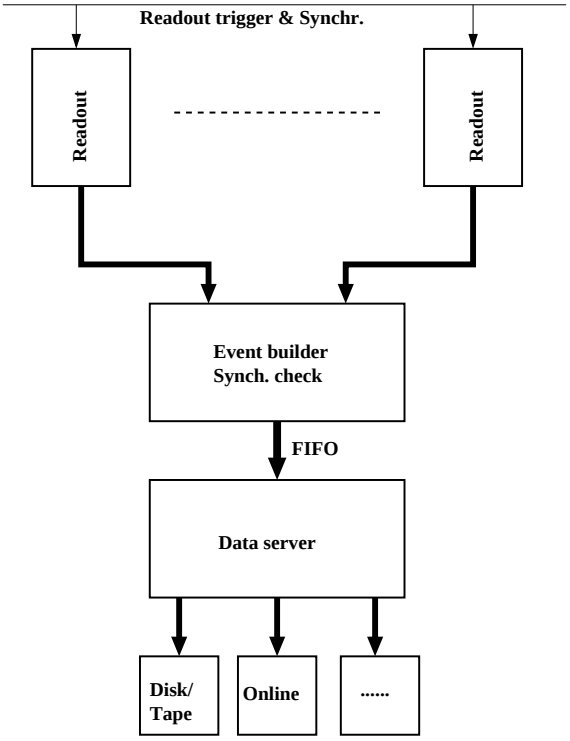

Figure 38: Concept of the TAPS readout.

In the combined mode the master sync sends the event-ID and the busy/clear flags to Acqu to ensure synchronization of the two independent (TAPS and CB, Tagger) acquisitions to Acqu and to guarantee the same event numbering. The individual dead times are also shared to consistently run both acquisition and trigger.

The event saver:
The event saver collects all data packets coming from the event builders and combines the packets with the same ID into one TAPS event. This program runs on the acquisition server, where it can directly write the events to disk or pipe them into the connected Acqu system. Because Acqu has also the same event ID's like TAPS, all data packets coming from any sub detector system can be combined to the whole event.

The user interface:
The program "donald_gui" running on the "SlowControlServer" (server1) was used as user interface. In principle it has several functions: In standalone mode one can choose the path/name to store the data. In the standalone mode as well as in the combined mode one can start & stop the data taking. This program ensures the synchronization between the TAPS event saver and the global readout system, and it also automatically starts/stops the data taking by receiving control flags from the master system in standalone mode.

When data taking is being activated, donald_gui connects to all VME CPU's and the event saver in order to start the necessary processes for reading out data. The event builders are accessing the VME backplane in the same way as the slow control, because of this they

can only run in an “exclusive or” mode to avoid errors. As a consequence, by switching on the acquisition, all slow control processes will be killed immediately.

In the combined readout mode all TAPS triggers are blocked while the whole system is busy. If one wants to switch to standalone mode, one has to switch off the busy-flag from the CB system because the triggers are then only provided by TAPS.

2.7.6. Slow control

To initialize the hardware and to set or change thresholds for the discriminators, adjust the pedestal position of the ADC’s, or to set the high-voltage of the detectors, an interface “slow control” is needed. All these parameters and the location of the modules (unique ID) are stored in a MySQL-database on a personal computer, the slow control-server. This server is a Pentium4, 2.4 GHz with 2 hard disks and 512 MB RAM, 1 Ethernet- and 1 fiber optics network connector and SuSE Linux 8.2 as operating system (called server1). The computer is installed in the counting room and is connected to a switch in the tagger hall. All VME-computers are also connected to this switch. On one of the hard disks every VME-CPU has an image which is loaded into the RAMDISK of the VME-CPU via TFTP-boot (see section 2.7.3). This technique has some advantages. Even if the VME-CPU is not switched on, one can access its hard disk. There is no limitation in disk space (like if using Compaq-Flash cards) or space in the VME-crate (using normal hard disks). Furthermore this setup makes it much easier updating the system. On the server a program, called “Taps-Server” is running which is responsible for communication with the MySQL database and the VME-CPU’s via TCP-protocol. The user interfaces are the client programs that allow the programs on the hardware side that communicate with the Taps-Server are called “Hardware-Server”, “HV-Server” and “Veto-Server”, see figure 39.

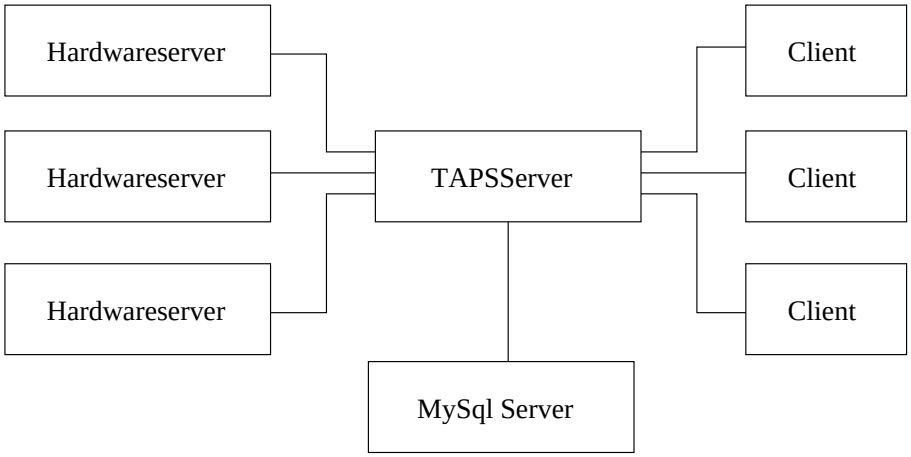

Figure 39: Concept of the TAPS slowcontrol.

The Hardware-Server is running on each VME-CPU. After switching on the VME-crate

or booting the CPU, the Hardware-Server is started automatically. The Hardware-Server first tells the crate in respect to the IP of the CPU which block it is logically assigned to. Then it sends a request to the Taps-Server to initialize all modules in this crate. The Taps-Server reads out the requested data from the database and sends back the detector settings for the BaF_2-boards. Afterwards the program is no longer needed. One can switch it off or let it remain in the background (e.g. until new thresholds will be set). It is also used to adjust the QAC pedestals when new boards are inserted. The Hardware-Server can just write values to the chosen channels, but from the NTEC hardware side it was not forseen to read them back.

The HV-Server is running on one VME-CPU and communicates with the LeCroy 1440-HV via Daisy-Chain. In this case the communication with the modules is realized via RS232. As the HV-crates have their own memory chips implemented, it is not necessary to initialize all modules by switching the crates on. This is a great advantage because of the crates' slow response to the LeCroy 1440 mainframes on the serial port. The HV-Server can read/write from the hardware and also from the database.

The Veto-Server is in some sense a mixture of Hardware-Server and HV-Server. It initializes the settings of the veto CFD's and can also read the values back. It runs on the same VME-CPU as the HV-Server (but not at the same time), thereby controlling the old CAEN TAPS CFD's (Ganelec FCC8) in the CAMAC-Crates via VME $\longleftrightarrow$ CAMAC interface over the VME-backplane and a CAMAC-branch-driver (CBD8210 & A2-controller) using the well known CNAF commands.

To switch off single detectors contributing to the trigger, their channels can be masked with the shell script SetMCU. This script manages the programming of the MCU's, explicitely which LED- or VETO- contributed to the TAPS trigger. This masking was used for the inner most rings of TAPS because of the particles being produced in non hadronic background reactions are boosted to very small angles.

For users the following clients can be used to change thresholds, pedestals or the voltages: One method to communicate with the Taps-Server is the program talk2server, which is in a command-line architecture. A short "how-to" will be given in the appendix A.1. The HV-talk is also a command-line program. With this program one can monitor much faster the HV-status, see appendix A.2.

An optional graphical user interface called Tatui (TAPS Tune User Interface) is available which also runs on the server. This program is able to read and write any valid value to the chosen detector module, either one by one or block-wise, with or without storing the values to the database.

As soon as a new BaF_2-readout-board is inserted, the following steps have to be completed:

- Ensure that the VME-Base-Address is correct
- Switch on test-pulser to rate of $\sim$ 1 kHz

- Call */taps/TapsD* on VME4 to clear the busy flag
- Run *Hardware-Server -testqac #* (board-number) to set the pedestal
- Store the values to the database
- Update the MySQL database with the specific minimal CFD-thresholds of the particular board provided by the electronic workshop
- Start the Hardware-Server in normal mode

A detailed description is found in appendix A.4.

2.7.7. The Charged Particle Veto

To distinguish between charged and neutral hits, a 5 mm thick hexagonal plastic scintillator sensitive only to charged particles (Type NE 102A), the Charged Particle Veto (CPV) or Veto for short was positioned in front of every single BaF_2 module. These vetos were mounted in a box consisting of an aluminum frame with a 1 mm thick PVC front plate. On a 3 mm thick rear plate the Vetos were directly glued on. The vetos were also wrapped into Aluminum foil to minimize light loss. To get each module light-tight, some layers of black-tape were glued onto them. Figure 40 shows a picture of the complete veto wall. To read the veto information out, a slit was machined into the vetos, where a signal wave-

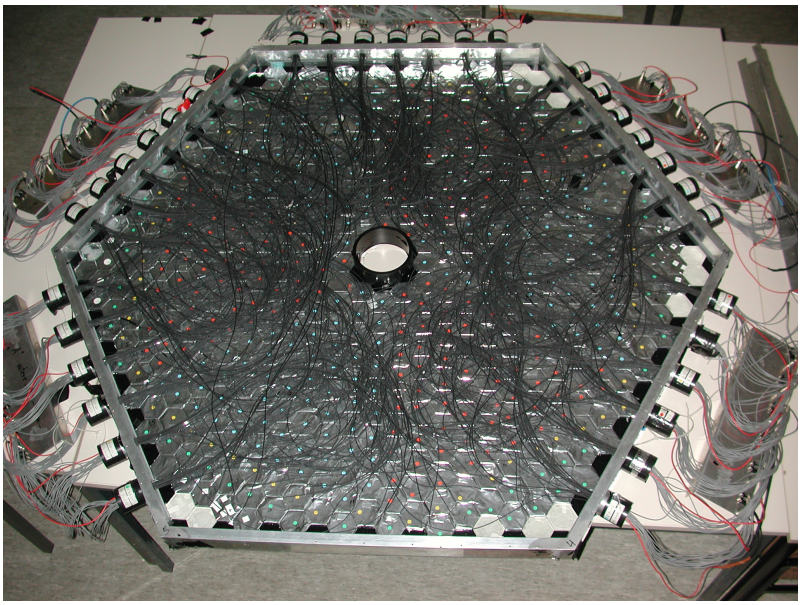

Figure 40: Photograph of the aluminum frame with veto detectors and lightguides inside.

length shifting fiber light-guide (Bichron BCF-92) was glued in. The other end of the light-guide was coupled to 16-fold photomultiplier (Hamamatsu H6568). In total there were 33 PM's installed on the outer side of the aluminum frame [Jan00].

The outputs of the PM's were connected to the inputs of 16 fold CFD's (Ganelec FCC8). The threshold value was chosen to be slightly above noise, so as to detect slow charged particles that got stuck in the plastic without giving a signal in TAPS. This digitized information (whether a channel fired or not) was given to coincidence registers (LeCroy 4448). The BitPattern of the events coming from the coincidence registers was read out via the CAMAC backplane by an A2 Controller and CBD8120 by the Crystal Ball acquisition. This had the advantage of keeping the TAPS acquisition in VME standard whereas for the CB, CAMAC readout was widely used.

2.8. Crystal Ball

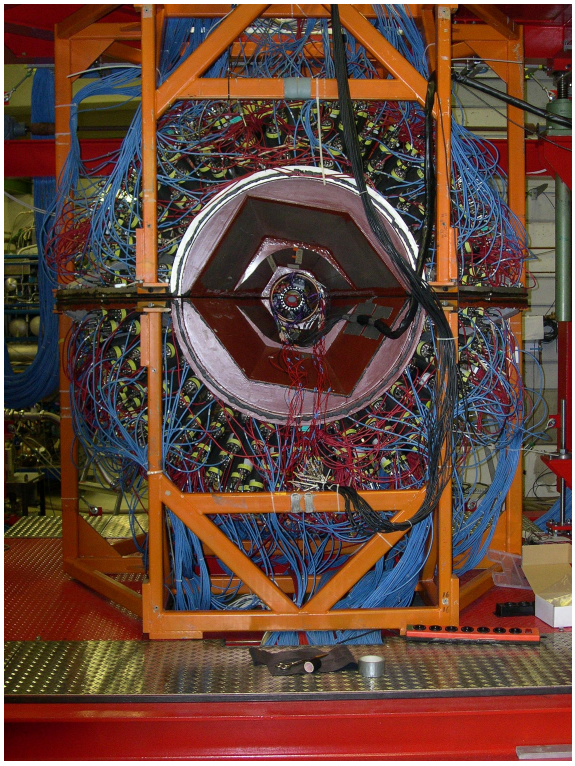

Figure 41: The Crystal Ball with the MWPC inside.

The Crystal Ball (CB) is a spherical modular Na(Tl)I-detector. The fundamental geometric object is a platonic body with 20 identical surfaces: an icosahedron. The 20 triangles forming that icosahedron have identical properties in length and are called major triangles of the CB. Each of the major triangles is subdivided into 4 equilateral triangles, the minor triangles, which consist of 9 Na(Tl)I-crystals with triangular shape. The surface of the sphere consists of 720 elements. As the CB was designed to be used in collider experiments, two hexagonal parts on opposite sides of the detector were not filled up with detectors. Here the beam pipes of the storage ring had to be fed through. The size of these

hexagonal holes is 24 detectors each, so that the total number of detectors is 672 with an solid angle acceptance of 93% of 4π [Cha76].

2.8.1. NaI Detectors

The basic form of the crystals is a frustum of pyramid in triangular shape. To be able to align the icosahedrical form as close as possible to an ideal sphere, 11 slightly different crystal forms are used. The crystals are 40.6 cm long (15.7 X_0), the length of the inner base is 5.1 cm, the outer base is 12.7 cm in length. With these dimensions, the crystals can stop $\pi^{\pm}$ mesons up to 240 MeV and protons up to 425 MeV. Typically 98% of the transverse dispersion of a shower will be deposited in an array of 13 crystals [Nef95]. For optical isolation the crystals are wrapped in 150 μm paper and 50 μm aluminum foil to minimize insensitive material and energy loss between the crystals. More properties of the CB are listed in table 10, the segmentation of the Crystal Ball is shown in figure 42.

azimuthal acceptance	$1,2^\circ \leq \phi \leq 178,8^\circ; 181,2^\circ \leq \phi \leq 358,8^\circ$
polar acceptance	$20^\circ \leq \theta \leq 160^\circ$
azimuthal resolution	$\sigma(\phi) = \frac{2^\circ \ldots 3^\circ}{sin\theta}$
polar resolution	$\sigma(\phi) = 2^\circ \ldots 3^\circ$
crystal length	15,7 X_0
energy resolution	$\frac{\sigma}{E} \approx \frac{2\%}{\sqrt[4]{\frac{E_\gamma}{GeV}}}$
time resolution	1 ns FWHM (has not been reached, see chapter 3.2.2)

Table 10: Properties of the CB.

2.8.2. Geometry of CB

The CB is assembled in two hemispheres. The outer wall of the hemispheres is made of of 25 mm Aluminum and has an outer diameter of 66 cm. The inner wall's diameter is 50.8 cm and it is made of 3 mm stainless steel (0,09 X_0).

The hemispheres are capsuled hermetically with a lower pressure inside to prevent damage of the hygroscopic crystals due to humidity. Stability is increased with stressing steel rope strings between the inner and outer cones. Both hemispheres can be adjusted separately around the center of the target. In addition, the upper hemisphere can be lifted via a motor controlled gear. An inactive area of $1.6\% \cdot 4\pi$ remains in the equatorial plane because of a 5 mm gap between the hemispheres and the 3 mm stainless steel walls of the hemispheres. The polar acceptance is restricted to $20^\circ \leq \theta \leq 160^\circ$ because of the entry and exit opening of the beam tunnel.

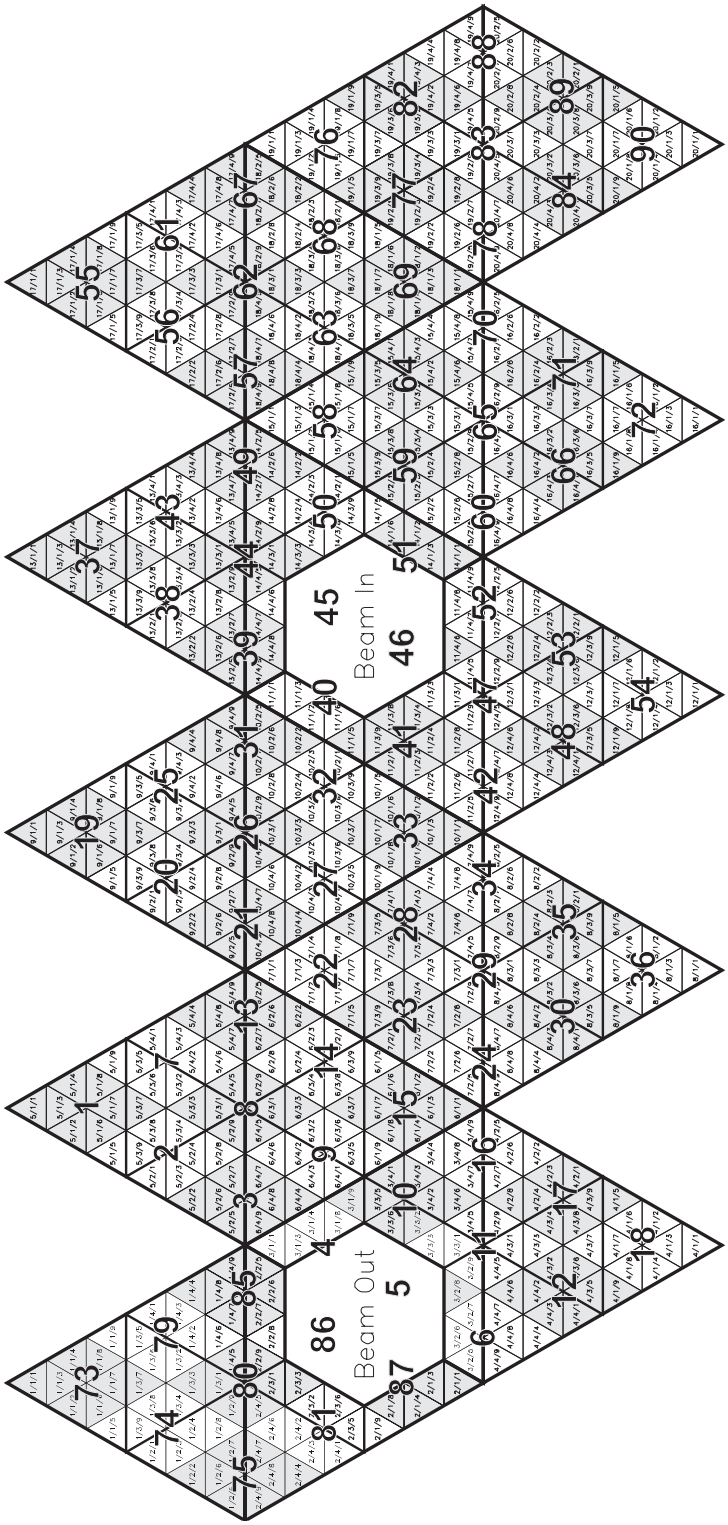

Figure 42: Segmentation of the Crystal Ball.
The large triangles are the major triangles, those numbered from 1...90 are called minor triangles and the small ones are the crystals.

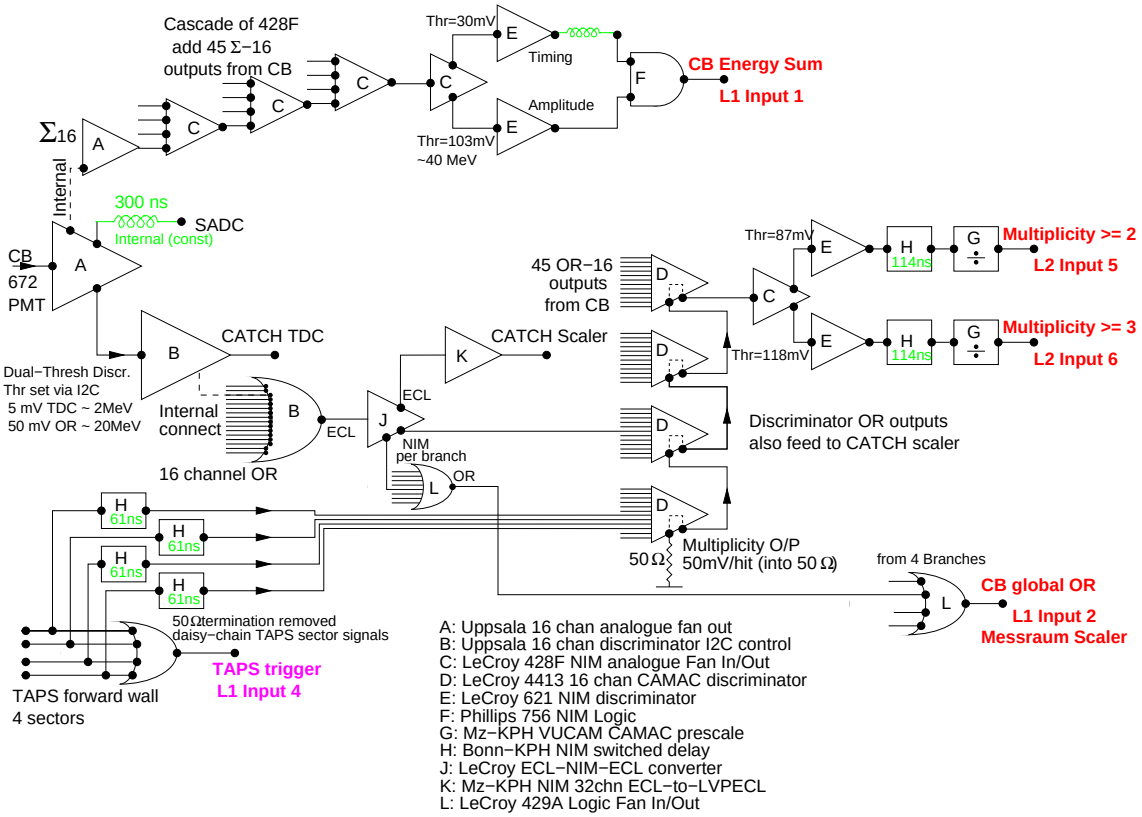

Figure 43: Readout scheme for the CB.

2.8.3. Readout Electronics

Figure 43 shows the readout components for the CB in a schematic way. The signals coming from the CB are transfered to active splits using 124 Ω-cables. Each split sums up the signal over two times eight channels, providing the energy sum as global trigger as energy sum. One 16 channel output is directly connected to the discriminators, and another is delayed by 300 ns and connected to the ADC's. The discriminator module has two discriminators with individual thresholds per each channel. One threshold is set slightly above the electronic noise to provide the time information for the CATCH-TDC's, the other one is forseen to provide the cluster multiplicity signal.
The ADC's and TDC's are scanning the signal continously; they are "running freely", no gate signal has to be provided. The experimental trigger is distributed by the trigger control system (TCS) to all frontend modules. In case of a positive trigger decision, the data buffer of those modules are passed to the next acquisition instance. The data is stored in temporary buffers, and from there it is read out by the processing computer via VME bus. The ADC's are VME cards, and thus do not have a possibility to communicate via VME bus or S-Link. A special multiplexer (GeSiCA or iMUX) is needed to control and read out the eight ADC modules.

All signal amplification is realized by SRC L50B01 photomultipliers in combination with a voltage divider, which was specially developed for this detector. All voltage dividers are operating with +1500 V anode voltage. The gain is adjusted with a potentiometer between the 3rd and 4th dynode such that the energy information for identical energy deposition in the crystals is alike [Kra07].

To reach high trigger rates, it is necessary to eliminate long dead times during data acquisition. The readout computers are operating with a real time operating system (Lynx OS) with parallel running software, so the data can be read out pseudo parallel and can be stored to disk or passed on to the next instances. The residual dead time consists of the time between generating a trigger signal and registration by the readout program and the time for the sequential readout of the modules.

2.9. The combined DAQ System, Triggers

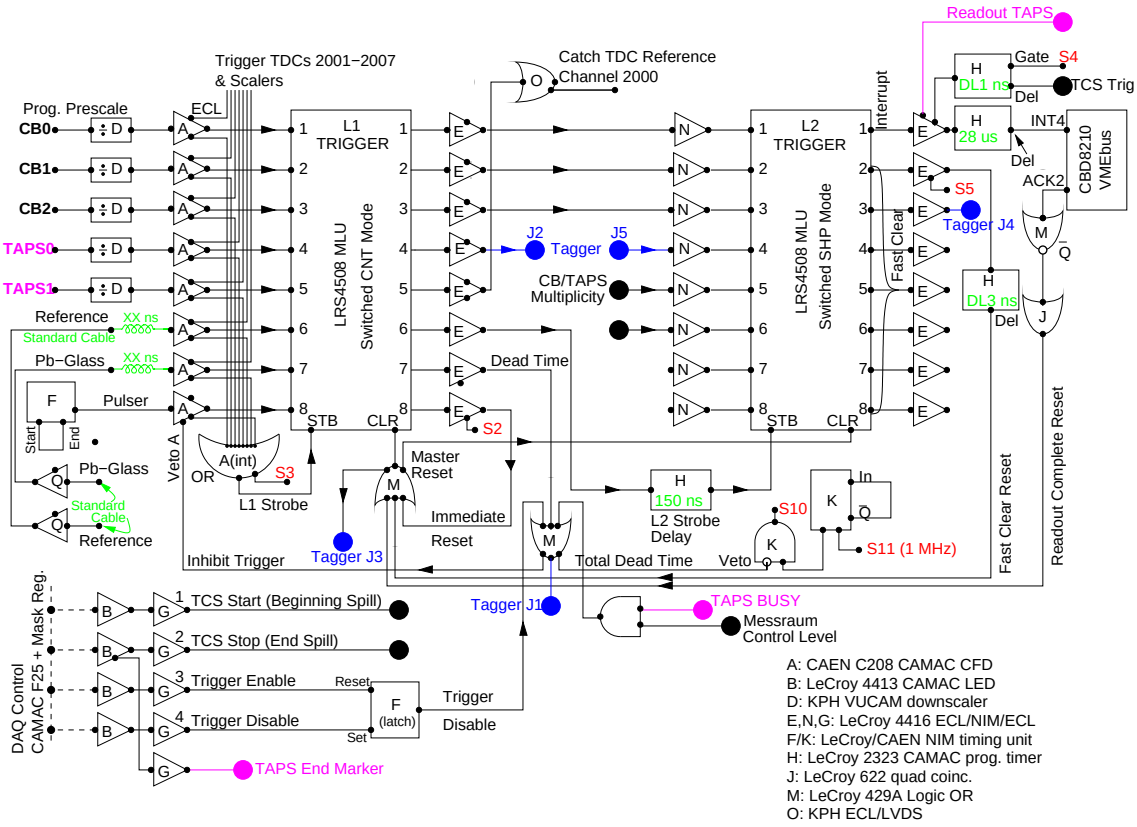

Figure 44: Trigger logic of the CB-TAPS acquisition.

As the reaction between beam and target is a statistical process depending on the cross sections of all allowed reactions, it is not possible to select just the one single reaction at interest. Furthermore, it is not possible to record all events, that are registered in the

detector system because of the high rates. For this reason a trigger system is needed that discriminates non interesting from interesting events which then are read out and taken to disk.
Besides a good signal/noise ratio, the trigger system should also provide a sufficiently high trigger rate to be able to run the experiment with an acceptable statistical error within an adequate amount of time. To be able to calculate absolute cross sections, the trigger has to be simulatable using MonteCarlo with the code GEANT, see chapter 5.

For the CB/TAPS@MAMI experiment a trigger system in two instances was set up. A pattern that is generated within some 10 ns in the first level, then, after around 150 ns it has to be confirmed in the second level. For data taking two possible trigger settings were installed: an energy sum in 1^{st} level trigger and a cluster multiplicity trigger in 2^{nd} level.

The energy sum trigger gives an analog signal of all NaI crystals that pass over a selected threshold. The TAPS modules were not designed to give out energy sums, therefore this trigger only works with the CB. The energy is summed in three steps which is described in detail in [Unv04]. For the rare η-decay runs, the energy sum was set to 300MeV, for the other runs it was set to 40 to 80 MeV depending on the particular reaction.

The cluster multiplicity trigger takes into account the number of final state particles. The reactions

$$\gamma A \rightarrow \pi^0\pi^0 X \quad \gamma A \rightarrow \pi^0\pi^\pm X \tag{37}$$

have at least four particles in the final state. The probability that low energetic nuclei do not reach a detector is very high because they get stuck in insensitive volumes. Thus the multiplicity threshold was set to three instead of four.
The trigger logic shown in figure 44 determines the number of responding discriminators. The area of the CB that is covered by the 16 channels of one discriminator defines the cluster size. If a particle showers into two clusters, it will be counted as two particles, whereas if two particles are hitting the same area, they will be counted as one particle. To determine the right number of clusters, the cluster size and the number of "logical areas" have to be considered independently. The OR signals of the 16 crystals of a discriminator B are translated into NIM signals. Those are collected by four LeCroy 4413 discriminators D. On the backplane a current of 1 mA per responding channel is provided. The discriminators E behind the linear FIFO have to have values between 100. . .150 mV for multiplicity ≥ 3. Module H delays the signal for the 2nd level trigger. The VUCAM module G allows to scale down the number of accepted triggers by software. The eight blocks of TAPS are combined to four logic segments that contribute to the multiplicity. To have sufficient events of a known reaction for calibration purposes, a multiplicity M = 2 scaled down by a factor of 50, was added to measure the single π^0 channel.

The main tasks of the event latch (see figure 44) are to recognize the pattern on L1, generate the necessary signals for the readout process, to detect a confirmation on L2 and, if

the event is valid, initialize the readout. The registers L1 and L2 are programmable memories. For each incoming pattern, an outgoing pattern can be stored. Via a programmable downscaler (D) the first level trigger can be weighted relatively. In the discriminator undesirable trigger signals can be switched off. The OR of the valid triggers activates the pattern recognition on L1. For valid L1 triggers, output 7 is closed, an invalid pattern resets the system.
A and L1 form the event flip-flop. In addition, L1 stops the tagger TDC's, provides the time difference for the CB and initializes in combination with L2 the pattern recognition. Via the three lowest bits L1 is integrated into L2 and then a final decision is made whether to reject the event or not. If the event is kept, the FIADC gates, the TCS trigger is generated and CB and TAPS are read out. The LATCH is cleared when the CB- and TAPS-readout is finished. Both systems send their data packages to the global event builder that combines the streams before writing them to disk. The synchronisation between CB and TAPS is monitored in several stages.

- The TAPS acquisition sends an event number to the CB readout. On merging the streams, this number is compared.
- Both systems record time references derived from the TAPS pedestal pulse trigger. If both systems are running asynchronously, the fixed time relation vanishes and the systems get "out of sync". A restart has to be done.
- Combining single π^0 events from one photon in CB and one in TAPS, a peak at the original π^0 mass has to be visible. In the "out of sync" case, only the combinatorial background will increase.

2.10. Overview of taken Data

During the beam time periode from June 2004 to April 2005 a great amount of data using different targets, like Hydrogen, Deuterium, Lithium, Carbon, Calcium and Lead were taken. Different maximum beam energies like 450 MeV, 645 MeV and 883 MeV were chosen to study for example pion production at threshold, the magnetic moment of the Δ resonance, η and rare η production and medium effects. Polarized beam and polarized targets were used for investigating asymmetries, in order to perform a full set of experiments. All beamtimes used for studying medium effects are listed in table 11. In the field "conditions", the detector systems being read out are listed. "TAPS" means that all BaF_2 crystals of TAPS were red out, "TAPS 1 off" means that for the inner ring of TAPS the HV was switched off and for "TAPS 2 off" the inner two rings were switched off.

	^{2}H	^{7}Li	^{nat}C	^{nat}Ca	$^{208}Pb(I)$	$^{208}Pb(II)$
Date	26.10.- 03.11.04	17.03.- 28.03.05	30.03.- 01.04.05	28.03.- 30.03.05	17.02.- 07.03.05	01.04.- 04.04.05
Time [h]	110	243	32	58	313	58
Files [GB]	315	680	99	160	264	169
File-Nr	4117-4336	6077-6501	6604-6669	6504-6602	5789-6064	6671-6775
Trigger	$M \geq 2$	$M > 2$	$M \geq 2$	$M \geq 2$	$M = 2(1/50) \wedge M > 2$	$M \geq 2$
$\Sigma_E(CB)$ [MeV]	40	50	50	50	50	50
Beam Current [nA]	3	6	3,5	5	12	7,5
E_γ [MeV]	883,24	883,24	883,24	883,24	645,27	883,24
Readout rate [Hz]	1200	1400	1200	1100	280	950
TAPS LED OR rate [kHz]	7.8	12	54	127	126	133
TAPS CFD OR rate [kHz]	29.5	651	596	690	690	662
Tagger Elements	1-320	1-320	1-320	1-320	1-284	1-320
Tagger OR 16 / 10 [kHz]	272	376	241	310	564	432
Collimator [mm]	3	4	4	4	3	4
Radiator	Diamond	10 μm Fe	10 μm Fe	10 μm Fe	10 μm Fe	10 μm Fe
Conditions	CB, PID MWPC TAGGER TAPS	CB, PID MWPC TAGGER TAPS 2 off	CB, PID MWPC TAGGER TAPS	CB, PID MWPC TAGGER TAPS 1 off	CB, PID MWPC TAGGER TAPS 2 off	CB, PID MWPC TAGGER TAPS 1 off

Table 11: Overview of “medium effects” beamtimes.

3. Calibration and Reconstruction

After having taken the data, it is necessary to calibrate all detector systems. This means that a conversion of the integer channel values (coming from the ADC's) to continuous meaningful quantities - like time or energy in physical units - has to be done.

3.1. TAPS

The TAPS system has to be calibrated before it can be used to determine the energy of the detected reaction products of nuclear reactions which is essential to do the tagger random subtraction. Therefore, several calibrations must be done. These are described in this section.

3.1.1. Energy-calibration

To convert the QDC channel information into energy information, it is necessary to perform a calibration. Due to the fact that the used setup (BaF_2 crystal, photomultiplier and readout electronics) has a linear dependency between the deposited energy and the pulse-height being analyzed in the NTEC board, it is sufficient to determine two calibration points. These points should be easy to determine and should be unique (to prevent mis-calibrations).
Figure 45 shows an energy spectrum of minimal ionizing cosmic muons that interact with the detector material. Those demanded points can be taken from this picture. The first point is the pedestal, the origin of this is explained in section 2.7.3. For the second point one can use the peak which shows the average energy deposition by cosmic muons (minimal ionizing particles) passing through the scintillator material. The energy value for BaF_2 crystals lying horizontally on a flat side was determined to 37.7 MeV [Röb91]. This value is used for an alignment of all detectors and as a pre calibration.
The calibration measurements were completed before and after every beam-period. This was important in order to have redundant energy calibration information available and to monitor the time-stability of all calibrations.
A second element to monitor the energy calibration is the pedestal pulser. This pulser does the following:
When no signal from any crystal has to be processed, a digital test-pulser fires just the digital part of the readout-electronics. As there is no energy information from the analog input, the time and energy value 0 is read out. The channel with E=0 MeV is producing a peak. With this technique one can easily check the position of this pedestal (which are set in the interval channels $95 \ldots 105$). Using the relation 38, the energy calibration was performed.

$$Energy\,[MeV] = \frac{Energy\,[ch.nr.] - pedestal\,[ch.nr.]}{cosmicpeak\,[ch.nr.] - pedestal\,[ch.nr.]} \cdot 37.7 MeV \qquad (38)$$

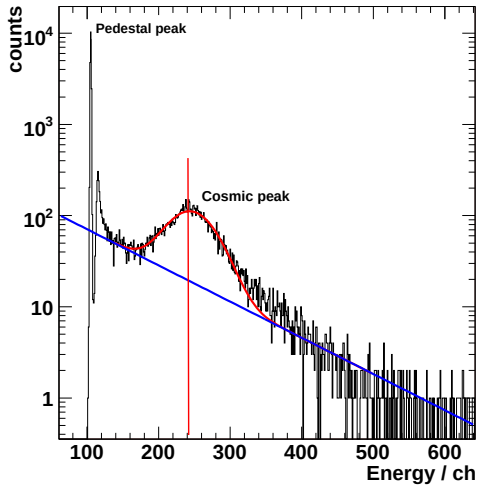

Figure 45: TAPS energy calibration using cosmic muons.

This technique calibrates the BaF_2 detectors relatively to each other. It has to be done for both the slow and the fast component of the scintillation light. The slow component refers to the total energy deposited in the BaF_2 detector (because of better energy resolution than the fast component) whereas the fast component is only needed for the pulse shape calibration which will be described in section 3.1.3.
The final energy calibration is based on this pre calibration. However, the different ionization properties of the particles are taken into account.

Cosmic peak and pedestal position determination:
The determination of the pedestal is taken by the first highest channel before it decreases again. The cosmic ray peak position is determined by fitting a gaussian to the signal plus an exponentially falling background as shown in figure 45 [Boi07].

3.1.2. Time-calibration

TAPS-TDC

The time calibration for TAPS was done in two steps.
First of all, every single TDC spectrum was fitted with a gaussian distribution. Next, the mean position was determined. Finally a linear offset factor to correct the misalignment

was calculated. In this way one is able to do a relative alignment of all detector elements.

TAPS-TAGGER

To perform the tagger random background subtraction or to use time of flight information for the particles, an absolute timing is needed. This was done by using the tagger as reference. All TAPS times were aligned with respect to the tagger channels (which are also relatively aligned, see chapter 3.3.3). For tagger and TAPS the start signal is generated individually and the trigger is used to apply the common stop. With this information, the tagger time has to be subtracted from the TAPS time to get the relative timing between tagger and TAPS.

$$\Delta t = (t_{trigger} - t_{TAPS}) - (t_{trigger} - t_{tagger}) = (t_{tagger} - t_{TAPS}) \tag{39}$$

Thus, the electronic trigger time will be eliminated.
Each tagger element and each TAPS channel have to be calibrated individually. All $352 \otimes 510$ time differences can be computed. This is done by fitting the peaks and calculating offsets. To minimize calculation time, the following calibration procedure was chosen:
First, the time differences of all 510 BaF_2 channels to any arbitrary tagger channel were calculated. Then the spectra were fitted and the time was shifted to align the peaks, which is shown in figure 46 left plot. In the second step, this procedure was done by aligning the tagger channels with respect to any BaF_2 crystal. The whole procedure was repeated until the resolution was optimized. The results are shown in figure 46 right hand side. The resolution obtained with this method is less than 2 ns [Zeh07].

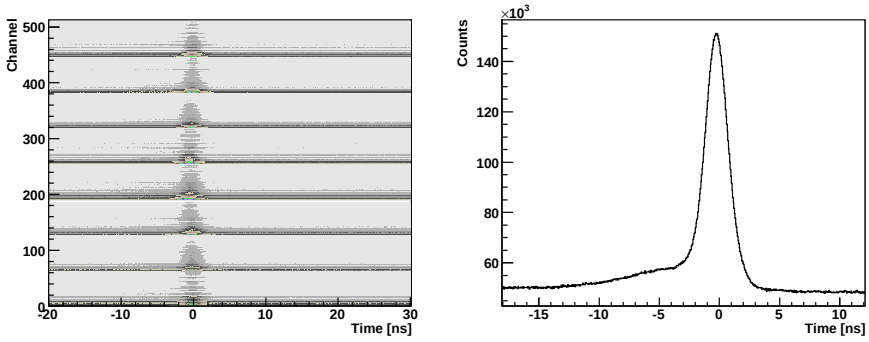

Figure 46: TAPS time calibration.
The left plot shows the relative alignment of all BaF_2 channels against the tagger. In the right plot the overall time spectrum is shown. This figure was provided by [Zeh07].

By plotting the timing of a particle detected in TAPS versus the energy deposited in the crystals, a time of flight analysis becomes possible. Figure 47 shows such a spectrum. Using the specific relation between time-of-flight and energy, particles of different masses can be separated.

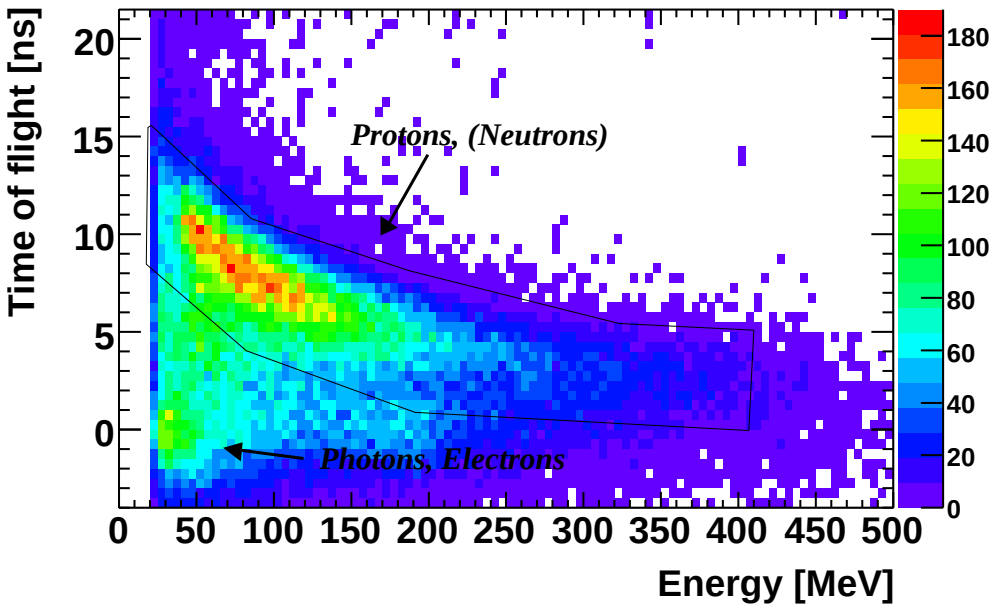

Figure 47: TAPS Time of flight versus energy plot with graphical proton cut.

3.1.3. Pulseseshape-calibration

BaF_2 has two scintillating components. Using the ratio of both one can distinguish photons from hadrons. If a particle is stopped in the crystal, all energy is deposited within a few hundred ps and the scintillation light is emitted within 2 μs for the slow component. For photons, the amount of light that is emitted within the first 30 ns is almost as high as the total light output, whereas this is not the case for protons. So, by integrating the PM signals over a time range of 30 ns and 2.0 μs, respectively, one obtains two values per BaF_2 channel, the so called short and long components. These signals are the same for the short integration window and the total light output in case of a photon (because of a very similar ionization mechanism compared to the cosmic muons, the calibration was done with), but they differ for non minimum ionizing hadrons. In figure 48 left plot, a schematic for this effect is shown. Plotting the energy deposition of the short component (E_S) against the long component (E_L) or the total light output, like it is shown in figure 48 right hand side, one is able to separate different types of particles.
Because the lines, generated by the different particles, have approximately the same origin but different slopes, it is more useful to plot the pulse-shapes in polar coordinates. This type of display has been invented by [Hej98]. Here the distance (or radius) R between any point and the origin is plotted against the angle ϕ to the x-axis.

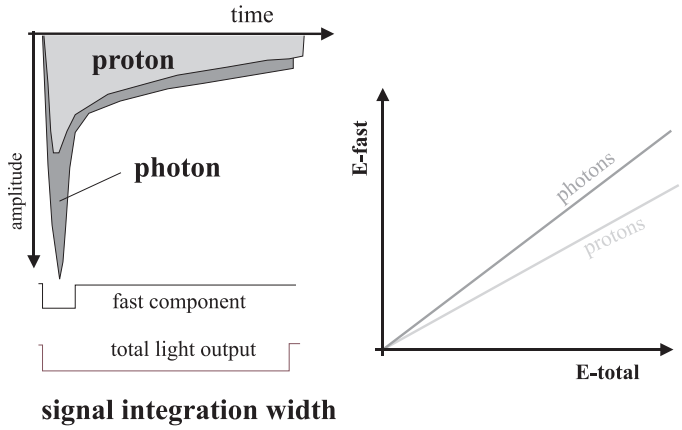

Figure 48: BaF_2 pulse forms for fast and slow component.

$$R = \sqrt{(E_S^2 + E_L^2)} \tag{40}$$

$$\phi = arctan\left(\frac{E_S}{E_L}\right) \cdot \frac{180^\circ}{2\pi} \tag{41}$$

In an ideal calibration the photons should be located at $\phi = 45^\circ$. Due to slight errors in the determination of the energy of the short component (because of its effective integration length of 30 ns), a slight derivation from the ideal pulse-form is visible.
The pulse shape analysis was done in the following way [Kot01]:
The plot on figure 49 right pad shows the polar representation. This plot was sliced up according to radii from $0 \ldots 10 \ldots 20 \ldots 30 \ldots 40 \ldots 60 \ldots 90 \ldots 130 \ldots 200 \ldots 280 \ldots 360 \ldots 420 \ldots 535$ MeV (see the magenta lines, shown on the y axis) and projected to the x axis. The resulting plots (see figure 49 left pad) were fitted the following way. First, a preliminary gaussian was fitted to determine the initial values for the current fit (not shown). Then a horizontal line was applied for baseline corrections (black solid line), afterwards a combined fit of a gaussian (magenta dotted line) on a P0 (not shown) was done. Determining the peak position of the fit (red dotted line) and the standard deviation, a 3σ cut (blue dotted dashed line) was set. The nominal peak position and the 3σ interval are then drawn in figure 49 right pad as the cut line. Every particle lying left to the blue line are hadrons and those on the right hand side (depending on the VETO information) are either photons or electrons.

With that information, an individual cut-line for each detector can be determined. Thereby, photons can be selected or eliminated for the individual analysis. Usually the 3σ-interval (red line) below the peak position (black line) is attributed to photons. In principle, every angle larger than the blue line can be neglected if one is looking for protons. For further analysis only the photons were identified using the 3σ-cut. The proton identification was not done this way.

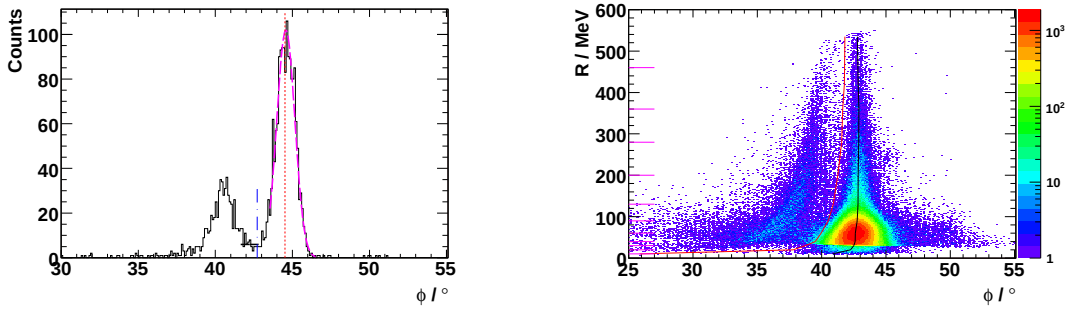

Figure 49: TAPS pulseshape calibration.
The left plot shows the fitting procedure for one radius bin (for details see text). On the right hand side the result of all radii bins is drawn with lines indicating the nominal peak position (black) and the 3σ interval (red). Also shown in magenta is the projection range on the y-axis.

3.1.4. LED-calibration

The energy threshold of the LED discriminators plays a role in the trigger conditions and must be accordingly exactly known and set before starting the measurements. Therefore, a calibration delivering a proper relation between the mV scale of the electronics and the corresponding energy threshold in MeV for the QDC was performed by Benedicite Boillat [Boi07]. This calibration was done by using the comparison between an energy spectrum

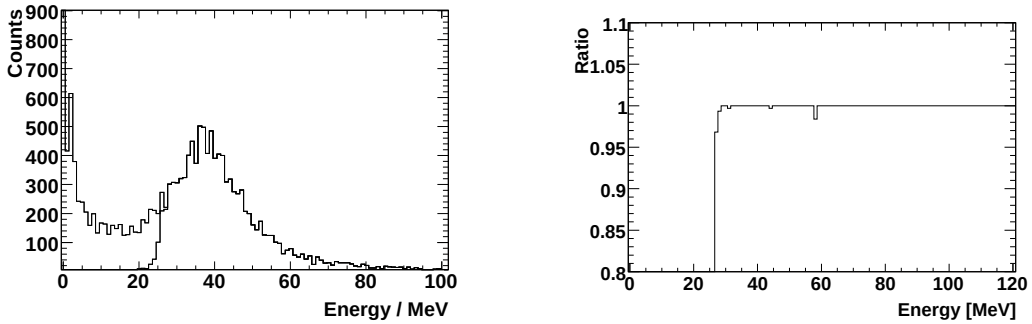

Figure 50: TAPS LED calibration.
On the left side, the cosmic ray energy spectrum is shown with and without an LED threshold. To determine the LED threshold in MeV, the ratio of the two spectra was taken, like it is shown on the right hand side. This figure was provided by [Boi07].

where the LED-threshold was taken into account and one where it was ignored (see figure 50 left) for each QDC channel. The precise determination of the LED threshold was done by generating the ratios of those 2 spectra and requiring a value close to 1 (0.99) (see

figure 50 right). This procedure was repeated for 4 different voltage settings of the LED discriminator (50mV, 100mV, 150 mV, 200mV) in order to get 4 points and thus proceed with a linear fit to finally obtain a reliable conversion function from the threshold in MeV to the hardware setting in mV [Boi07].

3.2. Crystal Ball

3.2.1. Energy-calibration

The calibration for photons was done in two steps. To achieve a rough calibration, the amplification of the PM's were aligned [Unv04]. In the next step, the energy of the π^0 decay photons was multiplied by a detector individual factor, that each $\gamma - \gamma$ mass yield peak at the same π^0 mass. The invariant masses of the photons from the reaction $\gamma p \rightarrow \pi^0 p \rightarrow \gamma\gamma p$ were aligned to $m_{\pi^0} \approx 135 MeV$ [Bru07]. As the electromagnetic shower spreads over several crystals, the energy calibration depends on the method and in which the crystals are combined to form clusters. This will be described in section 3.6.1. This technique is not very successful for protons and charged pions because of the different cluster sizes and problems in the cluster algorithm (to combine the correct cluster sizes) - see figure 51. Moreover it is not needed for the analysis described in section 4, these calibrations will therefore be skipped.

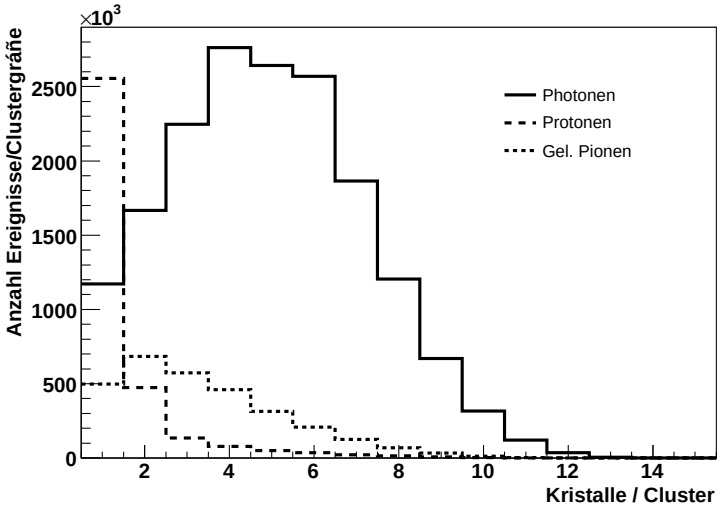

Figure 51: Crystal hits per cluster for different particles in CB.
This figure was taken from [Kra07].

3.2.2. Time-calibration

The Crystal Ball time calibration is similar to the time calibration of TAPS. The major difference is the way the time information of CB and tagger are combined. As the CB readout is started by the trigger signal and stopped by the individual NaI element (common start mode), the determination of the time difference is the following:

$$\Delta t = (t_{trigger} + t_{CB}) - (t_{trigger} - t_{tagger}) = (t_{tagger} + t_{CB}) \tag{42}$$

The time correction consists here of a relative alignment of the ladder times (due to different paths of the electrons in the tagger and cable length) and a relative alignment of the detector times, like it was done for TAPS. But in addition, since the CB time depends on the energy of the detected particle, a walk correction had to be applied to compensate for the pulse-height dependence of the timing. This correction can be performed by plotting the energy versus the time of the photons stemming from the reaction $\gamma p \rightarrow \pi^0 p$, as it is shown in figure 52. This spectrum was cut into slices, the peak position was fitted and the offset was calculated from the CB- and tagger time. For the Crystal Ball a resolution of 4 ns can be achieved [Zeh07]. This calibration was not provided from the CB analysis experts resulting in multiple redundant work of the individual PhD students as well as a relatively bad time resolution.

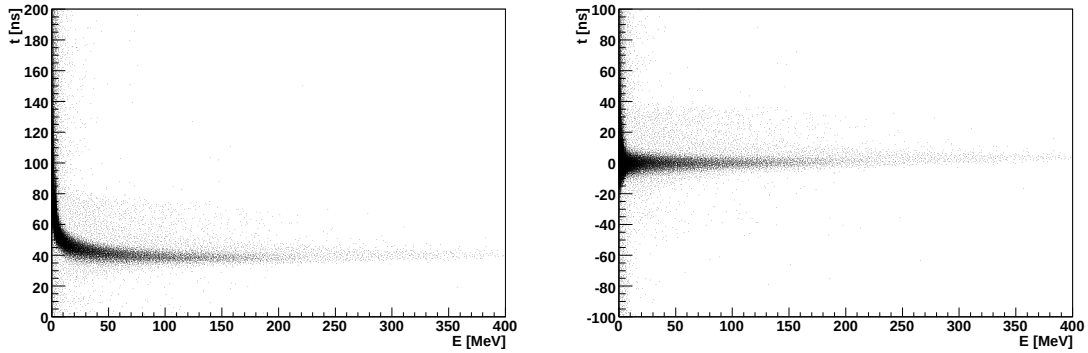

Time versus energy plot before correction. Time versus energy plot after correction.

Figure 52: NaI walk correction.
The picture was taken from [Kra07].

3.3. TAGGER

3.3.1. Random substraction

Due to the high electron flux coming from MAMI, there is always more than one electron hitting the tagger per hadronic event. To distinguish between prompt photons that induces

the real events and random background, the following steps were performed. Looking at the OR of all tagger times, one sees an almost flat background of random photons and a peak which is related to the experimental trigger and thus with the prompt photons. Assuming the background under the peak to be as flat as the background aside, one can subtract the scaled background (in figure 53 indicated as U_1 and U_2) area from the peak area (C), resulting in the prompt photons (S). The signal can be calculated using equation 43, where ΔC and$\Delta U_1 + \Delta U_2$ denote the width of the coincidence window the background time window respectively.

$$S = C - \frac{\Delta C}{\Delta U_1 + \Delta U_2} \cdot (U_1 + U_2) \tag{43}$$

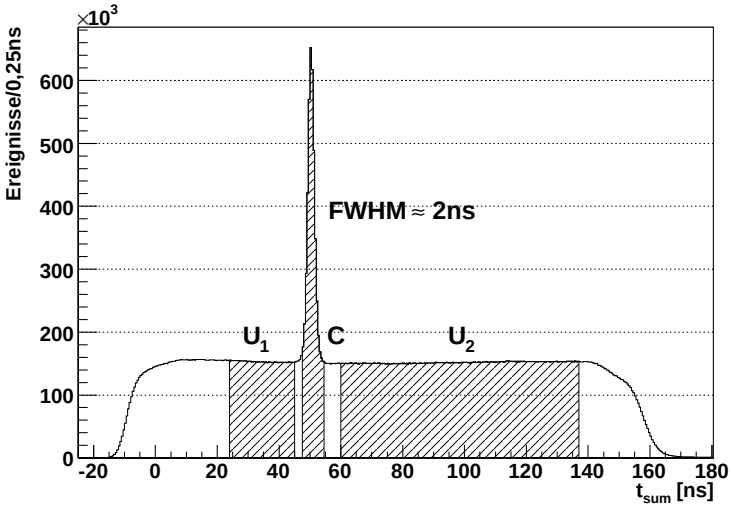

Figure 53: Tagger random background subtraction.
See text for details.

3.3.2. Energy-calibration

The energy calibration of the tagger was done by setting the field of the tagger magnet in a way that the bending curvature radius of the electrons in the corresponding interesting photon energy region is covered by the 352 elements in the focal plane detector. By knowing the fieldmap of the tagger magnet very well and also knowing the energy of the electrons provided by MAMI, the scattered electron energies can be calculated easily. The online tagger energy calculation program [TAGG] translates the tagger element number into the energies of the scattered electrons and the incident photon energy.

3.3.3. Time-calibration

The time calibration is done by fitting the peak in every TDC spectrum with a gaussian, determining the mean position, and finally calculating an offset factor to correct the misalignment [Cod07]. With this method an over all time resolution CB vs. Tagger of 2 ns is achievable. Figure 54 shows the online Tagger TDC spectrum which is already roughly aligned.

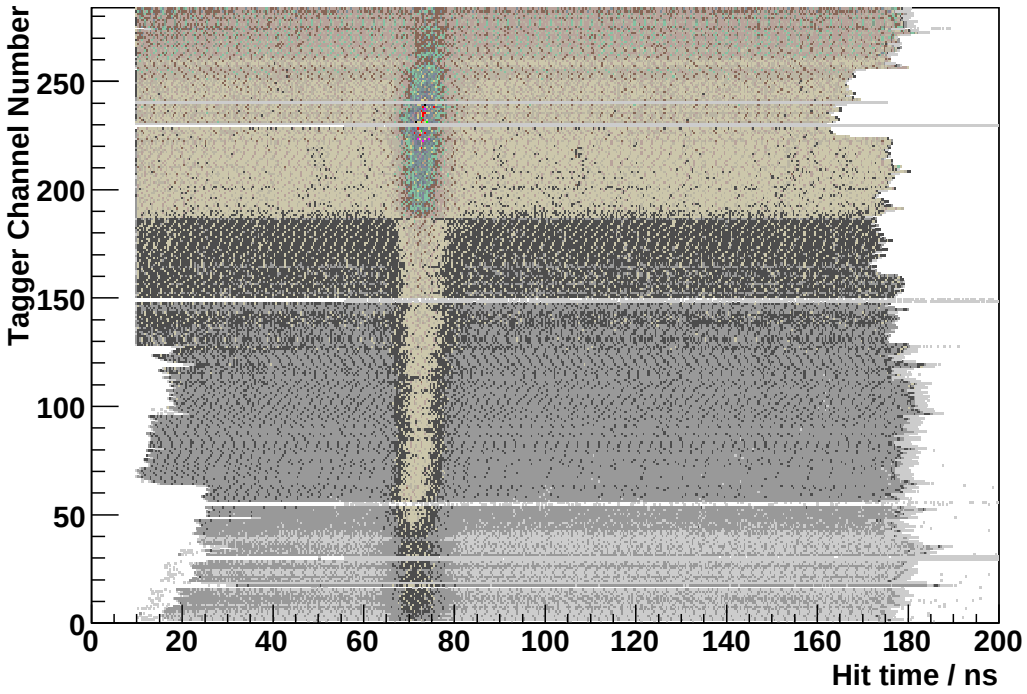

Figure 54: Time aligned Tagger TDC spectrum.

3.3.4. Tagging Efficiency (TE) Calibration

The number of photons produced in the radiator can be determined by summing up the scaler events for all tagger elements. Because the tagged photon beam is collimated, not all produced photons will reach the target. The tagging efficiency, (besides the collimator diameter), depends on the incident beam energy and the alignment of the beam along the collimator axis. To measure the tagging efficiency a Pb-glass detector was used which has 100% efficiency for photons and is mounted on the downstream side of the target. A low beam current is used to prevent random coincidences. Electrons hit the radiator and produce a bremsstrahlungsphoton as described in section 2.3. The electron which produced this photon hits tagger element i. In this element it starts a counting clock in the $TDC[i]$. The stop signal for all TDC's is generated by the experimental trigger; In the

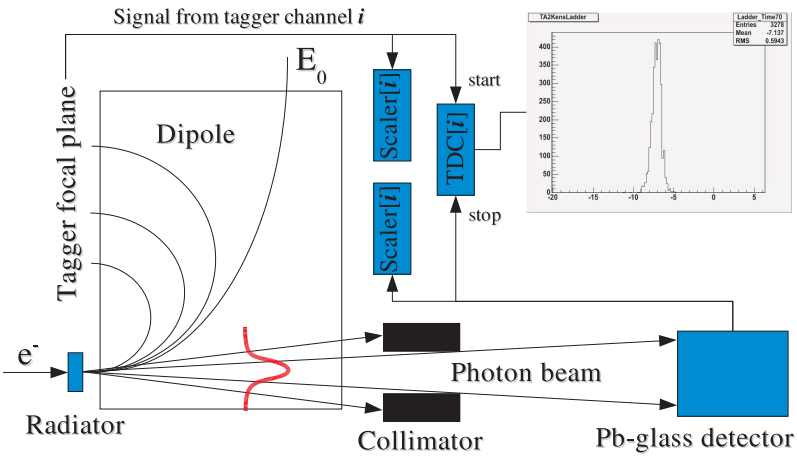

Figure 55: Schematics of a tagging efficiency measurement.

case of tagging efficiency measurement, the stop signal is generated by the Pb-glass detector being fired by the produced bremsstrahlungs photon. Every tagged electron hitting the focal plane detector that comes in coincidence with a photon is stored to $Ladder\_Hits[i]$ and $Sum\_Scalers[i]$. Those who are not correlated with a photon are just written to $Sum\_Scalers[i]$. A schematic overview is drawn in figure 55
The tagging efficiency is then determined in the following way, derived from equation 44:

$$\epsilon_{tagg}[i] = \frac{Ladder\_Hits[i]}{Sum\_Scalers[i]} \tag{44}$$

For the lD_2 runs with a 3 mm collimator the tagging efficiency was determined by Alexander Nikolaev to 32% in the energy range of $400 \ldots 460$ MeV, see figure 56. Details on the tagging efficiency calibration can be found in [Nik06].

3.4. Multi Wire Proportional Chamber

The angular resolution was determined by measuring cosmic rays going through the detector. The information of the 4 interaction points (strips and wires) of the two chambers can be combined to one track from each chamber. As the muons travel on straight lines through the material, both tracks have to be collinear. The angular resolution was determined by comparing the θ and ϕ angle difference between the two tracks to $\Delta\theta \approx 1.88°$ and $\Delta\phi \approx 1.33°$ [Dow03].
The efficiency of the chamber was determined by comparing events having two interaction points in both chambers with those having one interaction point in either one chamber to 81.2%.
The proton detection efficiency was determined by the reaction $\gamma p \rightarrow \pi^0 p$, taking three cluster events. The direction of the proton was predicted by applying coplanarity between the reconstructed π^0 and the proton and then identified via the PID $\Delta E/E$. An additional condition was and a cut on the invariant mass of the π^0 of 135 MeV. This results in a

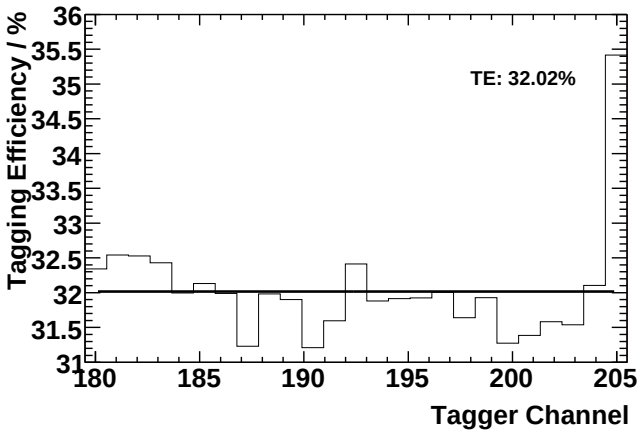

Figure 56: Tagging Efficiency in the interesting energy regime.
Also plotted is the result from fitting a horizontal straight line to the data.

proton track efficiency of 89,7%. Analogous to the proton efficiency, the efficiency for charged pions was determined with the reaction $\gamma p \rightarrow \pi^+ n$ to 79.3%. Here two clusters were required with one PID hit indicating the $\pi^{\pm}$. An additional cut on the polar angle of the neutron to be smaller than 60° was used. The difference in the efficiency for charged pions and protons is due to the higher proton ionization resulting in a larger output signal [Sch07].

3.5. Particle Identification Detector

All PID calibration procedures were designed and performed by Evie Downie and Richard Codling, Glasgow [Dow06].

3.5.1. Position-calibration

In the position calibration, the azimuthal angle of the PID elements relative to the Crystal Ball was determined. Plotting the PID element number versus the ϕ angle of the CB clusters for events with only one CB cluster and one PID hit, the position of every single element can be determined. To get more reliable results, for every element projections of this plot were performed and a gaussian around the highest point in this spectrum was fitted. From this, the mean ϕ position of each individual element was calculated and is shown in figure 57

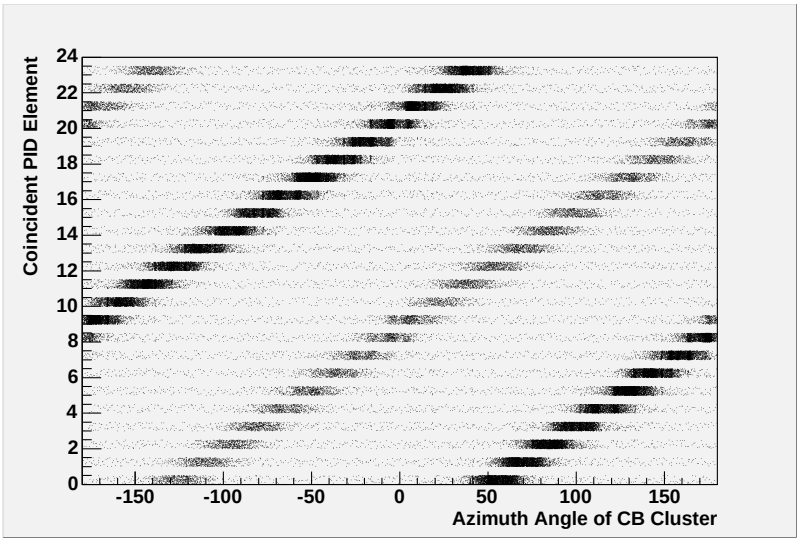

Figure 57: Azimuthal angles of CB clusters in coincidence with PID elements.

3.5.2. Energy-calibration

The PID was designed to separate electrons, charged pions and protons by determining the energy deposited in the plastic. By plotting the deposited energy in the PID (ΔE) versus the energy stored in the CB and then projecting it to the ΔE axis in an energy range of $32 \ldots 48$ MeV, one ΔE peak at 0.4 MeV (for charged pions) and another at 2.3 MeV (for protons) is visible for simulated data. The energy calibration factor was calculated by aligning the 24 PID elements such that the peak distances between pions and protons was shifted to 1.92 MeV, see figure 58.

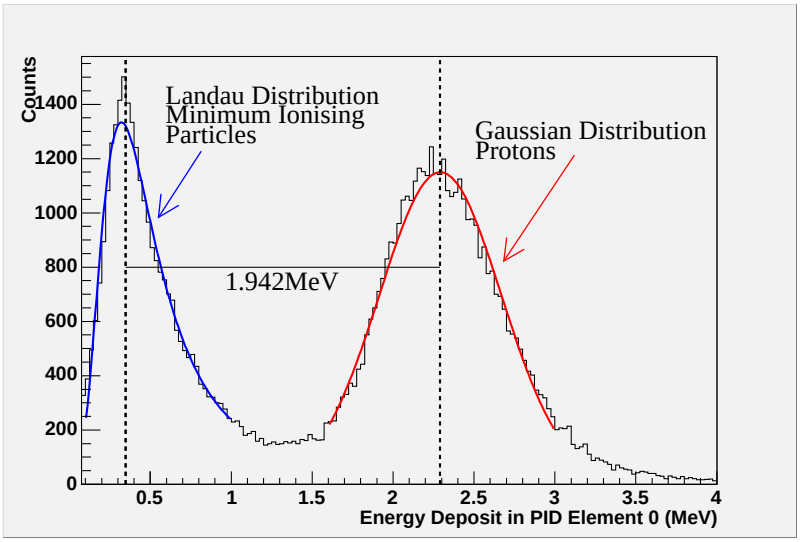

Figure 58: $\Delta E/E$ plot projection with fits to determine the peak positions.

3.5.3. Time-calibration

Using the CATCH TDC's with a fixed time to channel constant with identical readout electronics for all channels, the timing of the PID was aligned by software routines. The pulse form from the plastic is very sharp and gives a timing resolution of 3 ns FWHM. The alignment in time of the detector signals was performed by fitting a gaussian distribution to the time spectrum of every single element and shifting it with an offset function to the desired location in time.

3.6. Reconstruction

3.6.1. Cluster reconstruction

The particles produced by the reactions have different energies and penetrate the detector crystals in different ways. Charged particles ionize directly while neutral particles ionize indirectly, resulting in an electromagnetic shower. This shower does not stop within the dimensions of one crystal. Depending on the Moliere radius of the detector material, a cluster of crystals will take over parts of the particles' energy. A cluster encompasses all crystals which contain parts of this shower.

CB - Cluster algorithm

The cluster algorithm combines neighboring crystals which had correct energy information, in the way that they are grouped to a particle candidate. The main goal is to make clusters small enough that no additional particles are added by accident and at the same time large enough so that all energy of the particle is stored in that cluster. Having the cluster size too large will result in loosing particles and a wrong number of clusters. On the other hand, if the cluster size is too small, a part of the particle's energy will be lost and, in the worst case a second artificial cluster will be created. Unfortunately the CB cluster algorithm does not allow for a consistent treatment of this aspect since no shower shape analysis or local maximum search is possible. In this work, the simple cluster algorithm was used. The crystal with the highest energy deposition is selected, and the energy deposition of the neighboring crystals (in maximum 12 crystals) is added. The cluster position is determined by the energy weighted center of the crystal positions. The time information is extracted from the center detector. This procedure is repeated for all remaining detectors that gave a signal. All clusters with energies below 20 MeV will be rejected for the following analysis. Figure 51 shows the number of NaI crystals in the CB being hit for the different particle groups [Kra07].

TAPS - Cluster algorithm

Depending on the type and energy of the particle, different cluster sizes can be observed

in TAPS. If, for example, the energy is very high, or the particle is hitting the detector close to the edge of a crystal, the shower will spread over several crystals. For charged pions depositing their energy in TAPS, the whole energy is deposited within 3 detectors. To determine the energy of the particle, it is not sufficient to read out the crystal firing the LED. All energies of the surrounding crystals must be summed up to get the particle energy.
Problems can occur when two showers are close, however it is not easy to determine a border line between them.
The summation is also handled by the cluster algorithm. In the first step, the central detector of a shower is determined by searching for a maximum in the energy deposition. Starting from this center crystal, the neighboring crystals are considered. If they contain energy, it is summed up and the next neighbors are treated in the same way. To discriminate two neighboring hits with overlapping shower areas, the algorithm has to contain an escape sequence. This sequence monitors the decreasing energy deposition and delayed timing information starting from the center. For TAPS the shower spreads in maximum over two rings, surrounding the center crystal, an additional escape sequence was implemented. This sequence stops automatically after having summed the energy over these two rings.

3.6.2. Impact reconstruction

The impact point of a particle in TAPS is reconstructed by determining the centroid of the shower generated by the particle. The midpoints of the crystal's surface are weighted using the logarithm of the energy deposited in the crystal.

$$W_i = max\left\{0, P + log\frac{E_i}{E}\right\} \tag{45}$$

$$x = \sum \frac{W_i \cdot x_i}{W} \tag{46}$$

$$y = \sum \frac{W_i \cdot y_i}{W} \tag{47}$$

The construction of W_i in this way allows very small energy depositions contributing to the impact point. An optimal value for P was determined to be 5 [Mol92].
This correction is valid for any particle hitting TAPS orthogonally. Depending on the geometrical setup, this assumption is in first approximation valid for crystals in the inner rings. For this reason, the impact point also has to be corrected for the penetration depth of the shower.
The shower depth can be calculated from the following formula [PDG04]:

$$d = \left(log\frac{E}{12,7MeV} + 1,2\right) \cdot X_0 \tag{48}$$

with X_0 = 2.05 cm. Using these values and those specified in figure 59, an approximation of the correction can be calculated [Hej98]:

$$\frac{\Delta x}{x} = \frac{\Delta y}{y} = \left(\frac{s}{d} + 1\right)^{-1} \tag{49}$$

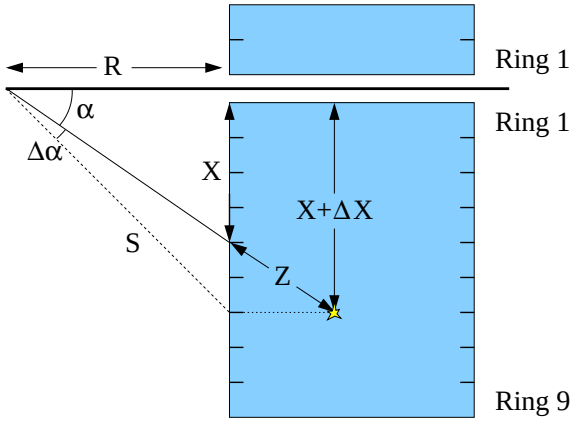

Figure 59: Impact reconstruction.
See text for details.

3.6.3. Particle reconstruction

Combining the information of all detector elements per detector class, one is able to separate protons, neutrons, charged pions, electrons and photons.
In TAPS the particle identification was done by combining the information of VETO, PSA and TOF. In table 12 an overview is given.

TOF	PSA	VETO	Particle
$\in$ photon cut	$\in$ photon band	fired	electron
$\in$ photon cut	$\in$ photon band	not fired	photon
$\in$ proton cut	$\notin$ photon band	fired	proton
$\in$ proton cut	$\notin$ photon band	not fired	neutron
$\in$ pion cut	$\in$ any band	fired	pion
$\in$ pion cut	$\in$ any band	not fired	neutron
$\in$ no cut	$\notin$ photon band	fired	electron
$\in$ no cut	$\in$ any band	not fired	none

Table 12: TAPS Particle Identification.
$\in$ = inside element
$\notin$ = not inside element

In the CB, the particle identification was also implemented using graphical cuts. Analog to the TOF analysis in TAPS, the energy loss in the PID was plotted against the deposited

energy in the NaI crystals. Applying cuts for every single PID element for protons and pions, a separation of protons, pions and from photons was done. Figure 60 shows the cuts for pions (lower cut window) and protons (higher cut window). Also seen are the low energetic electrons close to threshold.

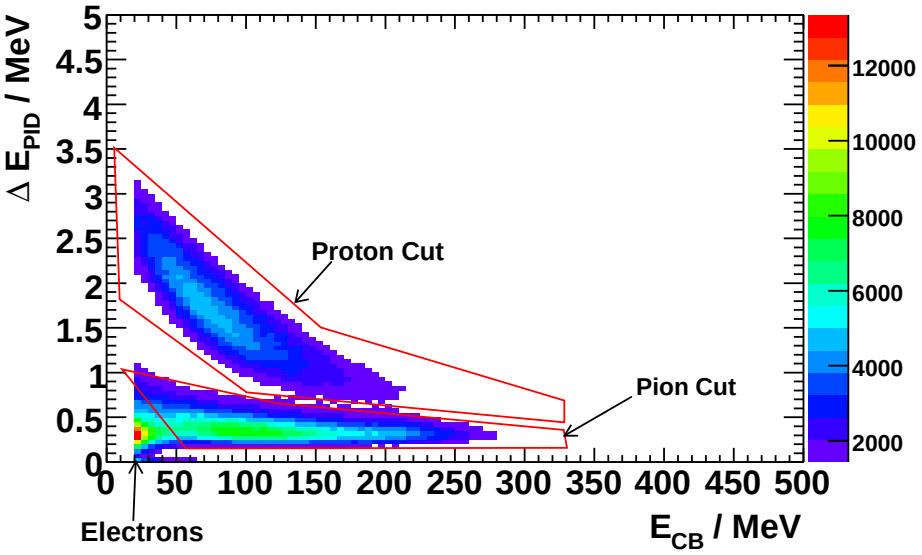

Figure 60: Particle identification using the experimental $\Delta E/E$ information.

For the CB the information from the graphical $\Delta E/E$ cuts were used for particle discrimination like listed in table 13.

PID	Particle
not fired	photon
$\in$ proton cut	proton
$\in$ pion cut	pion
$\in$ no cut	none

Table 13: CB Particle Identification.
$\in$ = inside element
$\notin$ = not inside element

4. Analysis

The analysis looks for events of the desired reaction channel in the raw data. To speed up the analysis, a preselection on the data was done. The analysis-speed of the channel described below was increased by a factor of 5 by selecting events with a multiplicity $M \geq 3$. This is the minimal requirement for the reaction $\gamma A \longrightarrow \pi^{\pm}\pi^0 X$ assuming the decay $\pi^0 \longrightarrow \gamma\gamma$ but without considering the recoil particles. Having reduced the amount of data by applying the preselection on the raw data, events with appropriate parameters were then filtered out by performing cuts on the particles' attributes. Using information about e.g. charge, timing, mass, angles, the reaction particles can be extracted form the raw data.
For the analysis of the raw data the Acqu-Root analysis framework was used developed by John Annand from the Glasgow University [Ann97] [Ann05] based on the ROOT framework [Bru05]. It consists of Detector- and User classes. The detector classes extract data from the stream, converting bitpattern, ADC and TDC channels into physical units according to the values stored in the calibration files. Afterwards, in the user classes the values can be processed. Here the analysis of the data itself is performed. Event by event, using cuts to eliminate other reactions, the desired channel is selected and the data is stored in root format. Using macros on those root files, the data can be processed and the histograms visualized.

4.1. The $\pi^0\pi^0$ channel on liquid Deuterium

To extract the $\pi^0\pi^0$ channel, the data files were analyzed under the following conditions:

Tagger random background substraction

Like described in 3.3.1, the background was subtracted by determining an area beside the peak and the area under the peak of the time coincidence spectrum. The scaled non-peak area was subtracted from the peak area to get only real events.

Number of Clusters

For a valid event, 4 photons have to be identified. As neutrons can be misidentified as photons, also 5 photon events were allowed. The photons were grouped into two π^0 particles using combinatorics under a "best pion condition". The best pion condition was determined by equation 50:

$$\xi^2 = \left(m_{\gamma_1\gamma_2} - m_{\pi^0}\right)^2 + \left(m_{\gamma_1\gamma_2} - m_{\pi^0}\right)^2 \tag{50}$$

The photon combination with the lowest ξ^2 was taken as the two pions for the current analysis.

Cut on the incident photon energy

To reduce the distributions of the4-momenta due to fsi, the incident photon energies were limited to 400-460 MeV leading to pions with relatively large mean free paths (near $p_\pi \approx 150$ MeV/c), see figure 14.

Opening angle cut

To suppress so called split-offs, a minimal opening angle of 30° for the photons from the π^0 decay was required.

Missing mass analysis

To ensure the reaction was taking place on one single nucleon and that no energy was transfered to the rest of the nucleus, the missing mass is determined with equation 51, where P denotes four momentum vectors.

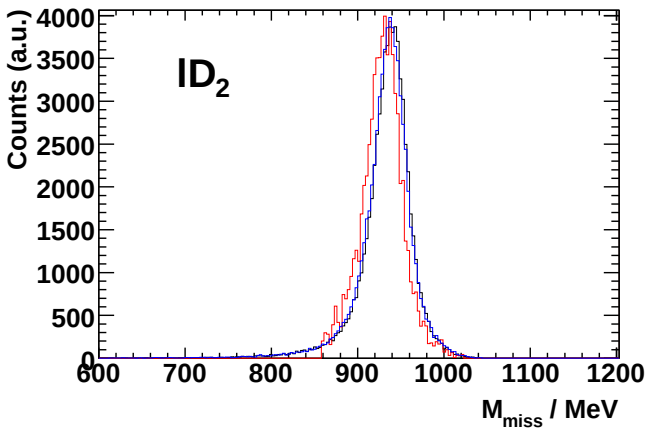

Figure 61: Missing mass of the nucleon in the $\pi^0\pi^0$ channel.
The black histograms is the missing mass spectrum from simulation for the channel $\gamma n \rightarrow \pi^0\pi^0 n$, the blue one for $\gamma p \rightarrow \pi^0\pi^0 p$. The red curve shows the missing mass distribution from the analysis of experimental data in the neutral channel.

$$M_{miss} = \sqrt{P_\gamma + P_{nucleon} - P_{\pi_1^0} - P_{\pi_1^0}} \tag{51}$$

Plotting the missing mass as shown in figure 61 red line, there is a peak at the mass of a nucleon. Therefore the reaction always took place on a single nucleon for the selected events. To reduce the background, a missing mass cut $M_{miss} \geq 860$ MeV was applied. The peak width is dependant on the detector resolution and the Fermi momenta. For comparison, the missing mass calculated from simulation of neutron and proton (black

and blue) is also plotted. For technical reasons, the cut on the missing mass is not shown for the simulated data. A comparison of the missing mass for the simulated data with and without Fermi momenta will be given in section 5.1.

Pion mass cut

The mass of the two pions is plotted in a symmetrized 2D diagram. Figure 62 shows an enhancement of the correlated $\pi\pi$ pairs at the nominal mass. Because of the combinatorial background, a relative broad cut (80 - 180 MeV) was chosen to be able to extrapolate the background with a fit function in the next steps.

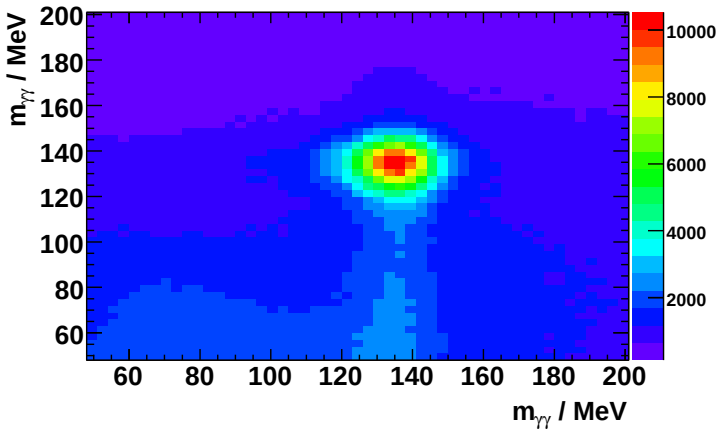

Figure 62: $\pi^0\pi^0$ mass distributions for incident photon energies from 400 to 460 MeV.

Cut on the $\pi\pi$-mass bins

The invariant mass of the $\pi\pi$ system was calculated from the reconstructed pions. Because of the wide cut, applied in the last step, a large amount of background remained. The invariant mass of the $\pi\pi$ system was plotted against the invariant mass of one π^0 like it is shown in figure 63. This spectrum was sliced into 5 MeV wide bins from $m_{\pi\pi} = 270 \ldots 390$ MeV. For each $\pi\pi$-mass bin the mass distribution of the π^0 was plotted in a histogram as shown in figure 64.

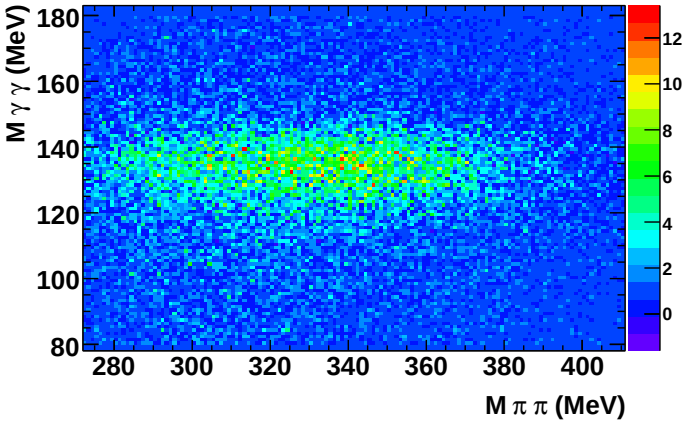

Figure 63: $m_{\gamma\gamma}$ versus $m_{\pi\pi}$ of one π^0 in the neutral channel for 400-460 MeV incident photon energy.

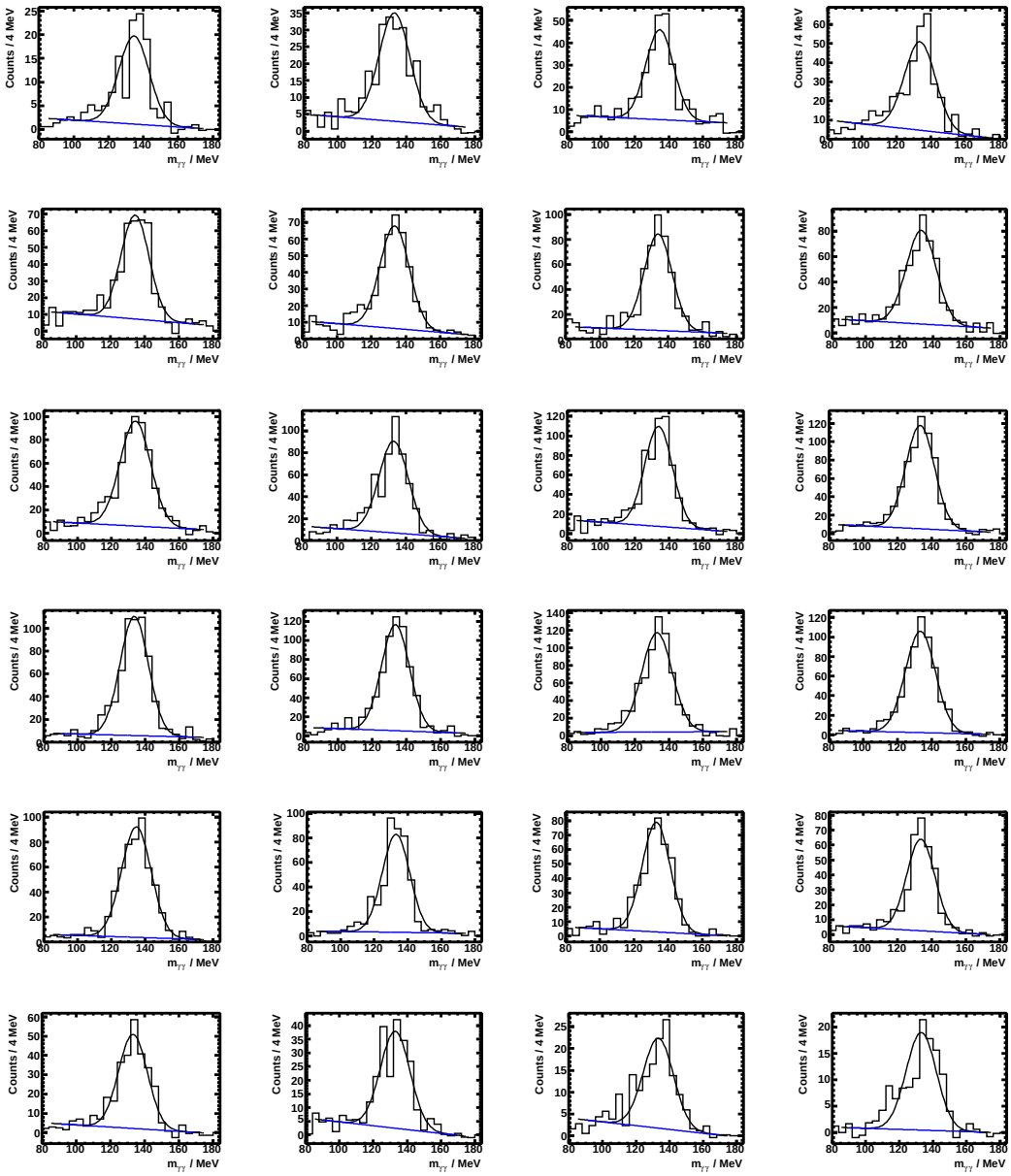

Figure 64: $m_{\gamma\gamma}$ spectra for the 5 MeV wide mass bins in the mass range from 275 MeV to 395 MeV in the $\pi^0\pi^0$ channel for 400-460 MeV incident photon energy. Fitted was a gaussian plus linear background in the range of 85-175 MeV, the width was allowed to vary between 8.2 and 9.0 MeV, the peak position between 133 and 137 MeV.

The background was fitted linearly and superimposed by a gaussian distribution in the peak area. In this way, the mass distribution of the pion pairs was determined much more precisely than just by taking a narrow $\pi\pi$-mass cut. The $\pi\pi$ invariant mass distribution after background subtraction is shown in figure 65.

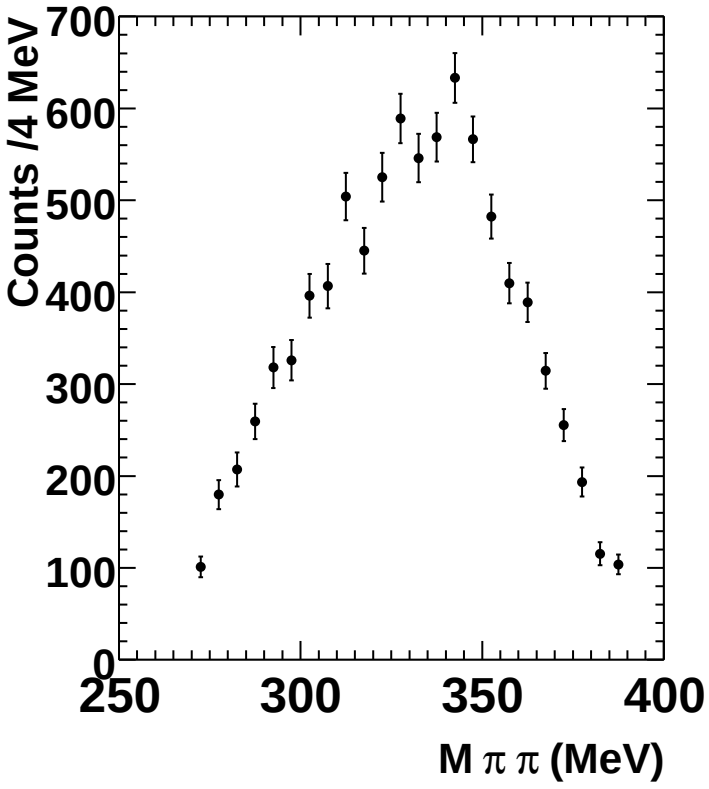

Figure 65: Mass distribution in the $\pi^0\pi^0$ channel for 400-460 MeV incident photon energy.

Figure 66 shows the angular distributions of the pions on the left hand side and on the right hand side, the angular distribution of the $\pi\pi$ system is plotted.

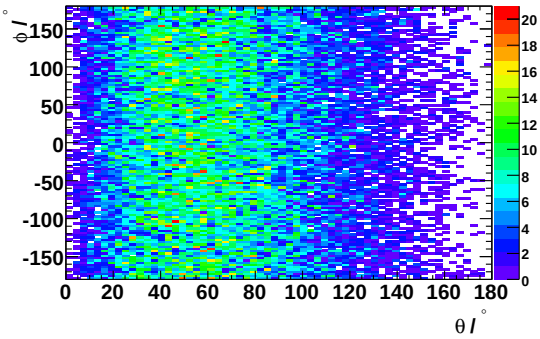

Angular distribution of the single pions.

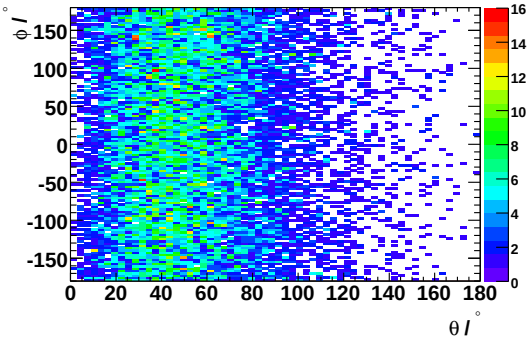

Angular distribution of the $\pi\pi$ system.

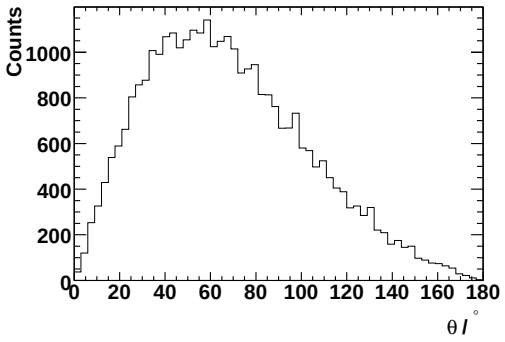

θ-angle distribution of the single pions.

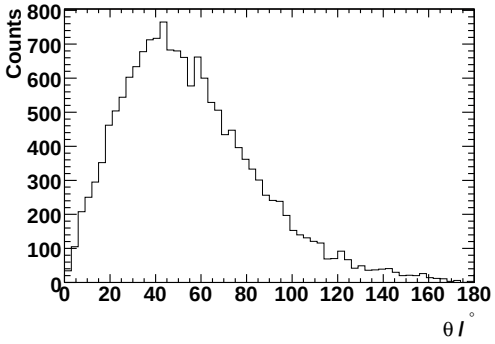

θ-angle distribution of the $\pi\pi$ system.

Figure 66: Angular distributions in the $\pi^{0}\pi^{0}$ channel.

4.2. The $\pi^{\pm}\pi^{0}$ channel on liquid Deuterium

For the I=J=1 channel, the program code was taken over from the I=J=0 channel as far as possible, to assure a direct comparison between the channels.

Background subtraction

The Background subtraction was also performed as described in 3.3.1.

Number of Clusters

Because in this channel only one neutral pion and one charged pion was required, the analysis was looking for two photons and a charged pion. The limited particle discrimination between a photon and an neutron was taken into account by allowing also here for

an additional photon. Using combinatorics again, the π^0 was composed from the photons which formed the mass closest to the nominal π^0 mass with the lowest ξ^2, see equation 52.

$$\xi^2 = (m_{\gamma_1\gamma_2} - m_{\pi^0})^2 \tag{52}$$

Cut on the incident photon energy

Events with incident photon energies in the range of 400-460 MeV have been selected.

Opening angle cut

As in the neutral channel, a minimum opening angle, of 30° for the photons from the π^0 decay was required.

Missing mass analysis

Here a missing mass cut $M_{miss} \geq 860$ MeV was applied. In figure 67 the red represents again the missing mass for the LD_2 data, black and blue are the quasi free channels on the neutron and proton as determined from simulation.

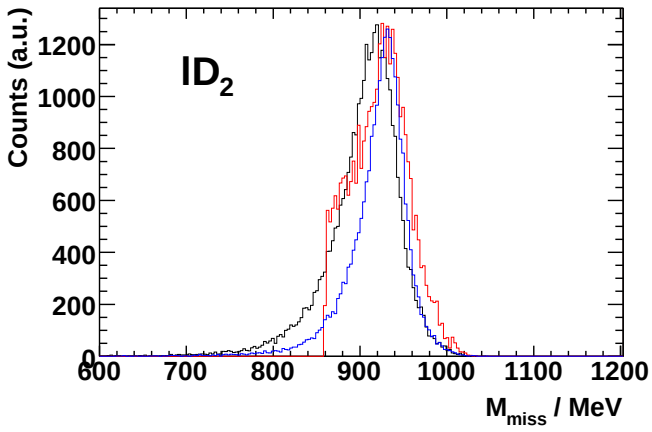

Figure 67: Missing mass in the $\pi^{\pm}\pi^0$ channel.
The black histograms is the missing mass spectrum from simulation for the channel $\gamma n \rightarrow \pi^-\pi^0 p$, the blue one for $\gamma p \rightarrow \pi^+\pi^0 n$. The red curve shows the missing mass from the analysis of experimental data in the $\pi^{\pm}\pi^0$ channel.

Pion mass cut

The mass cut of the π^0 in the charged channel was treated like the neutral pion channel.

A broad cut of 80 - 180 MeV was chosen to be able to extrapolate the background with a fit function in the next steps.

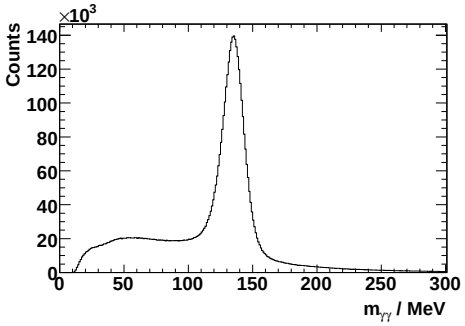

Figure 68: π^0 mass distributions in the $\pi^{\pm}\pi^0$ channel for incident photon energies from 400 to 460 MeV.

Cut on the $\pi\pi$-mass bins

Like in the $\pi^0\pi^0$ channel, the invariant masses of the $\pi\pi$ pair was determined and plotted against the invariant mass of the π^0 like it is shown in figure 69. The invariant mass spectrum was also sliced into 5 MeV wide mass bins from $m_{\pi\pi} = 270 \ldots 390$ MeV. For each mass bin the mass of the neutral pion was plotted (as in the neutral isospin channels).

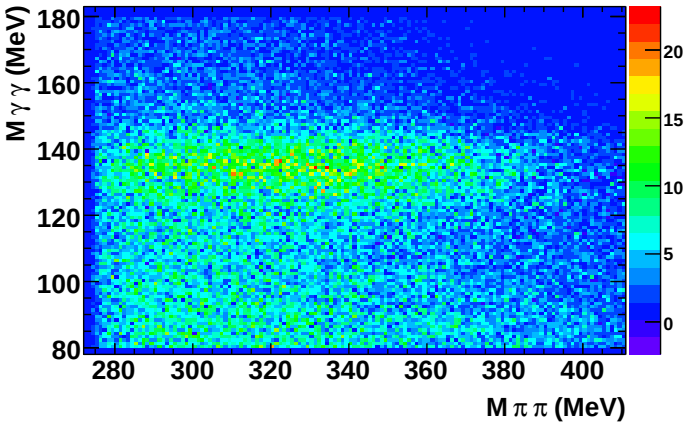

Figure 69: $m_{\gamma\gamma}$ versus $m_{\pi\pi}$ of the π^0 in the charged channel for 400-460 MeV incident photon energy.

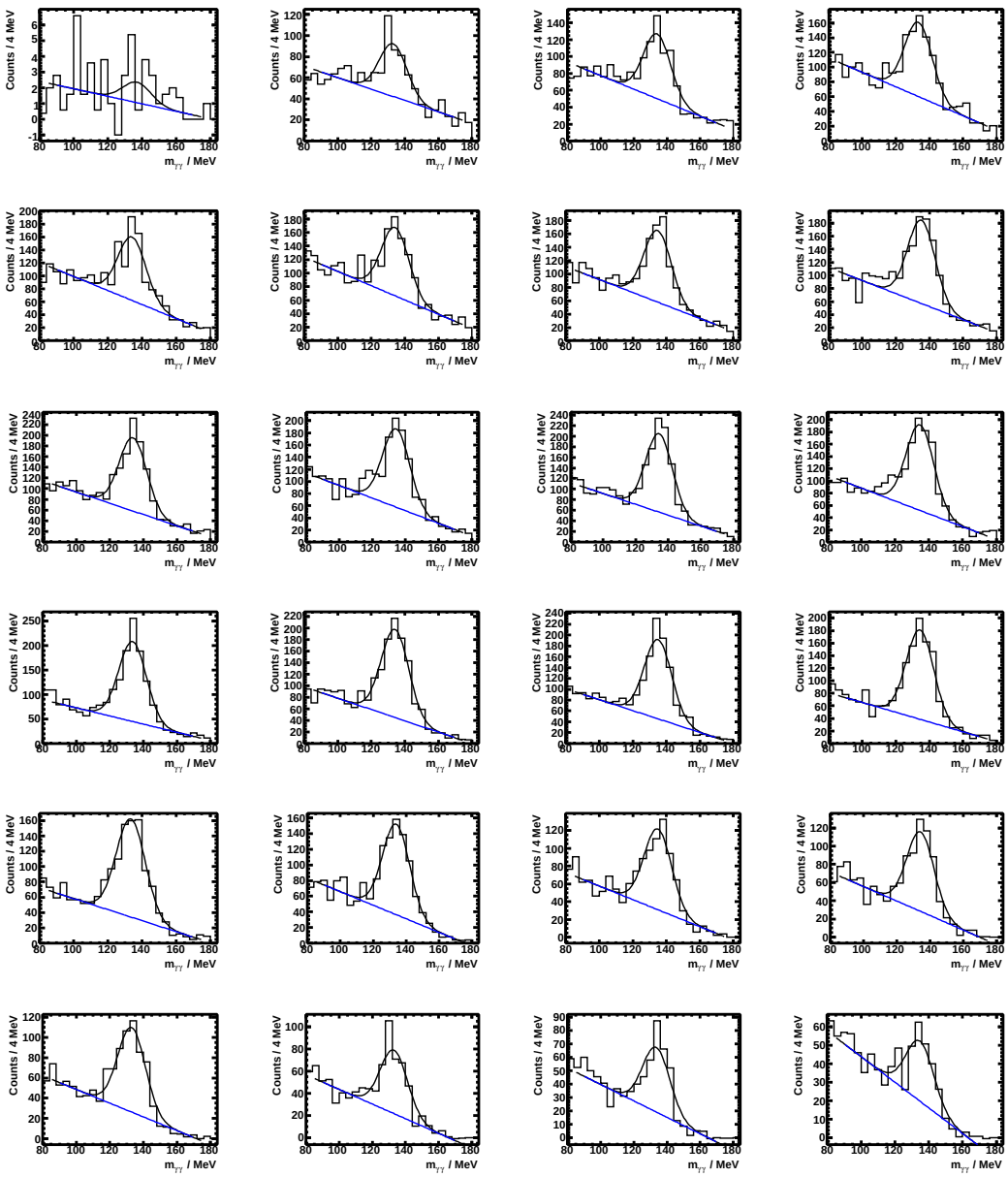

Figure 70: $m_{\gamma\gamma}$ spectra for the 5 MeV wide mass bins in the mass range from 275 MeV to 395 MeV in the $\pi^{\pm}\pi^{0}$ channel for 400-460 MeV incident photon energy. Fitted was a gaussian plus linear background in the range of 85-175 MeV, the width was allowed to vary between 8.2 and 9.0 MeV, the peak position between 133 and 137 MeV.

The background was also fitted linearly and superimposed with a gaussian in the peak area. From this, the mass distribution of the pion pairs was determined with improved background subtraction. The result is shown in figure 71.

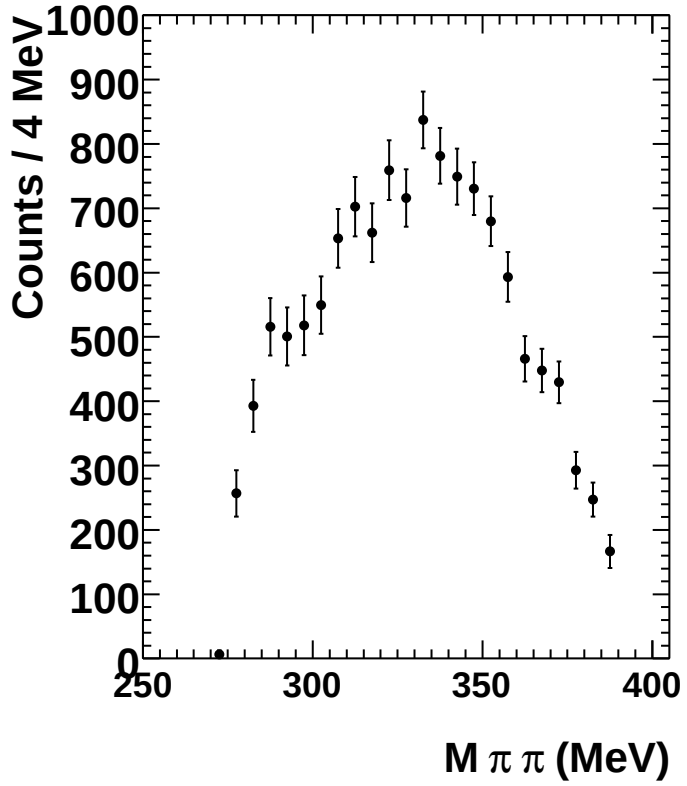

Figure 71: Mass distribution in the $\pi^{\pm}\pi^{0}$ channel for 400-460 MeV incident photon energy.

As two of the PID elements did not work properly, those two channels were masked. This effect is visible in figure 72 right hand side. As described in [Gre07], an enhancement of the neutral pion yield results from these broken channels in that azimuthal angle range.

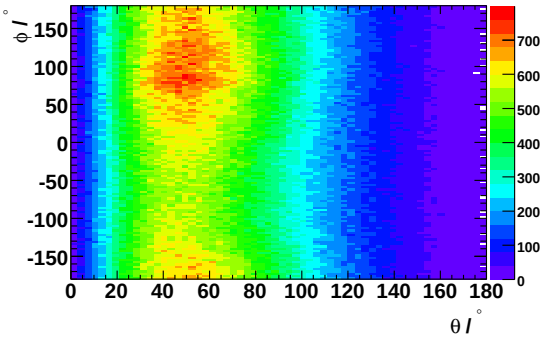

Angular distribution of the π^0.

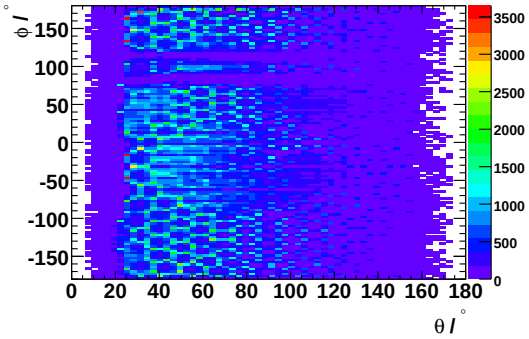

Angular distribution of the $\pi^{\pm}$.

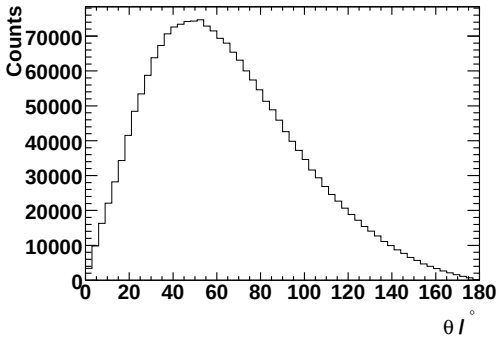

θ-angle distribution of the π^0.

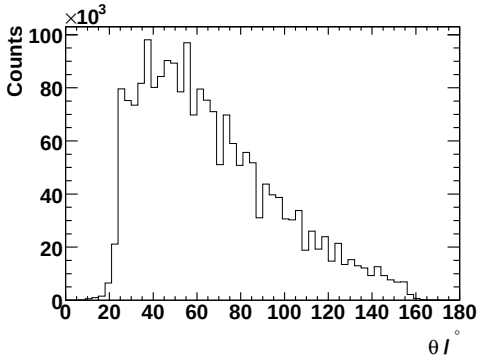

θ-angle distribution of the $\pi^{\pm}$.

Figure 72: Angular distributions in the $\pi^{\pm}\pi^0$ channel.

5. MonteCarlo simulation

As pointed out in the previous chapter it is possible to detect reaction products and to combine them to the events of interest. It is easy to count the number of events and to determine a relation to the incident beam properties, but due to threshold energies in the detector elements and the fact that the detector does not cover the whole solid angle, these results are not directly comparable to corresponding experiments and nor to theoretical models. Simulations of the reactions are needed to determine the detector response. From the number of registered events a cross section for the process is deduced and given by equation 53:

$$\sigma\left(E_\gamma, m_{\pi\pi}\right) = \frac{N_{event}\left(E_\gamma, m_{\pi\pi}\right)}{\epsilon\left(E_\gamma, m_{\pi\pi}\right) \cdot \Gamma_{br} \cdot N_{target} \cdot N_\gamma\left(E_\gamma\right)} \tag{53}$$

with:

- $N_{event}\left(E_\gamma\right)$ - number of reconstructed events in the beam energy bin.
- $\epsilon\left(E_\gamma\right)$ - detection efficiency, calculated from simulations.
- Γ_{br} - branching ratio of the observed channel.
- N_{target} - number of target nuclei per cm^2 - see chapter 2.4.
- $N_\gamma\left(E_\gamma\right)$ - number of beam photons hitting the target
  $N_\gamma\left(E_\gamma\right) = scalers\left(E_\gamma\right) \cdot \epsilon_{tagging}\left(E_\gamma\right)$.

Another reason for using simulations is to determine the background for any given reaction. Simulations are also necessary to determine the efficiency of cuts applied applied in the analysis.
Monte Carlo methods are a widely used class of computational algorithms for simulating the behavior of various physical and mathematical systems, and for other computations. The standard program to perform simulations in nuclear physics is the GEANT package [GEA94] which will be described in section 5.2.

5.1. Event generator

To produce the particles that can interact with the elements (described in the GEANT setup files), an event generator is needed.
For response measurements and for checking the whole geometrical setup, a very simple event generator was developed. It mainly consists of a random number generator which produces arbitrary values for the angles and momenta (θ, ϕ and $|p|$) in a given range for the chosen particles. As this generator was only able to produce one particle per event, the relative alignment of the detector elements, the correctness of the energy deposition in the materials and other basic checks could be performed by parsing the data through the simulation and the analysis code. θ and ϕ are given in radians, but as the simulation expects direction unit vectors in x,y,z, momentum, and energy, the values were transformed

the following way:

$$
\begin{aligned}
P_x &= sin\,(\theta) \cdot cos\,(\phi) && (54)\\
P_y &= sin\,(\theta) \cdot sin\,(\phi) && (55)\\
P_z &= cos\,(\theta) && (56)\\
|p_{tot}| &= |p| + m_{Particle} && (57)\\
E &= \sqrt{p_{tot}^2 - m_{particle}^2} && (58)
\end{aligned}
$$

As this event generator is not sufficient for the analysis of decaying particles, another one, which produces a three-body decay was developed. This event generator chooses the incident photon energy from any given distribution function (e.g. $1/E_\gamma$ or flat distribution) for a given energy range. For the studied reactions only quasi free production will be assumed. Moreover, even if the nucleus is at rest, all nucleons have momenta in some direction, so they are in motion. This is called Fermi motion. Effects of that Fermi motion will be discussed later. Depending on the nucleon and the photon energy, the center of mass energy is calculated, and if it is large enough to produce two pions on the nucleon, a GEANT function, GDECA3 is executed. The center of mass energy is given by:

$$
\begin{aligned}
s &= m_N^2 + 2 \cdot E_\gamma \cdot m_N && (59)\\
w &= \sqrt{s} \geq 2 \cdot m_\pi + m_N && (60)
\end{aligned}
$$

The return values of this function are angles and the four momenta in the center of mass (CM) system. As GEANT requires those variables in the laboratory system (LAB), they have to be transformed in the following way where p^i denotes the components of the four-momentum vectors (E, $\overrightarrow{p}$):

$$
\begin{aligned}
|\overrightarrow{p_{CM}}| &= \sqrt{\left(p^4_{CM}\right)^2 - m^2_{\pi,p}} && (61)\\
\theta_{CM} &= arccos\left(\frac{p^3_{CM}}{|\overrightarrow{p_{CM}}|}\right) && (62)\\
\phi_{CM} &= arctan\left(\frac{p^2_{CM}}{p^1_{CM}}\right) && (63)\\
\beta &= \frac{E_\gamma}{E_\gamma + m_{\pi,p}} && (64)\\
\gamma &= \frac{1}{\sqrt{1-\beta^2}} && (65)\\
p^4_L &= \gamma \cdot p^4_{CM} + \beta \cdot \gamma p^3_{CM} && (66)\\
p^3_L &= \gamma \cdot p^3_{CM} + \beta \cdot \gamma p^4_{CM} && (67)\\
p^2_L &= p^2_{CM} && (68)\\
p^1_L &= p^1_{CM} && (69)
\end{aligned}
$$

The values are then stored in an Ntuple file which later on can be read by GEANT. This event generator was set up in such a way that either the $\pi^0\pi^0$ or the $\pi^+\pi^0/\pi^-\pi^0$ channel on the neutron or proton were using the same routines. This means that all initially generated particles of the relevant channels were calculated exactly the same way. The auto tracking routine of GEANT does all tracking on its own, depending on the particles being generated. A time of flight cut on the particles that are generated was set to 500 ns in order to exclude the energy of the decay muons from contributing to the total energy that is deposited in the detector.

FERMI MOMENTA

Every single nucleon inside a nucleus can have a momentum. The nucleus is at rest when the sum of all nucleon momenta is zero. The motion of the nucleons is called Fermi momentum and it has to be taken into account by studying quasi free production mechanisms. Fermi momenta are of the order of 100 MeV and they play an important role in the reaction kinematics. Therefore this effect also has to be implemented into the simulation. A random Fermi momentum in an arbitrary direction is calculated from a given distribution file which is shown in figure 73.

The momentum of the nucleon is smeared by the distribution function. This modified nucleon momentum then is read in the GDECA3 function, described above.
As the Fermi momenta rise logarithmically with increasing atomic number, the difference between the distributions becomes marginal for the heavy nuclei. Because of this, for all heavy nuclei (except for the deuteron), the same Fermi distribution file was used in this work [Kru07]. Figure 74 shows the effect of Fermi motion on the missing mass for a nucleon.

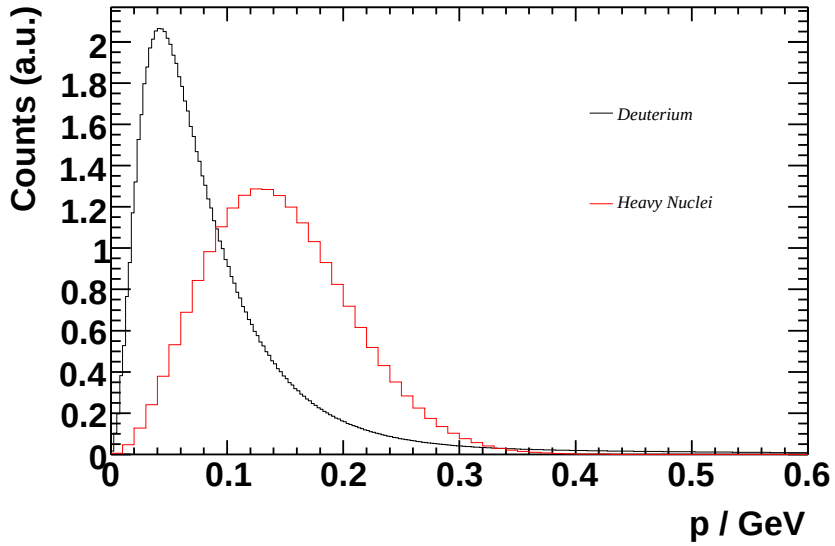

Figure 73: Fermi momentum distribution functions.
The black curve was used for Deuterium and the red one for C, Ca and Pb.

The final event generator was configured to run with parameters read in from a parameter file. In these files the following information was stored:

1. number of events to be thrown, normally 100,000 per channel.
2. reaction type - to be able to study differences in the detector response and to extract the efficiency on the different channels, the following numbering was used:

$$\begin{array}{ll} 0 & \gamma p \rightarrow \pi^0\pi^0 p \\ 1 & \gamma n \rightarrow \pi^0\pi^0 n \\ 2 & \gamma p \rightarrow \pi^0\pi^+ n \\ 3 & \gamma n \rightarrow \pi^0\pi^- p \end{array}$$

3. minimum photon energy to be thrown
4. maximum photon energy to be thrown
5. type of photon spectrum (e.g. flat spectrum or bremsspectrum)
6. Fermi momentum file (optional, for nuclei different from hydrogen)
7. length and material of the used target

If the minimum photon energy specified in the datafile is large enough to produce the reaction products, e.g.. for $\gamma N \rightarrow \pi_1\pi_2 N$:

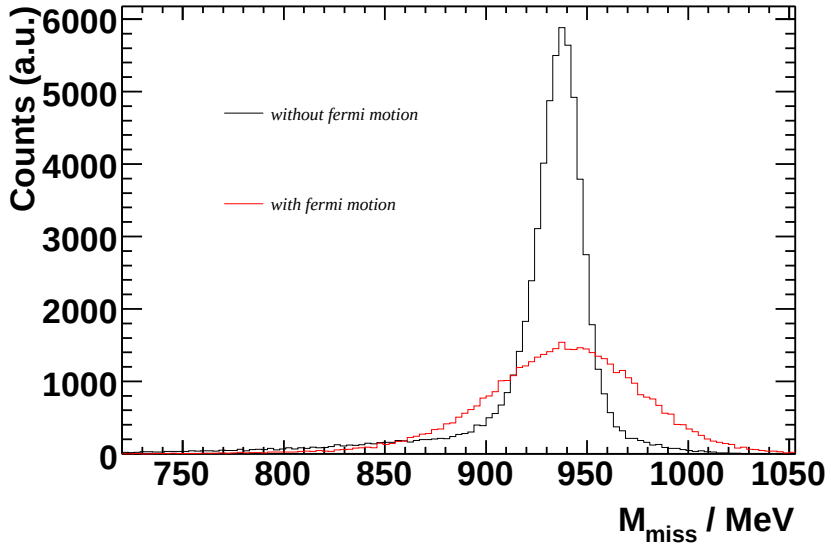

Figure 74: Comparison of the missing mass with/without Fermi motion for Ca on the $\pi^0\pi^0$ channel in the energy range of 400-460 MeV.

$$E_\gamma \geq \frac{(m_\pi + m_\pi + m_N)^2 - m_N^2}{2m_N} \tag{70}$$

then arbitrary photon energies are generated following the chosen photon spectrum distribution file. In the next step the vertex point in the cylindrical target volume is calculated and the Fermi momentum is added to the nucleon at rest. The values are given to GDECA3, a three body kinematic routine of GEANT to calculate the four momenta of the reaction products. After having transformed those from CM into LAB system, some diagnostic spectra are filled and all necessary values for GEANT to track the particles event-by-event are written into a treefile.

5.2. GEANT 3

The simulation of events was performed using the simulation package GEANT. These programs calculate all interactions of the generated particles with any material. Therefore, it was necessary to implement the whole detector setup with all relevant detector elements and materials in Fortran code. As a skeleton for the experimental setup described in chapter 2, the MonteCarlo framework developed by the Crystal Ball Collaboration [Cla05],

initially modified by John Price, was used. But nevertheless, several patches and changes were implemented lateron:

- Adding the PID
- Adding the MWPC
- Changing the TAPS geometry
- Adding Energy loss in cylindrical part of BaF_2
- Increase thickness of Veto-Box, front and rear
- Changing the VETO geometry
- Adding energy loss in the VETOS
- Adding readout of the VETOS
- Adding an aluminum box around TAPS
- Simulate VETO lightguides
- Adding TAPS dummy detectors
- Adding air cone around the cylindrical endcaps
- Changing the geometry of the inner CB shell
- Changing to thicker steel cylinder in the CB tunnel
- Adding two additional volumes simulating the cables from the PID and the MWPC in the CB tunnel
- Modification of the tunnel region with a metal disc perpendicular to the beam axis
- Inserting some 64 screws in the inner sphere
- Inserting a metal strip in the exit tunnel
- Inserting skirts in the beam tunels
- Implementation of solid targets

All these modifications have been performed by E.Downie, V. Kashevarov, S.Lugert, S.Schumann, M. Unverzagt. Most of them are shown in figure 75.

All settings in the GEANT3 packages are managed by a parameter file, the *.ffcards which is shown in Appendix A.10.

A specific problem was introduced with the π^+ simulation. While the π^- may be absorbed by nuclei after they deposited their energy, the π^+ decay into antimuons after $2.6 \cdot 10^{-8}$ s. Once the anti-muons deposit their small energy of 4,2 MeV, see [PDG04], they are trapped and decay after some micro seconds ($2.2 \cdot 10^{-6}$ s) into electrons. Most muons decay in the experiment after the electronics gates are closed. No trace of the deposited

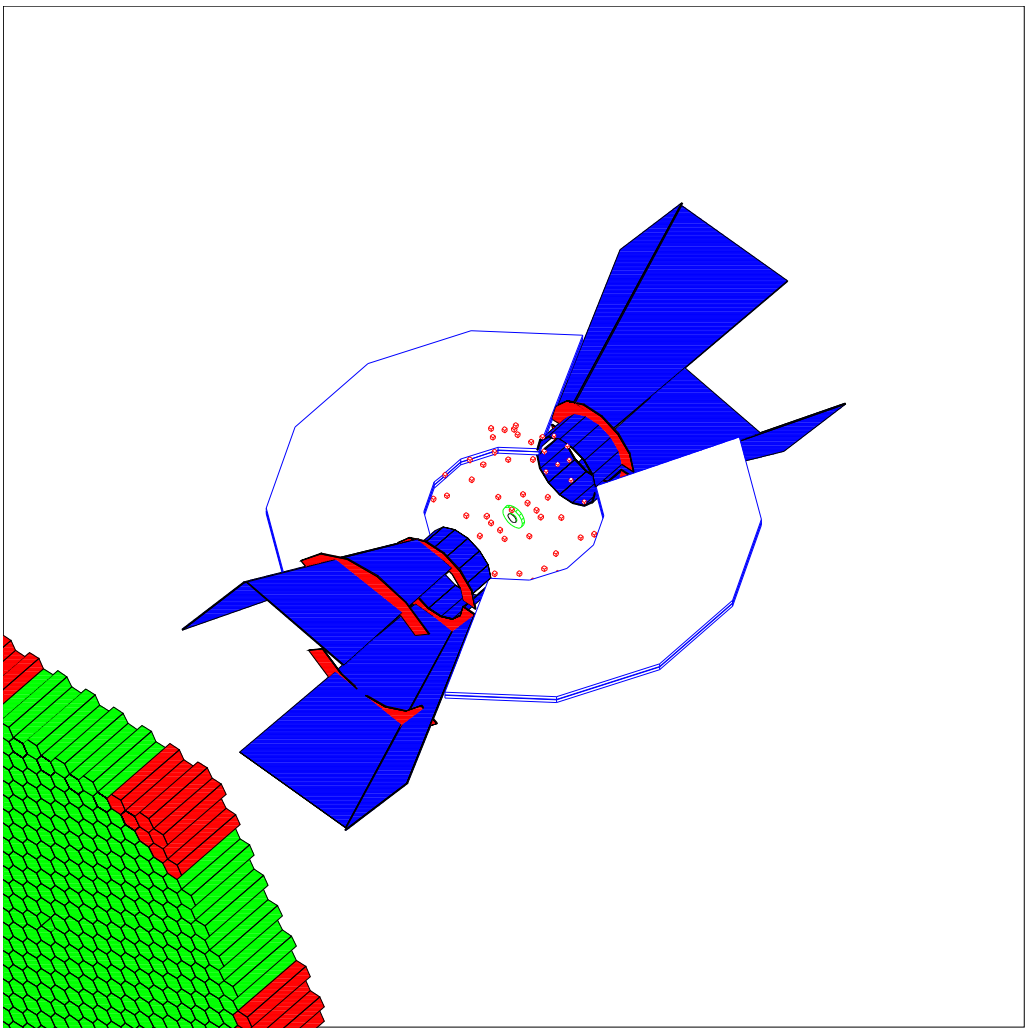

Figure 75: CB/TAPS detector in GEANT geometry with improvements in the setup as described in the text.

energy from the muon decay products exists in the data. This is not the default case of the simulation. It was therefore necessary to stop the tracking of particles in the simulation after a time ($5 \cdot 10^{-7}$ s). Only with this specification was it possible to get rid of extra deposited energy and extra detector hits in π^+ clusters. π^- form pionic atoms within a few ps. This decay releases additional energy in the detectors. To accommodate that effect, the simulation was performed with equal numbers of π^+ and π^-. The resulting efficiencies were averaged in the following.

5.3. Geometry

Figure 76 shows the complete simulation setup of the CBTAPS detector system in the GEANT simulation framework.

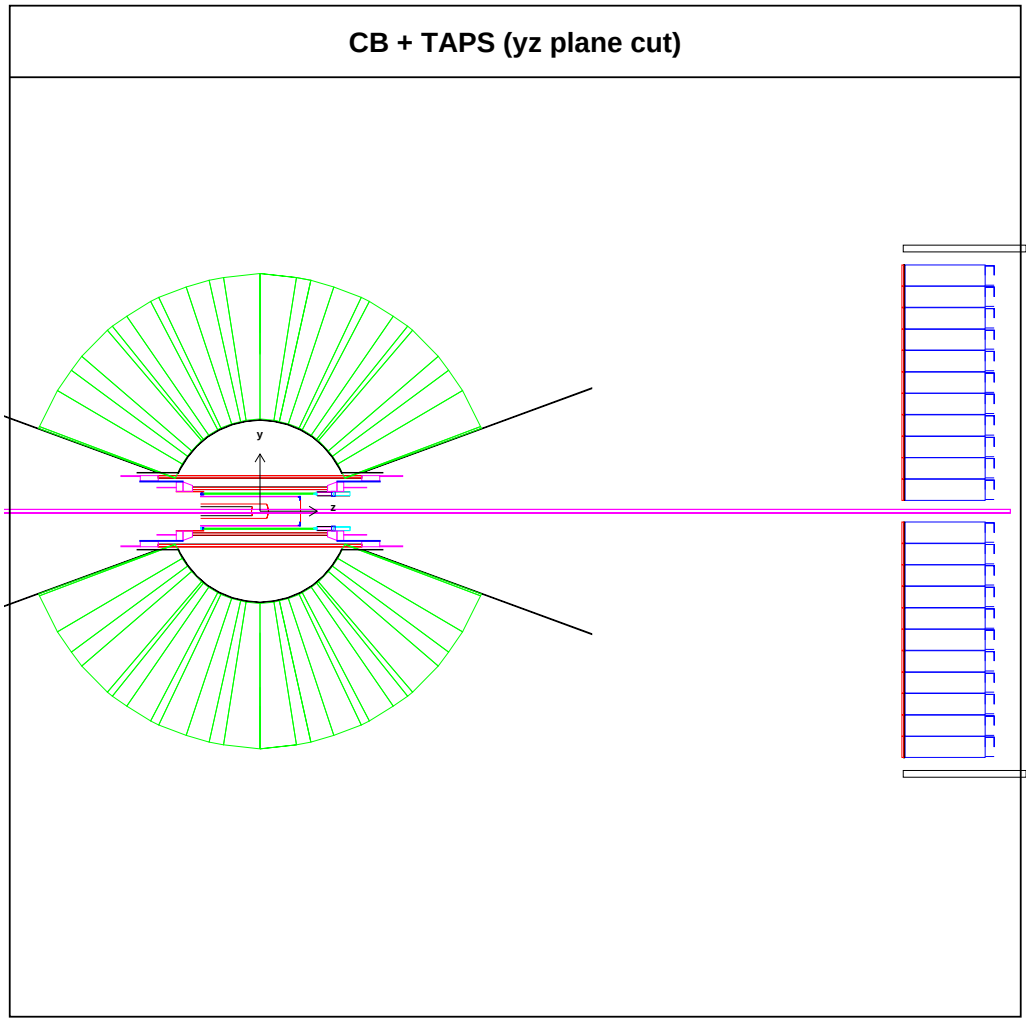

Figure 76: Simulation Setup in cut view.

The setup in GEANT has an inverse tree structure. TAPS, for example, consists of several hundred single elements. The base of the crystals is a volume element in hexagonal shape, 59 mm in thickness and 225 mm length. Attached to this is a cylindrical element with 25 mm length and 54 mm diameter. Assigned to these elements are the properties (atomic number, density and nuclear mass) of BaF_2. To take into account rescattering, a cylinder (inner diameter 54 mm, outer diameter 59 mm) having the properties of air is surrounding the cylindrical part of the crystal. All crystals are positioned in a huge hexagonal aluminum box referring to the numbering of the crystals in the experiment. In the same positioning routine, the CPV plastic scintillators with a thickness of 5 mm are also aligned a few mm in front of the BaF_2's to avoid misalignment of BaF_2 and CPV

numbering. Like in the experiment, dummy crystals were also filled in the corners of the aluminum box. In figure 77 the CPV's are shown as a white layer in front of TAPS, the BaF_2 crystals are green and the dummy detectors are given in red.
For the simulation of the CB, there are the two hemispheres, containing outer and inner cones. The cones were defined, containing the major triangles, that again contain the minor triangles, which finally contain the crystals.
To fill up the triangles consistently, 11 types of NaI crystals with slightly different shapes had to be generated. 9 crystals are combined in each minor triangle. Because there are holes for the beamline, besides the "normal" minor triangle, 12 minor triangles with different shapes for the beam entry and exit were defined. Four minor triangles are combined in each major triangle. As the CB is not a real icosahedral body due to the sub division into two hemispheres, 7 types of major triangles are needed to fill up the whole geometry of the two hemispheres of the CB.
Finally, the main detector components like CB, TAPS, MWPC, PID, Skirts and Target are positioned in the virtual lab the same way they were in the experiment
The bremsstrahlungs mechanism itself was not simulated instead a beam energy distribution file was read in. Therefore there was no need to simulate the tagger.

5.4. Tracking

The tree file generated by the event generator contains all necessary parameters of an event to be tracked. Tracking refers to the simulation of the passage of elementary particles through the matter.
In GEANT, tracking a particle through a geometry of objects consists of calculating a set of points in a seven dimensional space (x, y, z, t, px, py, pz) which is called the trajectory of the particle. To have a detailed description of the kinematic of the particle it would be necessary to calculate a trajectory point every time the component of the momentum change. This is not possible because it would mean calculating an enormously large number of points. Processes like the deflection of a charged particle in a magnetic field, the loss of energy due to bremsstrahlung and ionization or the deflection due to elastic electromagnetic scattering are essentially continuous. An arbitrary distinction is thus made between discrete and continuous processes, which is controlled by a set of thresholds which can be set by the user. A particle trajectory is thus a set of points at which a discrete process has occurred. The tracking package contains a subprogram which performs the tracking for all particles in the current event and for the secondary products which they generate, plus some tools for storing the space point coordinates computed along the corresponding trajectories [GEA94]. The color- and linestyle in figure 77 refer to the track type (blue dotted $\hat{=}\gamma$; red solid $\hat{=}$ charged particles; black dashed $\hat{=}$ neutral hadrons; green dashed $\hat{=}$ muons).

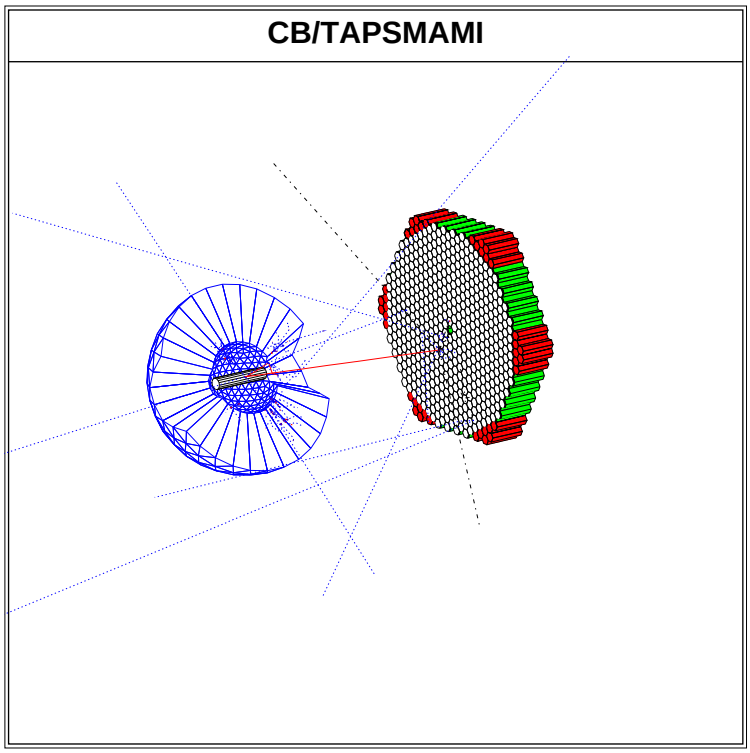

Figure 77: Trajectory of two events in the $\pi^{\pm}\pi^{0}$ channel.
The color code of the lines is explained in the text.

5.5. Analysis and efficiency determination

To determine the efficiency of the setup, the simulated and tracked data have to be analyzed in the same way the real data is processed. As in the tracking routine of GEANT, an additional energy smearing for BaF_2 and NaI was switched off. The following smearing terms were added to the import functions of Acqu:

TAPS energy smearing:

$$E_{BaF_2} = f_{TAPS}\left(E_0 + 0.03 \cdot e^{-0.5\cdot\left(\frac{E_0}{0.75}\right)^2}\right) \tag{71}$$

CB energy smearing:

$$E_{NaI} = f_{CB}\left((E_0 + 0.027 \cdot e^{-0.5\cdot\left(\frac{E_0}{0.75}\right)^2}\right) \tag{72}$$

[Dow07].
In the experiment the CPV's provided a bit pattern whether they fired or not. To register low energetic particles, the discriminators of the Vetos had to be set slightly above threshold. GEANT provides the energy deposited in the plastic scintillators. A threshold value of 50 keV was set for the simulated data to transform the deposited energy into a hit pattern.

5.5.1. The $\pi^0\pi^0$ channel

The analysis of the I=0 channel was set up the following way:
After having selected all events with 4 or 5 photons and no charged pion, the photons were combined pair-wise to π^0s and the best combination was taken for the next steps. A cut on the mass of the two pions $80MeV \leq m_\pi \leq 180MeV$ and a missing mass cut $M_{miss} = \sqrt{P_\gamma + P_N - P_{\pi_1^0} - P_{\pi_2^0}} \geq 860MeV$ were applied to select events corresponding to quasi free $2\pi^0$ production.

5.5.2. The $\pi^\pm\pi^0$ channel

In contrast to the neutral channel, a charged pion in the charged channel was demanded. The identification was done by a two dimensional cut in the ΔE_{PID} versus E_{NaI} plot like it is shown in figure 78. Moreover, a neutral pion was formed by combining 2 photons to form a neutral pion. The best combination was taken. A cut on the mass of the two pions $80MeV \leq m_\pi \leq 180MeV$ and a missing mass cut $M_{miss} = \sqrt{P_\gamma + P_N - P_{\pi_1^0} - P_{\pi_2^0}} \geq 860MeV$ were then applied.

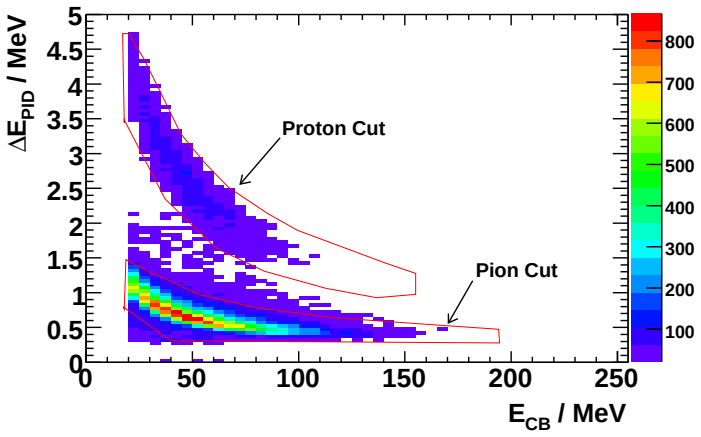

Figure 78: Particle identification using the $\Delta E/E$ information from simulation.

5.5.3. Resolution effect

To determine the detector system efficiency, the mass distribution of reconstructed $\pi\pi$ events had to be divided by the $\pi\pi$-masses of the start distribution. The result will be a mass dependant efficiency. Since the start distribution does not have included the detector resolution, it is necessary to fold it with a gaussian resolution function. This was important especially at the threshold and phasespace limit.

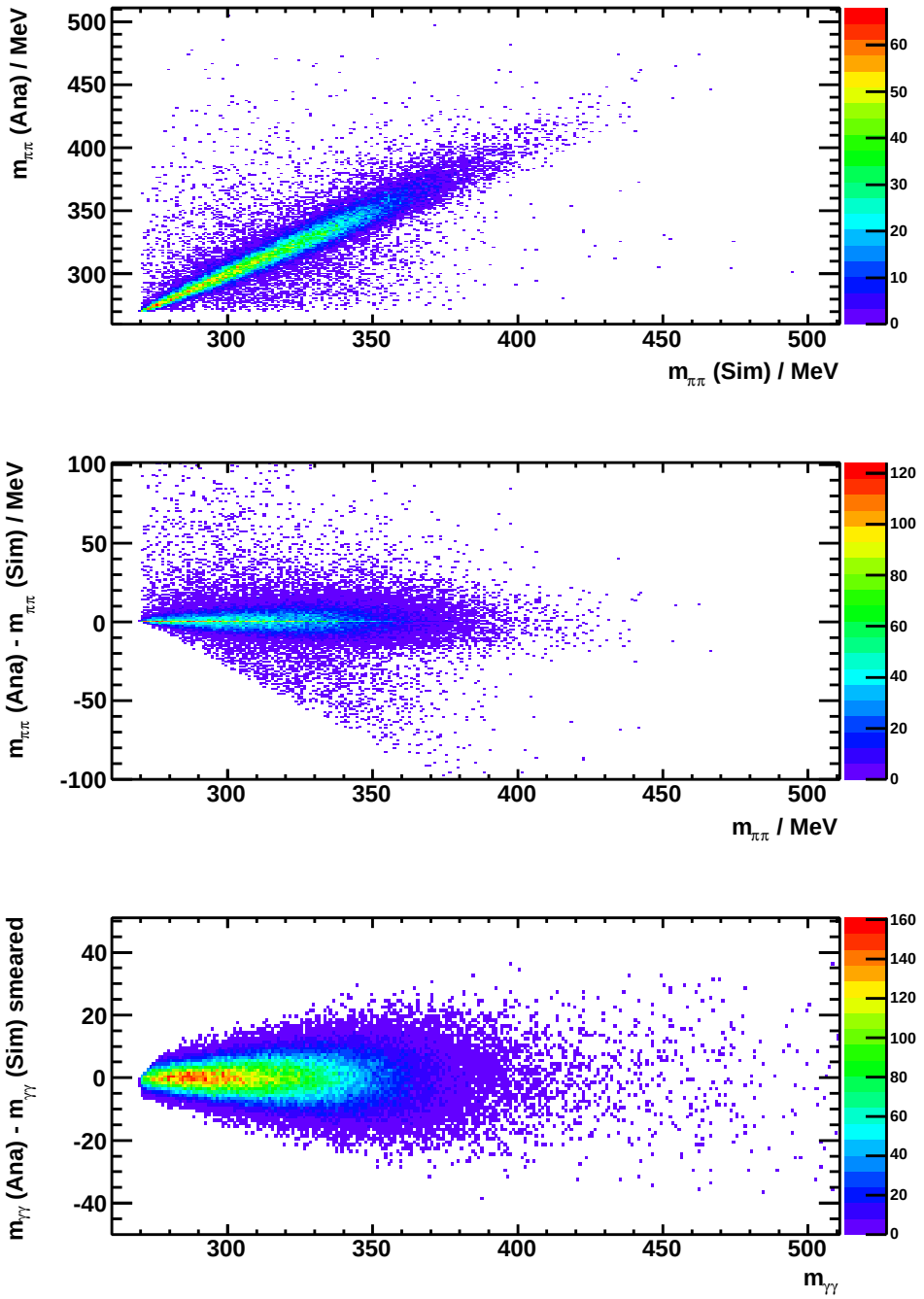

Figure 79: Resolution adaption of start distribution.
The top figure shows $m_{\pi\pi}$ of the analyzed simulation versus the start distribution, in the middle, the difference of start distribution and analyzed data is plotted against the analyzed data and the bottom figure shows the difference after the resolution correction.

	Intensity	
Cut	$\pi^0\pi^0$-channel	$\pi^\pm\pi^0$-channel
Start distribution	100%	100%
Photon multiplicity	97.8%	85.9%
$80MeV \leq m_\pi \leq 180MeV$	63.5%	40.6%
$\angle_{\gamma\gamma} \leq 30°$	47.2%	40.4%
$M_{miss} \geq 860MeV$	46.2%	39.1%

Table 14: Overview of all applied cuts.

To determine this resolution, for both simulated data (ANA) and start distribution (STD), the mass of the two pion system was plotted against the event number (as unique ID of the event) and stored in a root file. In the second step, as shown in figure 79 top, $m_{\pi\pi}$ of the analyzed events is plotted agains $m_{\pi\pi}$ of the start distribution. In the middle plot of figure 79, the difference between ANA and STD is plotted against ANA. The $\pi\pi$-mass range is cut into 30 MeV slices and fitted with a gaussian which is shown in figure 80.

The width (or σ) of the distribution is determined as a resolution parameter. Using this linear mass dependant smearing parameter (fig. 80 bottom right), the STD is modified and, by dividing ANA by STD, the efficiency of the channel is determined. In the last step, a second order polynom is fitted to the data.

Figure 81 shows the original start distribution (red), the smeared start distribution (blue) and the mass distribution from the analyzed simulation data (black). To proceed with the simulated data in the same way as described for the experimental data, the following steps were performed. In a two dimensional histogram, $m_{\gamma\gamma}$ was plotted against $m_{\pi\pi}$. This histogram was sliced into 5 MeV bins on the $m_{\pi\pi}$ axis. Then a gaussian was fitted according to determine the π^0 yield in the same way as for the Deuterium data. The only difference here is, that there was no need to fit a linear background. The figures for the simulation are shown in figure 82.

The over all efficiency for the channel $\gamma + D_2 \longrightarrow \pi^0\pi^0X$ in the interesting $\pi\pi$ mass region of $270 \ldots 390$ MeV is shown in figure 83, for $\gamma + D_2 \longrightarrow \pi^\pm\pi^0X$ it is shown in figure 84.

Also the missing masses in the neutral and charged channels for all targets were compared to the missing masses from the data analysis which is shown in figures 85 and 86.

The trigger efficiency was also taken into account. The following parameters were required in the simulation: The energy sum in the CB had to be larger than 50 MeV, the multiplicity was set to $M \geq 2$, the TAPS LED thresholds were set to 30 MeV and the discriminator thresholds of the CB were set to 20 MeV.

Table 14 gives an overview of all applied cuts and the remaining amount of events in the $\pi\pi$ channels in percent.

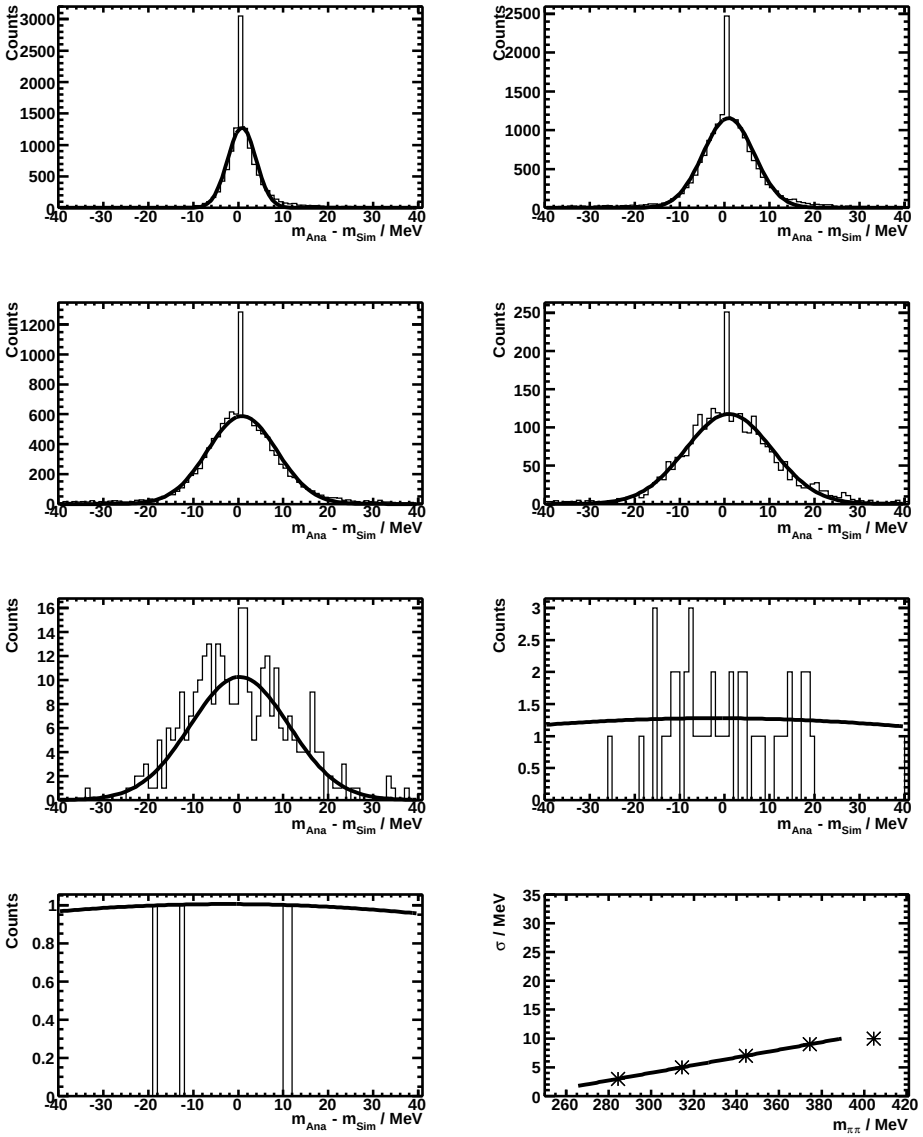

Figure 80: Resolution adaption of start distribution.
Shown are 30 MeV slices of figure 79 bottom with a gaussian fit for width determination.
The bottom right plot shows the width of the fit as function of the $\pi\pi$ mass.

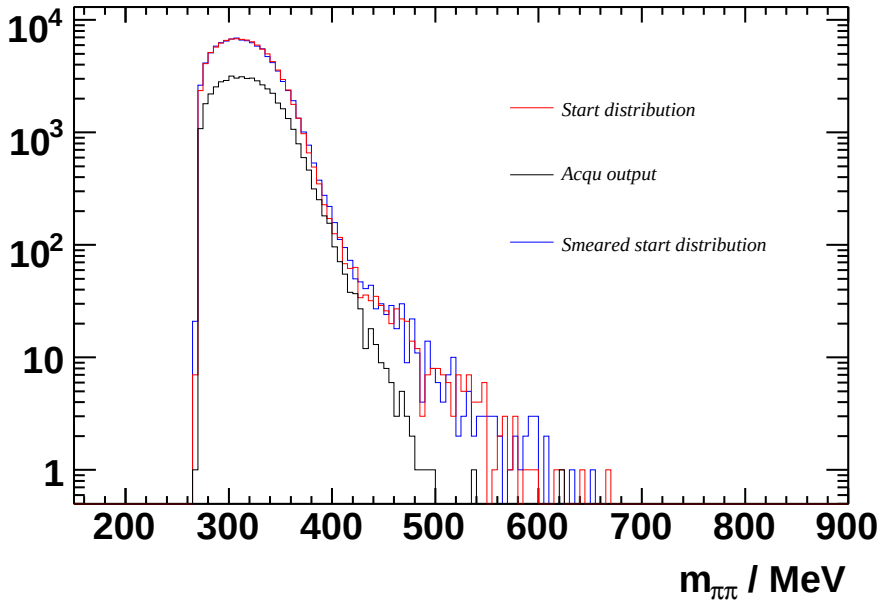

Figure 81: $2\pi^0$ start distribution, resolution corrected start distribution and analyzed simulation spectrum.

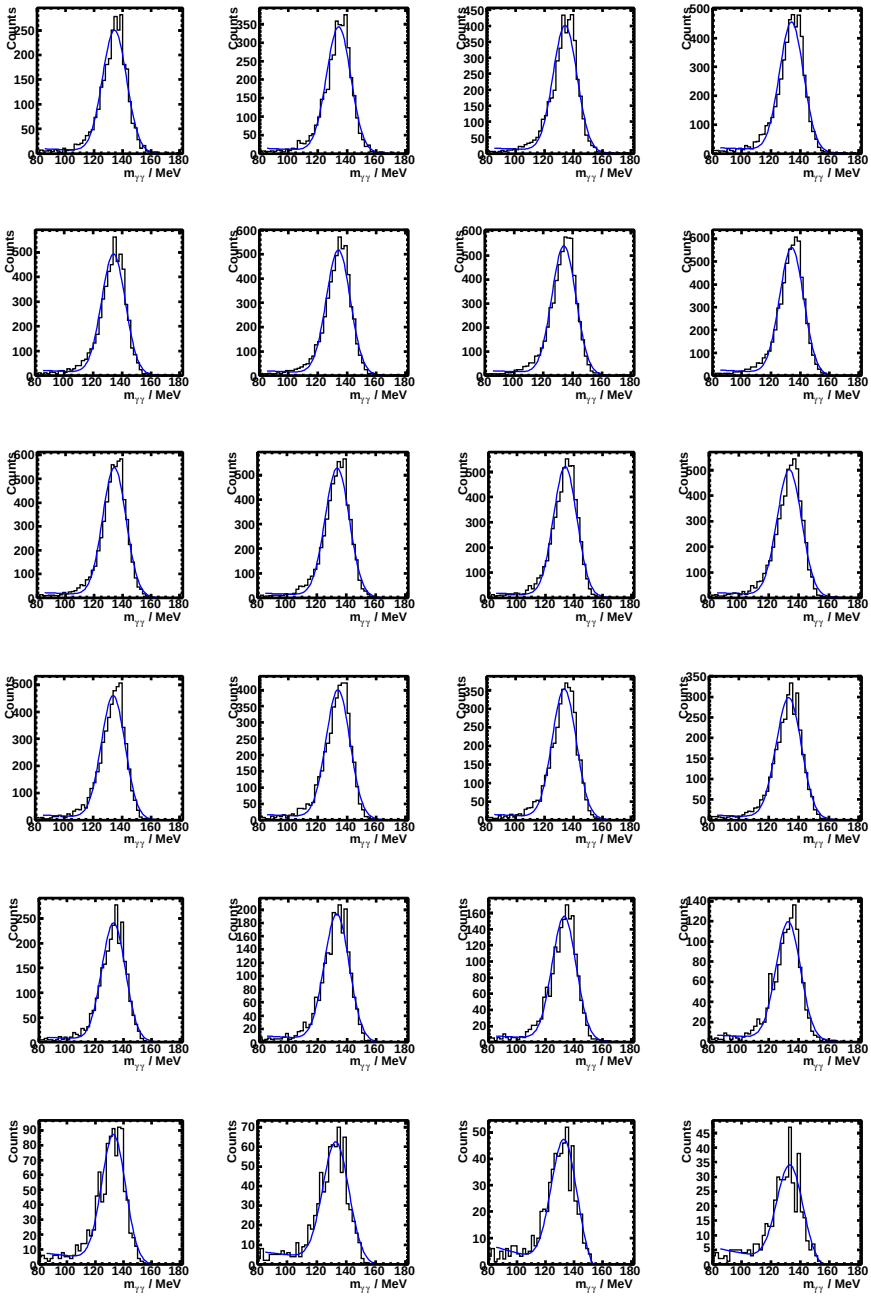

Figure 82: Simulated $m_{\gamma\gamma}$ distributions for $275MeV \leq m_{\pi^0\pi^0} \leq 395MeV$ in 5 MeV slices for the $\pi^0\pi^0$ channel.

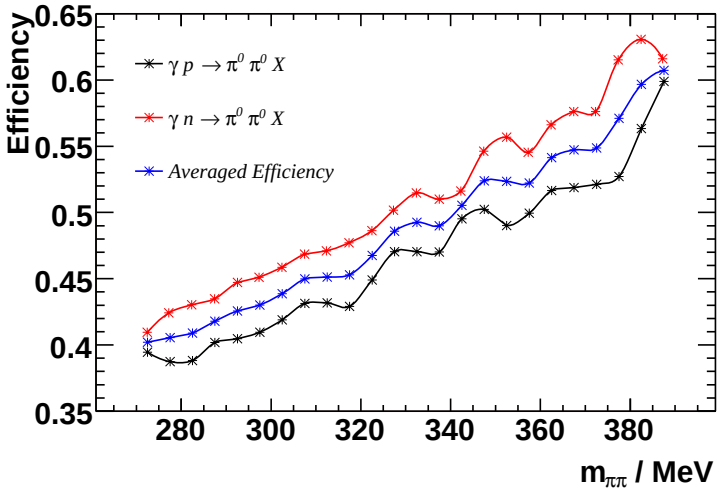

Figure 83: Efficiency for the $\pi^0\pi^0$ channel on liquid Deuterium in the energy range of 400-460 MeV.

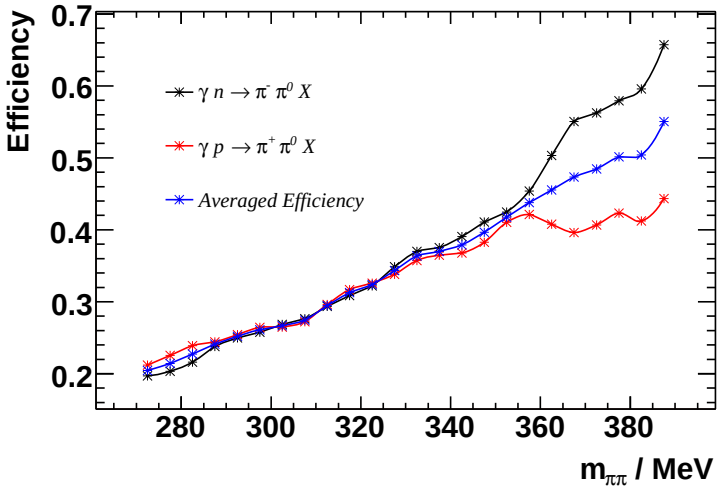

Figure 84: Efficiency for the $\pi^{\pm}\pi^0$ channel on liquid Deuterium in the energy range of 400-460 MeV.

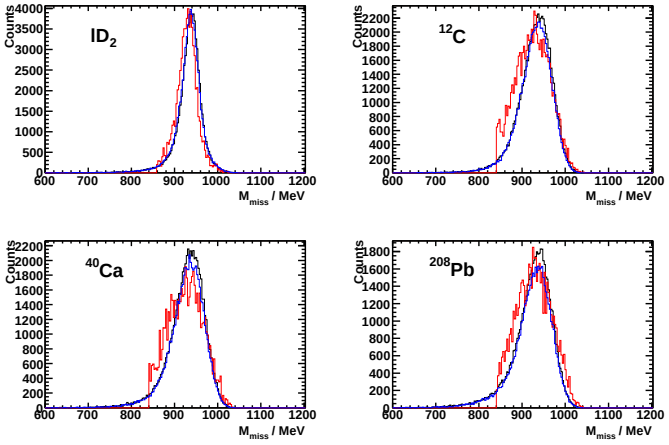

Figure 85: Comparison of the missing masses for the $\pi^0\pi^0$ channel for the targets ^2H, ^{12}C, ^{40}Ca and ^{208}Pb.
The black histograms represent the missing mass spectra from simulation for the channel $\gamma n \to \pi^0\pi^0 n$, the blue ones for $\gamma p \to \pi^0\pi^0 p$ including Fermi momenta. The red curves show the missing mass from the analysis of experimental data in the $\pi^0\pi^0$ channel.

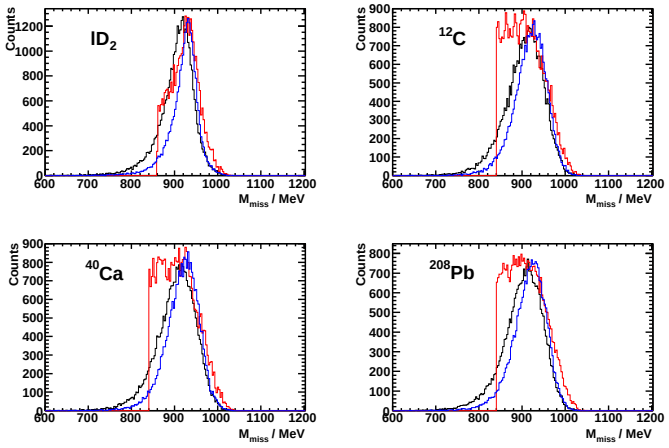

Figure 86: Comparison of the missing masses for the $\pi^{\pm}\pi^0$ channel for the targets ^2H, ^{12}C, ^{40}Ca and ^{208}Pb.
The black histograms is the missing mass spectrum from simulation for the channel $\gamma n \to \pi^-\pi^0 p$, the blue one for $\gamma p \to \pi^+\pi^0 n$ including Fermi momenta. The red curve shows the missing mass from the analysis of experimental data in the $\pi^{\pm}\pi^0$ channel.

6. Results

6.1. Determination of the mass differential cross section on liquid Deuterium

After having determined the mass distributions in the $\pi\pi$ channels for the incident photon energies from 400 to 460 MeV, and also the efficiencies for these channels, the mass differential cross sections of the considered channels were calculated. To be able to compare the cross section on the deuteron with the cross sections on the proton, the cross sections were not corrected for the $\frac{1}{E_\gamma}$ bremsspectrum. This chapter describes the procedure how to determine the cross section.

6.1.1. Cross section of the $\pi^0\pi^0$ channel

Knowing all parameters in equation 53, the mass differential cross section was calculated for each mass bin. The result is shown in figure 87 as black dots. To extract the mass differential cross section on the neutron, two different ways of analyzing the data were pursued.
By selecting events with 4 photons and one neutron in combination with a missing mass analysis (requiring an additional nucleon), the reaction kinematics is fixed. Because of the low detection efficiency for neutrons, the yield in this channel was very low. In addition, because of the low neutron-momenta and a relatively large surface density of insensitive material in front of the detectors, a large fraction of neutrons was stopped before reaching the detectors. A further problem was multiple scattering of the neutrons, which led to delayed energy deposition in the crystals in coincidence with wrongly determined four-momentum-vectors (due to energy loss in the insensitive volumes and distorted angular information). Even if requiring quasifree production on a neutron, the proton will also gain some amount of momentum as the photo-fission of Deuterium takes only 2.227 MeV. Having proton and neutron as moving particles, it is difficult to find out, on which particle the reaction took place. Because of these problems, this analysis was discarded.
The other way was, to take the difference of the mass differential cross section on the deuteron and the well known differential cross section on the proton, which was provided by [Kot07]. Theoretical calculations on this technique have been done by [Bus07] and it was found that this is an appropriate way of determining the cross section on the neutron. In figure 87, the cross sections on the proton (red stars) and neutron (blue triangles) are also shown. Table 17 in Appendix A.11 shows the numerical values of the cross sections in the $\pi^0\pi^0$ channel for d, p and n.

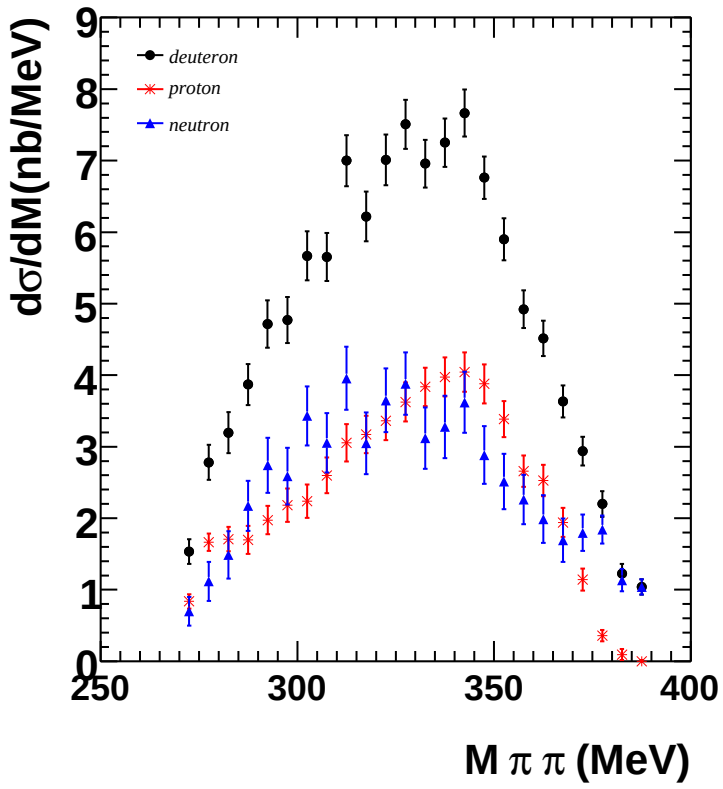

Figure 87: Mass differential cross section of the $\pi^0\pi^0$ channel for incident photon energies from 400 to 460 MeV.
The black dots show the cross section on Deuterium, the red stars represent the cross section on the proton, provided by [Kot07] and the blue triangles are the cross section on the neutron. See text for details.

The $\pi^0\pi^0$ mass differential cross section was also determined on the Deuterium for incident photon energies from 400 to 500 MeV (black dots) and compared to [Blo07] (red squares), which is shown in figure 88.

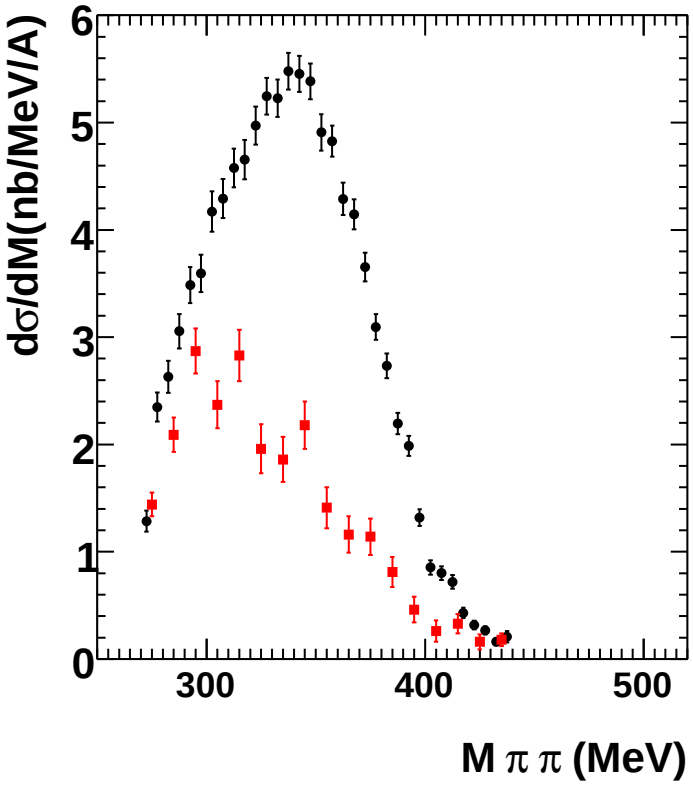

Figure 88: Mass differential cross section of the $\pi^0\pi^0$ channel for incident photon energies from 400 to 500 MeV.
The black dots show the cross section per nucleon on Deuterium, the red squares represent the cross section per nucleon for Calcium, taken from [Blo07]. See text for details.

6.1.2. Cross section of the $\pi^{\pm}\pi^{0}$ channel

As in the $\pi^{0}\pi^{0}$ channel, the mass differential cross section per nucleon of the $\pi^{\pm}\pi^{0}$ system on Deuterium was calculated using equation 53, the result is shown in figure 89. Since there are no reliable data of the mass differential cross section on the proton for this channel, and also the direct determination of the cross section on the neutron was not possible, the cross section on the neutron could not be determined. Table 18 in Appendix A.11 shows the numerical values of the cross section in the $\pi^{\pm}\pi^{0}$ channel on Deuterium.

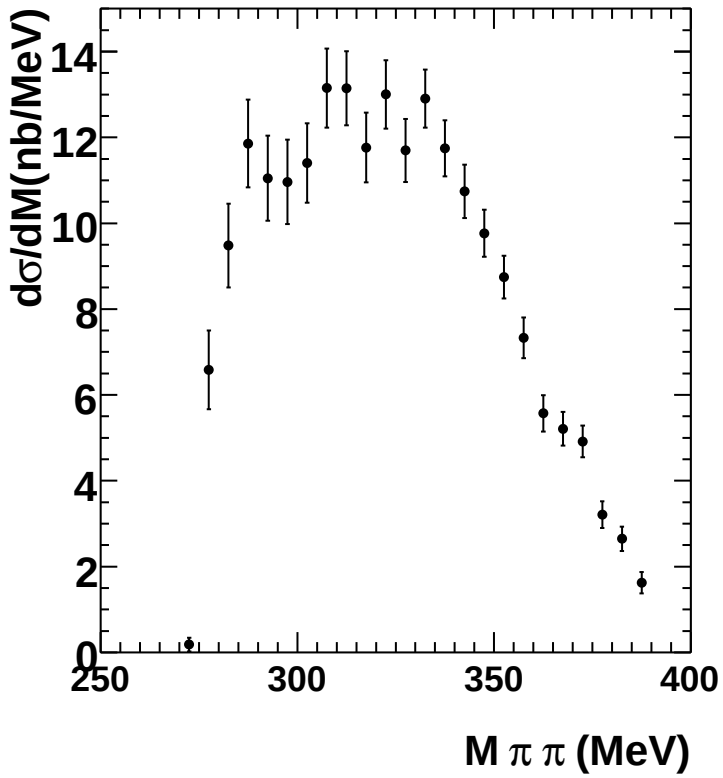

Figure 89: Mass differential cross section of the $\pi^{\pm}\pi^{0}$ channel for incident photon energies from 400 to 460 MeV.

The mass differential cross section per nucleon of the $\pi^{\pm}\pi^{0}$ channel on Deuterium for incident photon energies from 400 to 500 MeV is shown in 90 (black dots). Also plotted is the cross section per nucleon on Calcium (red squares), taken from [Blo07].

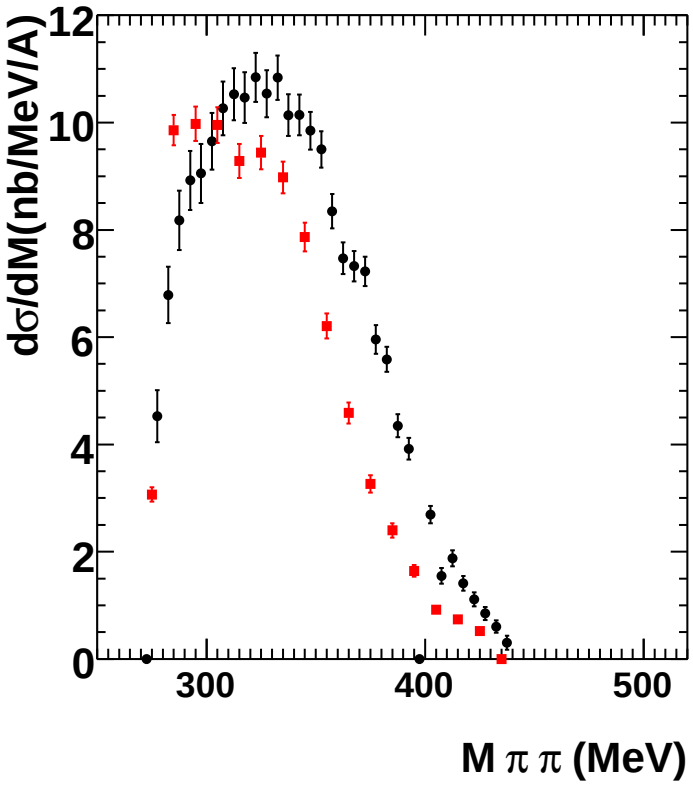

Figure 90: Mass differential cross section of the $\pi^{\pm}\pi^{0}$ channel for incident photon energies from 400 to 500 MeV.
The black dots show the cross section per nucleon on Deuterium, the red squares represent the cross section per nucleon for Calcium, taken from [Blo07]. See text for details.

6.2. Determination of the total cross section on liquid Deuterium

The total cross sections of the $\pi\pi$ channels were determined in the following way:
The analysis was performed as described in section 4 with some modifications which are described in this chapter.
To determine the total cross section in the range of 400 to 550 MeV incident photon energy, this energy range was sliced for the ongoing analysis. On the one hand, as many data points as possible should be obtained, on the other hand, enough statistics had to be collected per energy bin. The incident photon energy spectrum was restricted to 30 MeV wide bins from 400 to 430 MeV, 430 MeV to 460 MeV, 460 MeV to 490 MeV, 490 to 520 MeV and 520 to 550 MeV. A separate analysis was started per photon energy bin. Because higher incident photon energies were allowed in the analysis, the number of the 5 MeV wide $m_{\gamma\gamma}$ spectra (see figure 64) had to bee increased. So, instead of having 24 spectra from 275 to 395 MeV, 48 spectra from 275 to 515 MeV were filled, keeping the fitting procedure unchanged as described in section 4. Beside the modifications in the analysis code, also the simulation was adapted in the same way.

6.2.1. Total cross section of the $\pi^0\pi^0$ channel

The mass differential cross section of the $\pi^0\pi^0$-channel on Deuterium was determined for the incident photon energies from 400 to 430 MeV, 430 MeV to 460 MeV, 460 MeV to 490 MeV, 490 to 520 MeV and 520 to 550 MeV as shown in figure 91.

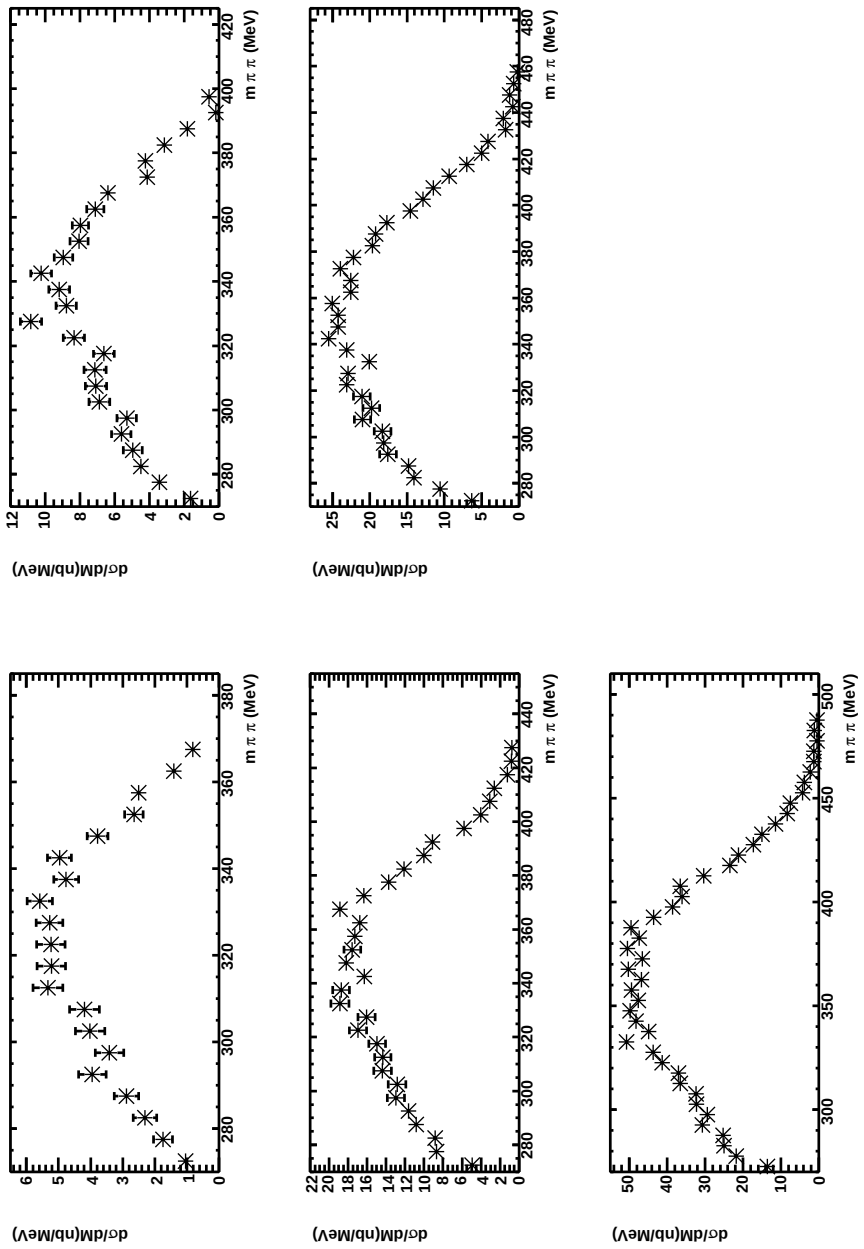

Figure 91: Mass differential cross section of the $\pi^0\pi^0$ channel in 30 MeV bins from 400 to 550 MeV.

The mass differential cross sections were integrated, leading to the total cross section which is shown in figure 92 (red squares). The total cross sections on the deuteron from the TAPS@MAMI experiment 1995/1996 (Kleber, [Kle99], blue triangles), TAPS@ELSA (Jaegle, [Jae07], magenta dots) and the model of the Giessen Theory group (Buss, [Bus07], black stars) are shown for comparison. There is good agreement. In table 19, the extracted total cross section on deuterium for the $\pi^0\pi^0$ and $\pi^\pm\pi^0$ are given.

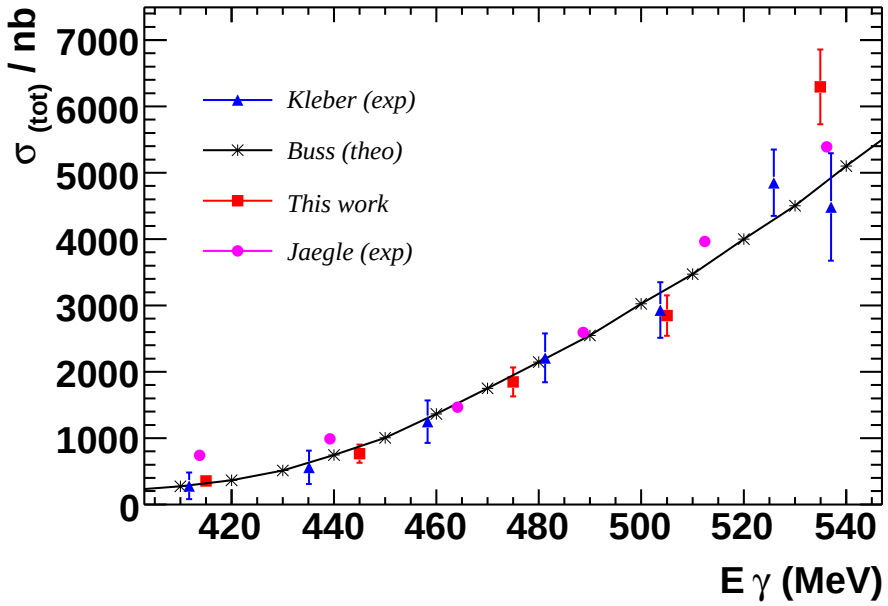

Figure 92: Total cross section of the $\pi^0\pi^0$ channel from 400 to 550 MeV incident photon energy.
See text for details.

6.2.2. Total cross section of the $\pi^\pm\pi^0$ channel

The mass differential cross section of the $\pi^\pm\pi^0$-channel on Deuterium was determined for the incident photon energies from 400 to 430 MeV, 430 MeV to 460 MeV, 460 MeV to 490 MeV, 490 to 520 MeV and 520 to 550 MeV as shown in figure 93.

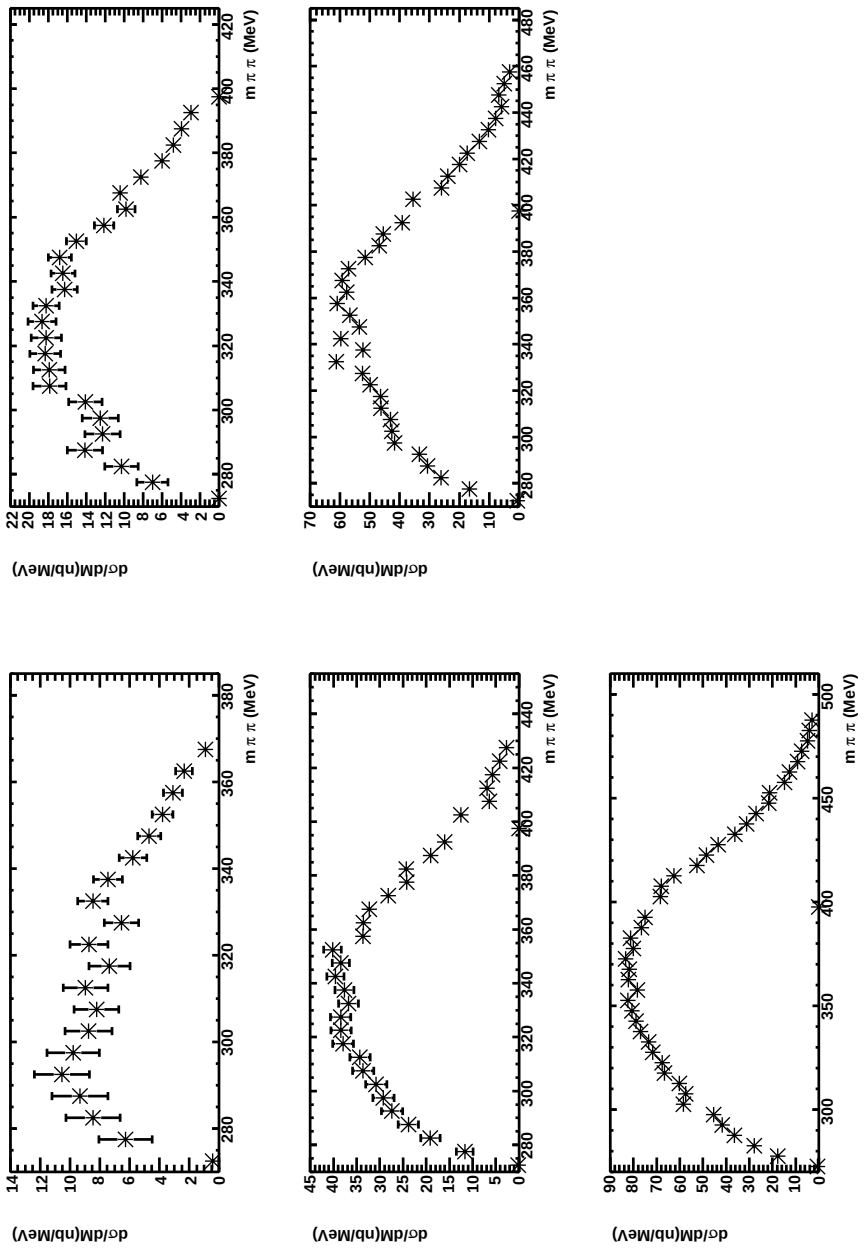

Figure 93: Mass differential cross section of the $\pi^{\pm}\pi^{0}$ channel in 30 MeV bins from 400 to 550 MeV.

The mass differential cross sections were integrated, leading to the total cross section which is shown in figure 94 (red squares). Also shown is the total cross section on deuterium for the channel $\gamma p \rightarrow \pi^+\pi^0 n$ (black points, [Ahr07]) and $\gamma n \rightarrow \pi^-\pi^0 p$ (black circles, [Zab97], [Ped07]) measured by the DAPHNE@MAMI experiment. The total cross section on the proton (Langgärtner, [Lan99], green squares) and the theoretical calculations of Buss ([Bus07], blue triangles) are shown as well. In table 19, the extracted total cross section on deuterium for the $\pi^0\pi^0$ and $\pi^\pm\pi^0$ are given.

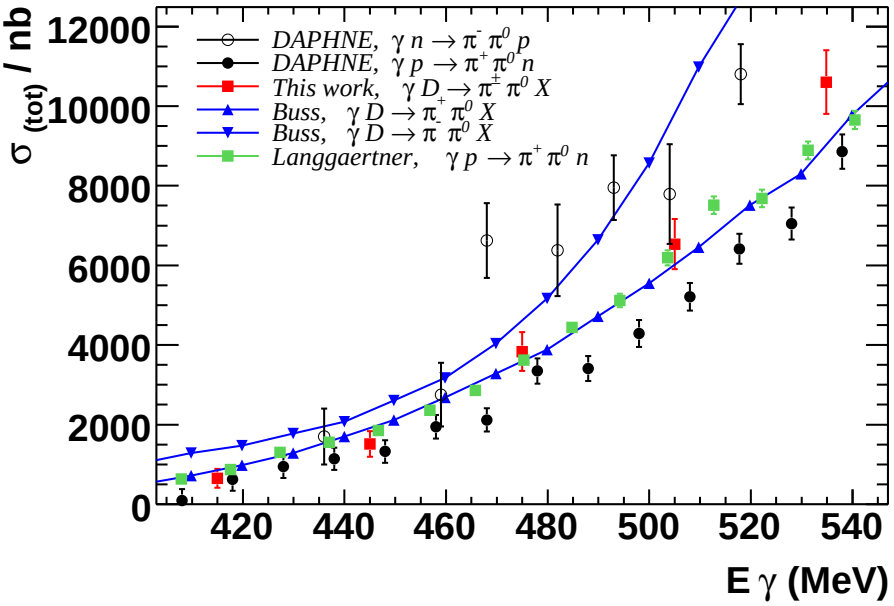

Figure 94: Total cross section of the $\pi^\pm\pi^0$ channel from 400 to 550 MeV incident photon energy.
See text for details.

6.3. Interpretation and outlook

6.3.1. Mass differential cross sections

The mass differential cross section of the $\pi^0\pi^0$-channel on the deuteron has been extracted and therefrom, by subtracting the differential cross section on the proton, the mass differential cross section of the neutron was derived. This cross section is very essential, because in theoretical calculations, it was assumed that the cross section on the proton and on the neutron are identical. This is not the case. The cross section on the neutron shows a relative shift of strength towards lower $m_{\pi\pi}$ in comparison to the cross section on the proton. To illustrate this, figure 95 shows the ratio of the cross section on the proton divided by the cross section on the neutron. With the cross section on the neutron available, refined transport calculations should be performed. With this modification in the BUU code, a recalculation of the mass differential cross section in the model and a comparison of the output with the cross sections given in [Gre07], will give an answer to the question whether the observed shift in the $\pi\pi$ mass is an effect of final state interactions, or if this is, as published, an effect of partial restoration of the chiral symmetry.

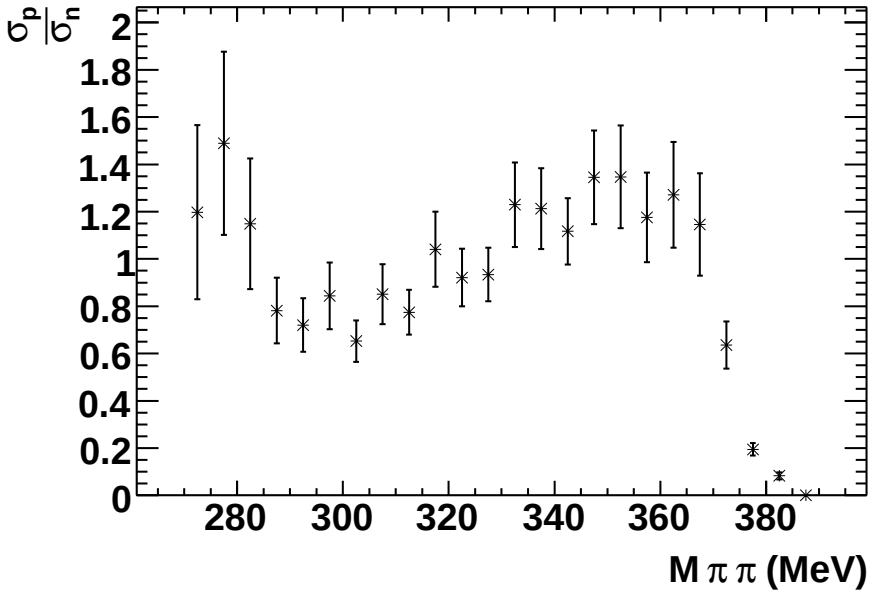

Figure 95: Ratio of $\frac{\sigma_p}{\sigma_n}$ on Deuterium in the $\pi^0\pi^0$ channel from 400 to 460 MeV incident photon energy.

6.3.2. Total cross sections

The total cross section in the $\pi^0\pi^0$-channel on the deuteron was determined and is in good agreement with the published data for low incident photon energies. At high incident photon energies, the total cross section was determined to be higher than in the previous experiment. As the total cross section of the BUU model was derived from the previous experiment, also here small modifications could be done in order to reach the data points from this work.

Also the total cross section in the $\pi^{\pm}\pi^0$-channel was measured. As in our setup no magnetic field was available, it was not possible to distinguish between π^+ and π^-. The cross section for the reaction $\gamma D \rightarrow \pi^{\pm}\pi^0 X$ should be the sum of the reactions $\gamma p \rightarrow \pi^+\pi^0 n$ and $\gamma n \rightarrow \pi^-\pi^0 p$. Comparing the cross section on Deuterium to that on Hydrogen, the cross section on Deuterium seems to be very low. This result is not yet understood.

References

[Ann97] J. R. M. Annand, I. Anthony, A. H. Sibbald, K. Livingston; *ACQU Data acquisition system for nuclear physics, 3rd Edition*; University of Glasgow, 1997

[Ann01] J. R. M. Annand; *Big Bite Trigger Specification and Costing*; University of Glasgow, 2001

[Ann05] J. R. M. Annand; *Data analysis within an AcquRoot Framework*; University of Glasgow, 2005

[Ant91] I. Anthony, J.D. Kelly, S.J. Hall, G.J. Miller und J.Ahrens; *Design of a tagged photon spectrometer for use with the Mainz 840 MeV microtron*; Nucl. Instr. and Meth. A310 (1991) 230

[Ahr94] J. Ahrens et al.; *The Mainz Microtron MAMI: A Facility Portrait with a Glimse at First Results*; Nuclear Physics News Europe 4 (1994)

[Ahr05] J. Ahrens; *private communication*; 2005

[Ahr07] J. Ahrens et al.; ; Phys. Lett. B 551, 49 (2003)

[Ber87] V. Bernard, U.-G.Meißner und I.Zahed; ; Phys. Rev. Lett. 59 (1987) 966

[Blo07] F. Bloch; *Double pion photoproduction off* ^{40}Ca; Eur.Phys. J. A 32, 219 (2007)

[Bon96] F. Bonutti; Phys. Rev. Lett. 77 (1996) 603

[Boi07] B. Boillat; *Doktorarbeit in Vorbereitung*; Universität Basel, 2007

[Bro91] G. E. Brown and M. Rho; *Scaling effective Lagrangians in a dense medium*; Phys. Rev. Lett. 66 2720 (1991)

[Bru05] R. Brun and F. Rademakers et al; *ROOT User's Guide 4.04*; CERN 2005

[Bru07] J. Brudvik: *Doktorarbeit in Vorbereitung*; UCLA Los Angeles, 2007

[Bus06] O. Buss, L. Alvarez-Ruso, P. Mühlich and U. Mosel; *Low-energy pions in nuclear matter and pi pi photoproduction within a BUU transport model*; Eur. Phys. J. A 29 (2), 189 (2006)

[Bus07] O. Buss: *Doktorarbeit in Vorbereitung*; Universität Gießen, 2007

[Cha76] Y. Chan et al.; *Design and Performance of a Modularized NaI(Tl) Detector*; IEEE Article, 1977

[Cod07] R. Codling; *Doktorarbeit in Vorbereitung*; University of Glasgow, 2007

[CERN] *http://www.cern.ch*

[GEA94] Application and Software Group, Computing and Network Division; *Geant Detector Description and Simulation Tool*, CERN, 1994

[Cla05] M. Clajus; *Crystal Ball Note CB-97-004*; UCLA Los Angeles, 1997

[Dow03] E. Downie; *The Magnetic Moment of the θ^+, First Year PhD report*; University of Glasgow, 2003

[Dow06] E. Downie; *Radiative π^0 photoproduction in the region of the $\Delta(1232)$ resonance*; Doktorarbeit, University of Glasgow, 2006

[Dow07] E. Downie; *private communication*

[Dre04] P. Drexler; *Entwicklung und Aufbau der neuen TAPS-Elektronik*; Doktorarbeit, Universität Gießen, 2004

[Dre06] P. Drexler; *private communication*

[Ehm00] A.Ehmanns; *Entwicklung, Aufbau und Test eines neuen Auslesesystems für den Crystal-Barrel-Detektor zur Messung photoinduzierter Reaktionen an ELSA*; Universität Bonn, 2000

[Gab94] A. R. Gabler et al.; *Response of TAPS to monochromatic photons with energies between 45 and 790 MeV*; Nucl. Instr. and Meth. in Phys. Res. A 346 (1994) 168-176

[Gre07] R. Gregor; *Modifikation von Pionenpaaren in Kernmaterie*; Doktorarbeit, Universität Gießen, 2007

[GSI] *http://www.gsi.de*

[Hal96] S. J. Hall et al.; Nucl. Inst. and Meth. in Phys. Res. A368 (1996) 698-708

[Hat92] T. Hatsuda and S. H. Lee; *QCD sum rules for vectro mesons in the nuclear medium*; Phys. Rev. C 46 R34 (1992)

[Hat99] T. Hatsuda and S. H. Lee; Phys. Rev. Lett. 82 2840 (1999)

[Hej98] V. Hejny; *Photoproduktion von η-Mesonen and Helium 4*; Doktorarbeit, Universität Gießen, 1998

[Hof57] R. Hofstadter; Ann Rev Nucl Sci 7 (1957) 231

[Jae07] I. Jaegle; *$\pi^0\pi^0$, η and η' photoproduction off the deuteron*; Vortrag, Milos, 2007

[Jan00] S. Janssen et al.: *The new charged-particle VETO detector for the photon spectrometer TAPS*; IEEE Trans. Nucl.Sci., vol. 47, no. 3, Juni 2000

[Jan05] A. Jankowniak; Lecture *Recirculating Electron Accelerators*; sutdent's workshop on electromagnetic interactions; Bosen, 2005

[Jid00] D. Jido, T. Hatsuda, T. Kunihiro; Phys. Rev. Lett. 84 3252 (2000).

[Kash06] V. Kashevarov; *private communication*; 2006

[Kle99] V. Kleber; *QuasifreieDoppe-π^0-Photoproduktion am Deuteron*; Diplomarbeit, Universität Giessen, 1999

[Kli90] S. Klimt, M. Lutz und W. Weise; *Chiral Phase Transition In The SU(3) Nambu And Jona-Lasinio Model*; Phys. Lett. B 249 (1990)

[Koc02] V. Koch; *Introduction to Chiral Symmetry*; http://theory.gsi.de/ knoll/lecture-VKoch.html GSI, 2002

[Kot01] M. Kotulla; *Experiment zur Bestimmung des magnetischen Moments der* $\Delta^+(1232)$ *Resonanz*; Doktorarbeit, Universität Gießen, 2001

[Kot04] M. Kotulla; *private communication*; 2004

[Kot07] M. Kotulla; *private communication*; 2007

[Kra07] D. Krambrich; *Aufbau des Crystal Ball-Detektorsystems und Untersuchung der Helizitätsasymmetrie in* $\gamma p \to p\pi^0\pi^0$; Doktorarbeit, Universität Mainz, 2007

[Kru95] B. Krusche; *Photoproduction of* π^0 *and* η *mesons from nucleons and nuclei in the second resonance region*; Universität Gießen, 1995

[Kru06] B. Krusche and S. Schadmand: *Study of Non-Strange Baryon Resonances with Meson Photoproduction*; nucl-ex/0306023 v1, 2003

[Kru07] B. Krusche; *private communication*; 2007

[Lag03] Y. Assafari et al; *Double* π^0 *Phootoproduction on the Proton at GRAAL*; Phys. Rev. Lett. 90 (2003) 222001

[Lag96] L. Murphy, J. M. Laget; CEA Report No DAPHNIA 96-10; Sacklay, 1996

[Lan99] W. Langgärtner; *Doppel-Pion-Photoproduktion am Proton*; Diplomarbeit Universität Gießen, 1999

[Leu07] S. K. Leupold; *Lecture on theoretical hadron physics*; Universität Gießen, 2007

[Leu07a] S. K. Leupold; *private communication*; 2007

[Mar98] A. Martin et al.; *Detection of charged pions and protons in the segmented electromagnetic calorimeter TAPS*; Nucl. Instr. and Methods in Phys. Res. A417 (1998) 137-149

[Mes02] J. G. Messchendorp, S. Janssen, M. Kotulla et al.; Phys. Rev. Lett. 89 (2002) 222302

[Mol92] K. Molenaar; *Performance of TAPS in the Tagged Photon Beam of MAMI*; Rijksuniversiteit Groningen 1992

[Nef95] B. M. K. Nefkens; *The Crystal Ball - Overview*; Crystal Ball Report 95-1, 1995

[Nik06] A. Nikolaev; *Tagging efficiency measurement*; Vortrag, 09.06.2005

[Nov91] R. Novotny et al.; *The BaF Photon Spectrometer TAPS*; IEEE Transactions on Nuclear Science, Vol 38, 1991

[PDG04] PDG - Particle Data Group; *Particle Physics Booklet*; American Institute of Physics (2004)

[PDG06] PDG - Particle Data Group; *Particle Physics Booklet*; American Institute of Physics (2006)

[Ped07] P. Pedroni; *private communication*; 2007

[Pfe98] M. Pfeiffer; *Ansprechverhalten von BaF2 Szintillationsdetektoren fÃ¼r niederund hochenergetische Photonen*; Diplomarbeit, Universität Giessen, 1998

[Rei99] A. Reiter; *Entwicklung und Test eines ortsauflösenden Detektors für die Photonenmarkierungsanlage*; Universität Mainz, 1999

[Roc05] L. Roca; *Helicity asymmetries in double pion photoproduction on the proton*; Nucl. Phys., A748 192, (2005)

[Röb91] M. Röbig; *Eichung des TAPS-Detektorsystems mit Höhenstrahlung*; Universität Gießen, 1991

[Röh01] Röhm GmbH & Co. KG: Rohacell 71 FX, EG-Sicherheitsdatenblatt, 2001

[Sch99] C. Schmidt: *Optimierung des Datenakquisitions-Systems des CRYSTAL-BARREL-Experiments an ELSA*; Universität Bonn, 1999

[Sch06] S. Schumann: *Doktorarbeit in Vorbereitung*; Universität Bonn, 2006

[Sch07] S. Schumann; *private communication*; 2007

[Smc94] *http://home.fnal.gov/ bugel/smc.gif*

[Sta00] A. Starostin et al.; Phys. Rrev. Lett. 85 (2000) 5539

[TAGG] *http://wwwa2.kph.uni-mainz.de/tagcal/online/*

[Tho04] A. Thomas; *Crystal Ball Hydrogen (Deuterium) Target Manual*; Vortrag, Universität Mainz, 24.06.2004.

[Tho07] A. Thomas; *private communication*; 2007

[Trn06] D. Trnka; *Investigation of in-medium modifications of the ω meson in photonuclear reactions*; Universität Gießen, 2006

[Unv04] M. Unverzagt; *Energieeichung des Crystal Ball Detektors am MAMI*; Universität Mainz, 2004

[War97] S. Wartenberg; *Die Strahlasymmetrie in der Deuteron-Photospaltung im Bereich von 160 bis 410 MeV*; Universität Mainz, 1997

[Wei92] M. Lutz, S. Klimt, W. Weise; ; Nucl. Phys. A 542 52 (1992)

[Zab97] A. Zabrodin et al.; ; Phys. Rev. C 55, R1617 (1997)

[Zeh07] F. Zehr; *Doktorarbeit in Vorbereitung*; Universität Basel, 2007

A. Appendix

A.1. talk2server

Program to communicate to TapsServer without X-Window

Syntax:
`talk2server [command] [channel] [value] [store]`

Example: to set the CFD-th of channel 347 to - 427 mV:
`talk2server 31 347 -427 0`

to shutdown the complete Slowcontrol `talk2server 100`

DEST	READ	SET	UPLOAD	INIT
QAC-LG	10	11	12	13
QAC-LGS	15	16	17	18
QAC-SG	20	21	22	23
QAC-SGS	25	26	27	28
CFD	30	31	32	33
LED-L	40	41	42	43
LED-H	45	46	47	48
BOARD	52	53	54	
V-SET	60	61	62	63
V-OFF	65	66	67	68
HV-BAF	70	71	72	73
HV-VETO	75	76	77	78
CFD VETO	80	81	82	83

PING 1 Used to check whether server is alive
TEST_QAC 5 Test QAC's and write Pedestals to DB
IP_UPLOAD 50 Uploads all the IP hostnames of the HardWareServers
END 100 End the server with this command

channel = number of Crystal
value = value to be set (neg. for discriminators, pos. for HV, V#, QAC#)
store = write value to database (0=no, 1=yes)

Also used as return values for the TATUI program:

errortype =	-1 = OK
	-2 = error in MySQL
	-3 = error in TapsServer
	-4 = error in HardwareServer
	-5 = error in HVServer
olddbvalue	= value has been stored before
oldhwvalue	= not implemented, always returning 0
newdbvalue	= value that has been stored
newhwvalue	= not implemented, always returning 0

A.2. hvtalk

Hvtalk is a program which was written by Michael Lang to access the LeCroy 1440 HV mainframe via the serial bus of a computer, which I modified. In comparison to the AD/CAM, no CAMAC interface and no CNAF commands have to be used. The commands which are shown below can be typed using the computers' keyboard which is a big improvement in comparison to use the handheld controller for two reasons. The controller has to be used locally, which does not allow to change the HV when the experimental area is closed. Furthermore, due to the keyboard layout of the handheld contoller it is very complicated and not intuitive at all, to type the right commands.
The most important commands are:

COMMAND	Function
M	Specifies the LeCroy mainframe
ST	Reports the status of the desired mainframe
ON	Switches on the mainframe
OFF	Switches off the mainframe
C	Specify channel
R	Read HV of the ”actual” buffer of the channel
E	Everything - ”actual”, ”demand” and ”backup” buffers
A	The value for all 256 channels is given out
W	Write voltage to the ”actual” buffer of the channel
DO	Do for number of channels specified
CO	Copy ”demand” into ”backup” buffer
U	Update ”demand” = ”demand” + ”backup” - ”actual” buffer
N	Report not updated channels
	The combined commands look the following:
M1 ST	Print status of mainframe 1
M2 ON	Switch on Mainframe 2
C1 W-1000	Write -1000 V to channel 1
C30 R DO 10	Read ”actual” buffers of channels 30 to 40
R E A	Read everything from all channels
CO U N	Copy ”demand” to ”backup”, update and show not updated channels

A.3. SetMCU

SetMCU is a program to set registers on the VME hardware. To mask e.g. the inner rings from the trigger, shell scripts are used. To switch on all channels for the trigger, the following script was used (this is the sequence for one MCU module):

	VME base address	VME sub address	value	action
./mcu/setMCU	0x10000000	0x00	0xffff	LED1 01-16 on
./mcu/setMCU	0x10000000	0x02	0xffff	LED1 17-32 on
./mcu/setMCU	0x10000000	0x04	0xffff	LED1 33-48 on
./mcu/setMCU	0x10000000	0x06	0xffff	LED1 49-64 on
./mcu/setMCU	0x10000000	0x08	0xffff	LED2 01-16 on
./mcu/setMCU	0x10000000	0x0a	0xffff	LED2 17-32 on
./mcu/setMCU	0x10000000	0x0c	0xffff	LED2 33-48 on
./mcu/setMCU	0x10000000	0x0e	0xffff	LED2 49-64 on
./mcu/setMCU	0x10000000	0x10	0xffff	VETO 01-16 on
./mcu/setMCU	0x10000000	0x12	0xffff	VETO 17-32 on
./mcu/setMCU	0x10000000	0x14	0xffff	VETO 33-48 on
./mcu/setMCU	0x10000000	0x16	0xffff	VETO 49-64 on
./mcu/setMCU	0x10000000	0x18	0x0001	external trigger
./mcu/setMCU	0x10000000	0x20	0x1fff	minimum delay

The first hex value is the VME base address, the second the VME sub address and the third is the value to be written. Details can be found in the MCU manual.

As an example, it is shown, how to mask channel 7 for LED2:

Channel	16	15	14	13	12	11	10	9	8	7	6	5	4	3	2	1
On/Off	1	1	1	1	1	1	1	1	1	0	1	1	1	1	1	1
Hex	f				f				b				f			

The script has to be modified the following:

```
./mcu/setMCU 0x10000000 0x08 0xffbf
```

A.4. Changing NTEC boards

If you detect any broken Channel in the Spectra/Pattern do the following very carefully:

1. Check the HV-Settings using TATUI
2. Check the Discriminator-Settings (also with TATUI)

If there was no error at all, you have to change the red CAEN-Board (MB) the following way:

1. Turn off the crate

2. Uncable the CAEN-Board
3. Unmount the Daisy-Chain-ECL-Cable (”CONTROL-Connector”) completely
4. Open top- & bottom-Screws
5. Take out the board by pushing the top-clamp upwards and simultaneously the bottom-clamp downwards
6. Put the board on a table, the backplane connectors showing to you
7. Take out the screw and the brass-cylinder between MB and PB on the right upper side
8. Separate MB and PB by pushing your thumbs onto the outside-edges of the backplane-connectors and reaching with your forefingers under the PB in order to lift it up
9. Check the rotary-switches on the MB
10. Take a new readout-moduleand unmount PB like mentioned above
11. Set the rotary-switches on the new MB the way it was on the old MB (If you don’t remember the number, the first board in the crate starts with 20 and the last ends with 2F)
12. Set the red termination-jumper (upper left side) exactly the way they were set on the old MB (The Termination has to be open for all except the last board)
13. Mount the PB on the MB
14. Put back the brass-cylinder and the screw (extremely important: If not done, the board may overheat and components may burn)
15. Put the new readout-module in the VME-slot (push top-clamp downwards and bottom-clamp upwards until the board is in with the others)
16. Mount the CONTROL-Connector
17. Cable the trigger-output
18. Fasten the screws again
19. Switch on crate
20. Switch on Testpulser
21. When the computer is up start the HardwareServer with the command `./HardwareServer -testqac #` (where # = boardnumber in crate)
22. After having finished the QAC-Setup, enter Y for saving the values to the Database
23. Cable the Detector-signal-cables
24. Continue with measurement

A.5. switching on the system

Starting the Slowcontrol:

1. Boot taps01
2. Make sure that TapsServer (TS) is running in the background (use ps aux to view processes)
3. Start Syscontrol in with the command `/home/sc/diag-tools/syscontrol &`
4. Switch on the VME-crates one by one and watch the syscontrol carefully
5. When all VME-computers are up, login by entering v1, v2, ..., (one by one)
6. Start the HardwareServers (HWS) to initialize the CAEN-Boards `/bin/HardwareServer -v 3`
7. After a successful Init, kill the HWS with CTRL+C If you don't, the readout-mode won't work!!!
8. Login on v9
9. Start the HVServer (HVS) `/tmp/slowcontrol/bin/HVServer -v 3` That one you don't have to kill :-)
10. Login on the MCU-computers (v9, v10)
11. Go to the taps folder (cd /taps)
12. Run `./start_mcu`
13. Watch the scaler in the NIM-trigger-crate The cosmic-range should be between 10 and 20 Hz

If the computers are already on, skip 1), 3), 4) ;-)

A.6. TapsServer

- Is running on Server-1
- Autostart-Routine (always on when system starts)
- Main Program to communicate with MySQL-Database, the User-Clients and the HardwareServers
- If one has to kill, type `killall -9 TapsServer` (the binary can be found in `/sqldata/slowcontrol/bin`)

The Program can be started with the following options:

-?	This message
-v <level>	Verbosity level (default=0, max = 3)
	How detailed shall the report/error messages be that given out?
-t <thrds>	Number of threads (default=10)
-q <queue>	Maximum size of queue (default=10)
-h <host>	Hostname of SQL-Server (default=localhost)
	Fixed, DON'T change!
-u <user>	Username of SQL-Server (default=taps)
	Fixed, DON'T change!
-p <passw>	Password for SQL-Server (default=taps2003)
	Fixed, DON'T change!
-d <dbase>	Database-Name (default=taps)
	Fixed, DON'T change!

If the TS was started with the script `/etc/init.d/tapsserver start`, there is a logfile in `/home/sc/log/tapsserver.log`
Otherwise it would be good to start this way:
`./TapsServer -v 3 > TS-yyyymmdd-hhmm.log`

A.7. HardwareServer

- running on VME1 - VME8
- Client to set/write thresholds/pedestals on CAEN-Boards/Piggybacks

-?	This message
-v <level>	Verbosity level (default=0, max = 3)
	How detailed shall the report/error messages be that are given out?
-t <thrds>	Number of threads (default=10)
-q <queue>	Maximum size of queue (default=10)
-s <host>	Hostname of SQL-Server (default=localhost)
	Fixed, DON'T change!
-testqac <b-nr>	Testing QAC's, get Pedestals with option to write to SQL-DB.
	This Option tests the QAC's and adjusts the pedestals to channel 105.
	These values can be written directly into the SQL-Database.
	Afterwards, the program finishes.
	To change some values, the HWS has to be restarted!
	The Boardnumber is the Number of the Board in the VME-Crate.
	For this option only the digital-testpulser is needed.
-noinit	Starts the Hardwareserver without Initialization of the boards.
	Skips the initialization of the boards.
-initonly	Initialization of the boards and finish the HWS.
	Specially to switch directly to the readout-mode after initialization.

A.8. Network cable plan

To ensure that the data from the readout boards can be transported fast to the event builder, the second network interface of the VME CPU was connected via a 100MBit uplink to another optical Gigabit Ethernet switch. The system was designed so that all communication between server and clients, that is any traffic except for data-transport is realized using the first network connector (eth0) and only experiment-data are sent on the second one (eth1). Therefore two strict separated private network systems were realized having the following properties:

Table 15: Network plan

Computer	eth0	eth1	comment
server1	192.168.1.100	A2 network	sql- & bootserver
server2	192.168.2.100	A2 network	data server
switch 1	192.168.1.101	—	boot-switch
switch 2	192.168.2.101	—	data-switch
VME 1	192.168.1.1	192.168.2.1	block A
VME 2	192.168.1.2	192.168.2.2	block B
VME 3	192.168.1.3	192.168.2.3	block C
VME 4	192.168.1.4	192.168.2.4	block D
VME 5	192.168.1.5	192.168.2.5	block E
VME 6	192.168.1.6	192.168.2.6	block F
VME 7	192.168.1.7	192.168.2.7	block G
VME 8	192.168.1.8	192.168.2.8	block H
VME 9	192.168.1.9	192.168.2.9	MCU ABGH, HV- & CAMAC-interface
VME 10	192.168.1.10	192.168.2.10	MCU CDEF
VME 11	192.168.1.11	192.168.2.11	spare
VME 12	192.168.1.12	192.168.2.12	spare

A.9. Tagger Calibration

Main beam (TOTAL) energy = 882.3383 MeV, Main beam momentum = 882.3381 MeV/c.
NMR reading = 1.0483700 (Equivalent uniform field = 1.0511167 Tesla)

tagger channel	E_γ / MeV	E_e / MeV	tagger channel	E_e / MeV	E_γ / MeV
1	818.351990	63.986282	2	817.158936	65.179314
3	815.916748	66.421509	4	814.625122	67.713150
5	813.284180	69.054085	6	811.892883	70.445358
7	810.448547	71.889709	8	808.951477	73.386772
9	807.404297	74.933945	10	805.807495	76.530777
11	804.163452	78.174805	12	802.475220	79.863052

tagger channel	E_γ / MeV	E_e / MeV	tagger channel	E_e / MeV	E_γ / MeV
13	800.744690	81.593552	14	798.975586	83.362656
15	797.172363	85.165863	16	795.338135	87.000130
17	793.477966	88.860283	18	791.597839	90.740433
19	789.701294	92.636948	20	787.794922	94.543350
21	785.885071	96.453171	22	783.977356	98.360886
23	782.078369	100.259872	24	780.194214	102.144028
25	778.330078	104.008194	26	776.490112	105.848129
27	774.678528	107.659714	28	772.897583	109.440697
29	771.148193	111.190041	30	769.429932	112.908325
31	767.739746	114.598480	32	766.074219	116.264053
33	764.428040	117.910217	34	762.794617	119.543655
35	761.166931	121.171341	36	759.537109	122.801132
37	757.897217	124.441055	38	756.244934	126.093323
39	754.584106	127.754181	40	752.917908	129.420349
41	751.246826	131.091446	42	749.570190	132.768066
43	747.887085	134.451172	44	746.198120	136.140167
45	744.504150	137.834106	46	742.804077	139.534149
47	741.098328	141.239944	48	739.386597	142.951630
49	737.668091	144.670151	50	735.943726	146.394562
51	734.213013	148.125214	52	732.476624	149.861618
53	730.734497	151.603775	54	728.985474	153.352753
55	727.230225	155.108002	56	725.468872	156.869354
57	723.701416	158.636810	58	721.927490	160.410751
59	720.147095	162.191162	60	718.360474	163.977814
61	716.567322	165.770935	62	714.767883	167.570389
63	712.962158	169.376099	64	711.149963	171.188293
65	709.331299	173.006943	66	707.506226	174.832062
67	705.674744	176.663513	68	703.837036	178.501221
69	701.993042	180.345184	70	700.142639	182.195618
71	698.285522	184.052734	72	696.422302	185.915955
73	694.552490	187.785797	74	692.676147	189.662125
75	690.793457	191.544769	76	688.904724	193.433533
77	687.009705	195.328552	78	685.107910	197.230377
79	683.199951	199.138336	80	681.285522	201.052765
81	679.364807	202.973434	82	677.437988	204.900238
83	675.504883	206.833344	84	673.565796	208.772491
85	671.620117	210.718109	86	669.668213	212.670044
87	667.710327	214.627899	88	665.746094	216.592194
89	663.775269	218.562973	90	661.798584	220.539642
91	659.816040	222.522217	92	657.827393	224.510880
93	655.832214	226.506027	94	653.831177	228.507050
95	651.824280	230.513962	96	649.811035	232.527222

tagger channel	E_γ / MeV	E_e / MeV	tagger channel	E_e / MeV	E_γ / MeV
97	647.791870	234.546356	98	645.767090	236.571167
99	643.736328	238.601944	100	641.699646	240.638611
101	639.657349	242.680939	102	637.608887	244.729385
103	635.554321	246.783936	104	633.494263	248.844025
105	631.428467	250.909760	106	629.356812	252.981415
107	627.279785	255.058441	108	625.196899	257.141357
109	623.108337	259.229919	110	621.014038	261.324219
111	618.914185	263.424103	112	616.809326	265.528900
113	614.698425	267.639832	114	612.581970	269.756287
115	610.460571	271.877655	116	608.333557	274.004700
117	606.200989	276.137268	118	604.062866	278.275360
119	601.919861	280.418396	120	599.771606	282.566650
121	597.618225	284.720032	122	595.459900	286.878357
123	593.296265	289.041992	124	591.127319	291.210907
125	588.953125	293.385132	126	586.773682	295.564545
127	584.589478	297.748749	128	582.400696	299.937561
129	580.206848	302.131409	130	578.007996	304.330261
131	575.804382	306.533875	132	573.596008	308.742249
133	571.383057	310.955170	134	569.164978	313.173279
135	566.942139	315.396088	136	564.714783	317.623474
137	562.482788	319.855469	138	560.246460	322.091797
139	558.005737	324.332520	140	555.760498	326.577789
141	553.510376	328.827881	142	551.255859	331.082367
143	548.997314	333.340942	144	546.734741	335.603546
145	544.467285	337.870972	146	542.195557	340.142731
147	539.919983	342.418274	148	537.640259	344.697998
149	535.356262	346.981995	150	533.068176	349.270081
151	530.776062	351.562195	152	528.480042	353.858215
153	526.180298	356.157959	154	523.876709	358.461517
155	521.568848	360.769409	156	519.257080	363.081177
157	516.941895	365.396332	158	514.622986	367.715271
159	512.300171	370.038086	160	509.973572	372.364685
161	507.643555	374.694702	162	505.310150	377.028107
163	502.973328	379.364929	164	500.632965	381.705292
165	498.289185	384.049072	166	495.941895	386.396362
167	493.590942	388.747314	168	491.236694	391.101562
169	488.879272	393.458984	170	486.519043	395.819214
171	484.155853	398.182404	172	481.789246	400.549011
173	479.419495	402.918762	174	477.046448	405.291809
175	474.670563	407.667694	176	472.292206	410.046051
177	469.910553	412.427704	178	467.526306	414.811951
179	465.139008	417.199249	180	462.748657	419.589600

tagger channel	E_γ / MeV	E_e / MeV	tagger channel	E_e / MeV	E_γ / MeV
181	460.355804	421.982452	182	457.960266	424.377991
183	455.562134	426.776123	184	453.161285	429.176971
185	450.758118	431.580139	186	448.351990	433.986267
187	445.943726	436.394531	188	443.533142	438.805115
189	441.119934	441.218323	190	438.704651	443.633606
191	436.286621	446.051636	192	433.866394	448.471863
193	431.444275	450.893982	194	429.020020	453.318237
195	426.593292	455.744965	196	424.164093	458.174164
197	421.733154	460.605103	198	419.300323	463.037933
199	416.865601	465.472656	200	414.429352	467.908905
201	411.990845	470.347412	202	409.550232	472.788025
203	407.107513	475.230743	204	404.663269	477.674988
205	402.217834	480.120422	206	399.770538	482.567719
207	397.321350	485.016907	208	394.870850	487.467407
209	392.418457	489.919800	210	389.964325	492.373932
211	387.509399	494.828857	212	385.052551	497.285706
213	382.594055	499.744202	214	380.134644	502.203613
215	377.673828	504.664429	216	375.211670	507.126587
217	372.748596	509.589661	218	370.284363	512.053894
219	367.818604	514.519653	220	365.351440	516.986816
221	362.883423	519.454834	222	360.414307	521.923950
223	357.944153	524.394104	224	355.473389	526.864868
225	353.001709	529.336548	226	350.529175	531.809082
227	348.055237	534.283020	228	345.580505	536.757751
229	343.105225	539.233032	230	340.629150	541.709106
231	338.152832	544.185425	232	335.675232	546.663025
233	333.196899	549.141357	234	330.718384	551.619873
235	328.239319	554.098938	236	325.759033	556.579224
237	323.278442	559.059814	238	320.797852	561.540405
239	318.316650	564.021606	240	315.835083	566.503174
241	313.353149	568.985107	242	310.871094	571.467163
243	308.388306	573.949951	244	305.905273	576.432983
245	303.422363	578.915894	246	300.939331	581.398926
247	298.455688	583.882568	248	295.971985	586.366272
249	293.488342	588.849915	250	291.004272	591.333984
251	288.520630	593.817627	252	286.036987	596.301270
253	283.553223	598.785034	254	281.069519	601.268738
255	278.585815	603.752441	256	276.102417	606.235840
257	273.619385	608.718872	258	271.136292	611.201965
259	268.653198	613.685059	260	266.170166	616.168091
261	263.687805	618.650452	262	261.206055	621.132202
263	258.724487	623.613770	264	256.243164	626.095093

tagger channel	E_γ / MeV	E_e / MeV	tagger channel	E_e / MeV	E_γ / MeV
265	253.761841	628.576416	266	251.281555	631.056702
267	248.801331	633.536926	268	246.321289	636.016968
269	243.842163	638.496094	270	241.363525	640.974731
271	238.885742	643.452515	272	236.408508	645.929749
273	233.931519	648.406738	274	231.455566	650.882690
275	228.980225	653.358032	276	226.505127	655.833130
277	224.030884	658.307373	278	221.558228	660.780029
279	219.086426	663.251831	280	216.614380	665.723877
281	214.143555	668.194702	282	211.673706	670.664551
283	209.204895	673.133362	284	206.736877	675.601379
285	204.269409	678.068848	286	201.802979	680.535278
287	199.337524	683.000732	288	196.873291	685.464966
289	194.410156	687.928101	290	191.948425	690.389832
291	189.487427	692.850830	292	187.027405	695.310852
293	184.568481	697.769775	294	182.110718	700.227539
295	179.654053	702.684204	296	177.198792	705.139465
297	174.744995	707.593262	298	172.292053	710.046204
299	169.840332	712.497925	300	167.390015	714.948242
301	164.940430	717.397827	302	162.492798	719.845459
303	160.046631	722.291626	304	157.601807	724.736450
305	155.157959	727.180298	306	152.715454	729.622803
307	150.274780	732.063477	308	147.835510	734.502747
309	145.397339	736.940918	310	142.960754	739.377502
311	140.526367	741.811890	312	138.093201	744.245056
313	135.661316	746.676941	314	133.230957	749.107300
315	130.802002	751.536255	316	128.375000	753.963257
317	125.949585	756.388672	318	123.525391	758.812866
319	121.103210	761.235046	320	118.682617	763.655640
321	116.263672	766.074585	322	113.846802	768.491455
323	111.431519	770.906738	324	109.017761	773.320496
325	106.605835	775.732422	326	104.195862	778.142395
327	101.787231	780.551025	328	99.380493	782.957764
329	96.975708	785.362549	330	94.572388	787.765869
331	92.171326	790.166931	332	89.772339	792.565918
333	87.374939	794.963318	334	84.979248	797.359009
335	82.585510	799.752747	336	80.193604	802.144653
337	77.803833	804.534424	338	75.415894	806.922363
339	73.029907	809.308350	340	70.646362	811.691895
341	68.264648	814.073608	342	65.884766	816.453491
343	63.506714	818.831543	344	61.130615	821.207642
345	58.756958	823.581299	346	56.385254	825.953003
347	54.015503	828.322754	348	51.647705	830.690552

tagger channel	E_γ / MeV	E_e / MeV	tagger channel	E_e / MeV	E_γ / MeV
349	49.282104	833.056152	350	46.918457	835.419800
351	44.557007	837.781250	352	42.197510	840.140747

A.10. GEANT FFCARDS

In the following all relevant settings in a ffcard are described:
AUTO 1
This option switches on automatic step size and tracking medium parameters of the tracking routine of GEANT.
FREQ 500
Shows the progress of the simulation. An output is given every 500 events.
SEED 0
Calculates a seed for the GEANT tracking routines automatically.
SMEA FALSE
This is an optional energy smearing, which is added to all energy deposits to account for the difference between the measured and simulated CB energy resolution. This option is switched off because the energy smearing is performed in the Acqu framework for TAPS and CB.
SPLT 0.0 0.0 0.0
SPLT controls the simulation of the last particle (photon) tracked. If the first value is 0.0 (default), that photon is treated normally. Otherwise, it is replaced by two photons with the same total energy. The first value is the opening angle between the photons and the other two specify the energy range (in GeV) of the second photon.
TMAT 30
TMAT describes the target material used. The properties of the target materials are stored in materials.inc.
TRAC 99*TRUE
This option specifies whether every single particle from a selected reaction is tracked, including possible re-decays.
As standard option it is switched to TRUE for all particles. Therefore, one does not have to care about the full decay chain of any excited state, (but it might be useful to select a distinct decay branch).
TRGT TRUE
The target assembly (target, beam pipe, veto barrel) is included in the setup for the simulation.
GAP 0.05 0.05
Gap between both hemispheres of the CB.
HPAC 2
GCALOR is used as a general purpose tool for calculations of particle transport and interactions with matter, covering an extended range of applications [Mar98].

CUTS 0.0001 0.0001 0.001 0.001 0.001 0.0001 0.0001 1E4 1E4 0.01 0.5E-6
Specifies the kinetic energy cuts in GeV for gammas, electrons, neutral hadrons, charged hadrons, muons, electron bremsstrahlung, muon- and hadron bremsstrahlung, δ rays from electrons, δ rays from muons, total energy cut for direct pair production by muons, and time of flight cut in seconds to mimic the QDC integration gate of the CB.

A.11. Cross sections

$m_{\pi^0\pi^0}$ / MeV	$\sigma@lD_2$ / nb	$\Delta\sigma$ / nb	$\sigma@p$ / nb	$\Delta\sigma$ / nb	$\sigma@n$ / nb	$\Delta\sigma$ / nb
272.5	1.33483	0.169362	0.8370555	0.1010	0.49777	0.183643
277.5	2.68228	0.244826	1.6642777	0.0215	1.01801	0.254913
282.5	3.39052	0.274427	1.7085	0.1690	1.68202	0.32229
287.5	3.94511	0.296319	1.6976111	0.1970	2.2475	0.355829
292.5	4.92662	0.319886	1.9737222	0.1970	2.9529	0.375681
297.5	4.4547	0.31982	2.1833125	0.2330	2.27138	0.395695
302.5	5.41864	0.345141	2.2376875	0.2330	3.18095	0.416427
307.5	5.48531	0.335817	2.5991875	0.2490	2.88612	0.41806
312.5	6.34949	0.349078	3.0546875	0.2600	3.2948	0.435265
317.5	6.15112	0.346697	3.1715625	0.2600	2.97956	0.433357
322.5	6.8294	0.346798	3.3615625	0.2720	3.46783	0.440741
327.5	7.95819	0.342164	3.6246875	0.2720	4.3335	0.437105
332.5	7.27111	0.331568	3.8367857	0.2680	3.43432	0.426335
337.5	7.02753	0.332749	3.9746875	0.2740	3.05285	0.431043
342.5	7.57891	0.328439	4.0440625	0.2740	3.53485	0.427725
347.5	6.48136	0.296741	3.8780714	0.2740	2.60328	0.403895
352.5	5.44477	0.287423	3.3855714	0.2500	2.0592	0.380936
357.5	5.46637	0.261099	2.6587857	0.2200	2.80758	0.341427
362.5	4.17618	0.241654	2.5266428	0.2200	1.64954	0.326798
367.5	3.54194	0.220279	1.9405	0.2030	1.60144	0.299553
372.5	2.89816	0.202789	1.1417499	0.1550	1.75641	0.255241
377.5	2.20792	0.178283	0.3584999	0.0780	1.84942	0.194599
382.5	1.4098	0.135739	0.0934999	0.0780	1.3163	0.156554
387.5	0.92548	0.102302	0.0	0.0160	0.92548	0.103546

Table 17: Mass differential cross sections $\pi^0\pi^0$ on Deuterium, proton and neutron for incident photon energies from 400 to 460 MeV.

$m_{\pi^{\pm}\pi^0}$ / MeV	$\sigma@lD_2$ / nb	$\Delta\sigma$ / nb
272.5	0.11659	0.173998
277.5	5.31071	0.934407
282.5	8.35055	0.980562
287.5	11.301	1.02719
292.5	10.0038	1.0036
297.5	9.96991	0.987105
302.5	10.0767	0.929394
307.5	11.3896	0.939784
312.5	12.2362	0.860289
317.5	10.5229	0.82131
322.5	11.5013	0.801241
327.5	10.886	0.738734
332.5	12.4559	0.671017
337.5	11.1498	0.655289
342.5	9.58363	0.627711
347.5	9.49931	0.546409
352.5	9.04424	0.494195
357.5	7.1353	0.476356
362.5	5.46544	0.419929
367.5	5.27983	0.383005
372.5	5.07694	0.363309
377.5	2.82386	0.313011
382.5	2.47233	0.277855
387.5	1.48695	0.247455

Table 18: Mass differential cross sections $\pi^{\pm}\pi^0$ on Deuterium for incident photon energies from 400 to 460 MeV.

E_γ / MeV	$\sigma\,(\pi^0\pi^0)$ / μb	$\Delta\sigma$ / μb	$\sigma\,(\pi^{\pm}\pi^0)$ / μb	$\Delta\sigma$ / μb
400-430	0.3554	0.0721	0.6493	0.2396
430-460	0.7654	0.1356	1.5116	0.3226
460-490	1.8483	0.2195	3.8342	0.4872
490-520	2.8470	0.3028	6.5348	0.6316
520-550	6.2376	0.5655	10.5946	0.7978

Table 19: Total cross sections of the $\pi^0\pi^0$- and the $\pi^{\pm}\pi^0$ channel on Deuterium from 400 to 550 MeV incident photon energy.

Danksagung

Zunächst möchte ich mich ganz herzlich bei Dr. Rainer Novotny bedanken, der mich nach der Diplomarbeit geworben und in das II. Physikalische Institut geholt hat.

Ganz herzlich bedanken möchte ich mich bei Prof. Dr. Volker Metag für die interessante Aufgabenstellung, sein reges Interesse an dieser Arbeit, die Möglichkeit zur eigenständigen Forschung und auch für die eingeräumten Freiräume zur außerberuflichen Weiterbildung.

Dr. Martin Kotulla danke ich für die moralische Unterstützung, die vielen Diskussionen, in denen er mir die richtigen Impulse setzte und natürlich die Betreuung dieser Arbeit.

Auch möchte ich allen danken, die beim Aufbau des Experiments in Mainz geholfen haben, sei es beim Strippen ziehen, Targets tauschen oder Detektoren stapeln. Speziell genannt seien Ralf, Benedicte und Fabien, meine WG- und TAPS-Kollegen sowie die Mainzer (Dirk, Marc, Sven, Michael, Matthias und Eric), die des Öfteren Sachen im Archiv nachschlagen oder Crates resetten mußten und während der Experimentierphase als zentrale Anlaufstelle für die TAPSianer dienten. Ralf und Peter haben darüber hinaus häufig unter meinen C-Kenntnissen leiden müssen. Sie waren es, die immer wieder die Kastanien für mich aus dem Feuer holen mussten wenn der C-Compiler mal wieder nicht so wollte wie ich. Ich glaube, ohne sie würden SlowControl und Acqu bei mir immer noch zumindest partiell streiken.

Werner, Jürgen und Anita, die guten Seelen des Institutes, waren immer für mich da, sei es bei Computerproblemen, technischen und allgemeinen Fragen sowie Verwaltungsangelegenheiten. Zudem hat Jürgen mich sehr stark unterstützt bei der Entwöhnung von Redmond.

Nicht zu vergessen sind die Werkstätten, die ihr Know How vor allen Dingen bei der Konstruktion des Strahlrohrs für die Festkörpertargets einbrachten.

Der gesamten Arbeitsgruppe danke ich für die freundliche Aufnahme und das familiäre Umfeld. Wir haben viele sehr schöne Stunden erlebt, sei es beim Grillen, auf Ausflügen oder auch einfach nur bei der täglichen Arbeit, auch wenn sie gerade in der Schussphase unter meiner Laune zu leiden hatten. Ich hätte die Zeit hier nicht missen wollen (naja, oder zumindest die Meiste). Auch ein großes Dankeschön an den Rest der A2-Kollaboration, die das Arbeiten in einer sehr angenehmen Atmosphäre ermöglichten.

Ein ganz spezieller Dank geht an Prof. Dr. John Price für das hervorragende und reichhaltige Collaboration Dinner mit dem außerordentlich großen Essensangebot im Seafood Restaurant in Los Angeles. Auch möchte ich mich dafür bedanken, daß er uns die heimische Braukunst, wie dem ”Stone Cold Bastard Ale” in der Westwood Village Brewery näherbrachte. Bis dato war mir nicht bekannt, daß man Bier auch aus alten Autoreifen herstellen kann. Nicht zu vergessen seine Bemühungen um die Crystal Ball Simulation.

Bedanken möchte ich mich bei allen Leuten, die diesen Packen Papier Korrektur gelesen

haben (Dave, David, Kottu, Micha, Rainer, Ralf, Stefan und Volker). Ich weiß, aus diesem Kauderwelsch Englisch zu machen war nicht wirklich leicht, aber gemeinsam haben wir es doch (hoffentlich) relativ gut hinbekommen.

Verwandte, Freude und Bekannte zu haben, die einen durchs Leben begleiten und Freud und Leid mit einem teilen ist aber noch viel wichtiger. Um niemanden zu vergessen, danke ich euch allen im Kollektiv, daß ihr für mich da ward und hoffentlich auch weiterhin für mich sein werdet.

Letztendlich bedanke ich mich bei meiner Mutter für die Unterstützung jeglicher Art! Meinem Vater widme ich diese Arbeit.